A Tale of Two Craters: Reconstructing Mars Paleoenvironment Using Orbital and Rover Data at Endeavour and Jezero

Thesis by
Oak A. Kanine

In Partial Fulfillment of the Requirements for
the degree of
Doctor of Philosophy in Geology

CALIFORNIA INSTITUTE OF TECHNOLOGY
Pasadena, California

2026
(Defended July 29th, 2025)

Oak A. Kanine
ORCID: https://orcid.org/0000-0002-9204-6107

ACKNOWLEDGEMENTS

For Olivia.

ABSTRACT

Understanding the evolution of planetary climates and corresponding changes to planetary surfaces involves the study of terrains of various ages and morphologies. Here, I study Endeavour and Jezero, two craters within the martian Noachian Highlands. I use multiple approaches — including sedimentology, stratigraphy, geomorphology, numerical modeling, and the quantitative study of geologic structures in 3D — and a combination of orbital images from satellites and on-the-ground or *in-situ* images from rover-based instruments to conduct detailed and ground-truthed studies at both craters. At each site, I characterize the role of water in shaping the surface and thus constrain the climate of ancient Mars. Also presented in this work is a methodological approach to optimize the usage of rover and orbital images for three-dimensional orientation of geologic structures.

In *Chapter 2,* I find that rockfall is a potential source of erosion on Endeavour's crater rim. Repeated events of large clasts bouncing downslope and eroding bedrock could have generated incised landforms in the absence of flowing liquid water. Boulder deposits atop other crater-infilling units indicate the process of rockfall continued during or after the Noachian-Hesperian boundary (~2.5-2.7 Ga), potentially continuing to shape the crater rim morphology after regional surface desiccation. In contrast, the Jezero crater strata at Kodiak butte discussed in *Chapter 3* are interpreted as either preserved fluvial bars in a braided river or mouth bars in a shallow lake, indicating water was abundant in the crater. Gravel-sized grains were transported by energetic flows, with minimal quiescent settling of fine-grained sediment. Deposits of such settings may have a lower biosignature

preservation potential than those of Gilbert deltas, the previous depositional hypothesis. In *Chapter 4*, I performed traces of beds of the Jezero delta-fan structure in HiRISE and then used apparent dips of a given feature seen from multiple perspectives in rover images to estimate true surface orientations. I confirmed that the orientations of scarps, beds, or other quasi-planar surfaces measured from the highest-available resolution orbital datasets are accurate. However, it is challenging to distinguish hierarchical stratigraphic elements from each other and from erosional surfaces using orbital data, and therefore rover data adds key context for depositional interpretations that inform paleoenviroment. In particular, bedform internal structures could only be determined from rover datasets. In all, through a synthesis of methodological approaches and datasets, I find that the two studied craters potentially record disparate predominant morphology-shaping forces — dry rockfall in Endeavour, and fluvio-lacustrine activity at Jezero. These sites provide spatial and temporal snapshots of past surface conditions on Mars that can be used to build a more complete narrative of the planet's history.

TABLE OF CONTENTS

Chapter 1

INTRODUCTION: STATE OF THE FIELD AND MOTIVATION FOR STUDY

Geologic signatures of liquid surface water are abundant on ancient martian terrain, including valley networks (e.g., Irwin et al., 2005; Fassett and Head, 2008); catastrophic or megaflood outflow channels (e.g., Burr et al., 2009); depositional landforms such as fans and deltas (Di Achille and Hynek, 2010; Morgan et al., 2022); as well as open- and closed-basin crater lakes (e.g., Irwin et al., 2005; Goudge et al., 2015) indicative of ponding water. However, our understanding of the climatic conditions which produced such landforms, the mechanisms by which such a climate was first sustained and then transformed into the modern frigid martian desert, and the timescales over which aqueous activity and climate transitions occurred, remain incomplete and under lively debate. Some interpret the aforementioned geologic evidence as indicative of "warm and wet" conditions in the past with an active hydrologic cycle that sustained rainfall (e.g., Craddock and Howard, 2002; Luo et al., 2017; Ramirez and Craddock, 2018). However, studies of deposit cohesion (Koeppel et al., 2022) and mineralogy (Bishop et al., 2018) suggest that early Mars was typically cold and dry, experiencing only episodic and brief periods of liquid water. Similarly, the "cold and icy" hypothesis (Wordsworth et al., 2015) proposes that Mars in the Noachian to early Hesperian, residing at greater distance than Earth from a Sun that was fainter in its youth, accumulated ice (in the southern highlands in particular (Wordsworth et al., 2013)), which provided flowing water during

excursions to warmer climatic conditions, or as episodic or seasonal melt of snow or ice (e.g., Kite et al., 2013; Palumbo et al., 2018). Still others favor a "dry and warm" hypothesis, wherein the planet was arid to semi-arid, but with enough rainfall to carve the observed valley networks (Ramirez et al., 2020; Kite et al., 2021; Luo et al., 2023). Such as scenario may require a medium (as described in Citron et al., 2018) to large (Di Achille and Hynek, 2010) northern ocean (Ramirez et al., 2020). Geologic evidence for such an ocean has been questioned, however, (Sholes et al., 2019), with smaller-scale paleolakes across the Mars crustal dichotomy proposed as an alternative explanation (Rivera-Hernández and Palucis, 2019).

Climate models struggle to produce above-freezing temperatures in martian conditions consistent with a "warm" paleoclimate scenario (Ramirez et al, 2020). Various atmospheric conditions have been proposed to provide the necessary warming, including clouds (Forget et al., 2013; Ramirez and Kasting, 2017; Kite et al., 2021), an atmosphere of CO_2 mixed with another greenhouse gas such as sulfur compounds (Johnson et al., 2008), H_2 (Turbet et al., 2019; Haberle et al., 2019), CH_4 (Turbet et al., 2019; Kite et al., 2017; Ramirez and Kaltenegger, 2018), H_2O vapor (Kite et al., 2021); or some combination thereof (Ramirez et al., 2014; Kite et al., 2021). To further complicate matters, the warming mechanism must also accommodate wet-dry cycling (e.g., Davis et al., 2018; Rapin et al., 2023), as well as potentially several major climate transitions over geologic time (Kite et al., 2023).

Explaining planetary-scale climate transitions is a daunting task, as is verifying global climate models. Nevertheless, these aspiring hypotheses and models rely on more tangible endeavors: the thorough cataloguing and description of

environmental indicators at specific sites, which provide a tether to reality for theory and computational models. Such a project is undertaken in this work in an effort to find pieces to the Mars paleoclimate puzzle such that we may progress toward answering fundamental questions about the past environment and how it changed with time.

We leverage both orbital datasets — suited for examination of meso-to-large features over potentially spatially expansive regions of interest — and rover datasets — which provide the most detailed ground-truthing available, at typically millimeter to meter-scale — for two sites: Endeavour Crater and Jezero Crater (Figure 1). Both craters are located in cratered and fluvially-dissected terrain in the Southern Highlands. Endeavour is located at 2˚ S latitude in Middle Noachian-aged terrain (Tanaka et al., 2014), placing the age of impact ~3.8 - 3.9 Ga (Hartmann and Neukom, 2001) or younger. Jezero Crater is located at 18˚ N altitude on the edge of the Isidis basin, with age of impact constrained by crater counts on the regional olivine unit to at least 3.8 Ga (Mandon et al., 2020), with subsequent activity in the crater following. Despite the potential similarity in age, while abundant evidence for once-flowing water is present in Jezero crater, including two inlet channels, a depositional fan, and an outlet channel, potential morphological evidence for water-mediated erosion is sparse in Endeavour crater, limited to gullies in the crater wall and a few aerodynamically-shaped (teardrop) rock “islands.”

Our investigation into Mars paleoclimate at these two sites is a three-pronged approach. At Endeavour, we examine the plausibility of a dry environment producing incision on the crater rim via rockfall using numerical modeling and images from the Opportunity rover. In Jezero crater, we use a 3-D outcrop model and Perseverance rover images to undertake a detailed sedimentological and stratigraphic analysis of an erosional remnant of the sedimentary fan and reconstruct the water-rich environmental conditions of its deposition. Also in Jezero, we seize the opportunity provided by overlapping orbital and rover datasets to compare our ability to determine a feature's orientation in space using remotely-sensed vs. *in-situ* datasets, an exercise which informs the lens through which we view remote sensing studies of geologic structure, some of which drive paleoclimate hypotheses.

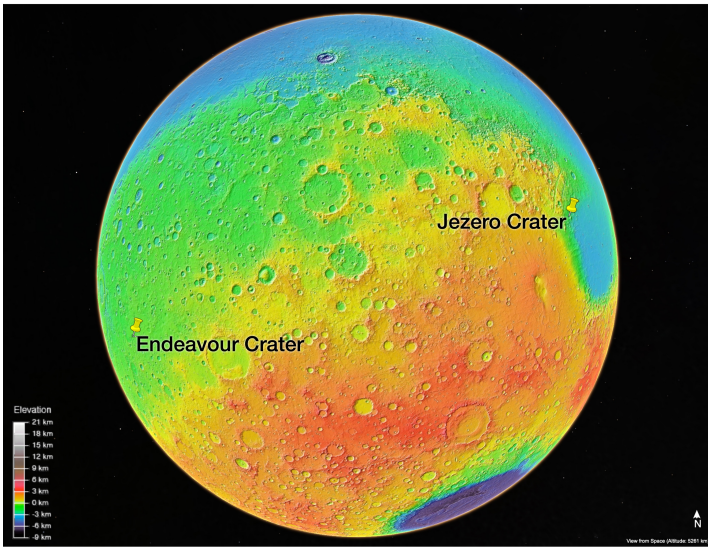

Figure 1: global colorized terrain map of Mars, from Mars Orbiter Laser Altimeter (MOLA) data. Image credit NASA/USGS/ESA/DLR/FU Berlin (G. Neukum). Obtained from Google Earth.

References

Bishop, J.L., Fairén, A.G., Michalski, J.R. et al. (2018). Surface clay formation during short-term warmer and wetter conditions on a largely cold ancient Mars. *Nature Astronomy, 2*, 206–213. https://doi.org/10.1038/s41550-017-0377-9

Burr, D., Wilson, L., & Bargery, A. (2009). Floods from fossae: A review of Amazonian-aged extensional–tectonic megaflood channels on Mars. In D. Burr, P. Carling, & V. Baker (Eds.), *Megaflooding on Earth and Mars* (pp. 194-208). *Cambridge: Cambridge University Press*. https://doi.org/10.1017/CBO9780511635632.010

Citron, R. I., Manga, M., & Hemingway, D. J. (2018). Timing of oceans on Mars from shoreline deformation. *Nature, 555*(7698), 643–646. https://doi.org/10.1038/nature26144

Craddock, R. A., & Howard, A. D. (2002). The case for rainfall on a warm, wet early Mars. *Journal of Geophysical Research, 107*(E11), 5111. https://doi.org/10.1029/2001JE001505

Davis, J. M., Grindrod, P. M., Fawdon, P., Williams, R. M. E., Gupta, S., & Balme, M. (2018). Episodic and declining fluvial processes in southwest Melas Chasma, Valles Marineris, Mars. *Journal of Geophysical Research: Planets*, *123*, 2527–2549. https://doi.org/10.1029/2018JE005710

Di Achille, G., & Hynek, B. M. (2010). Ancient ocean on Mars supported by global distribution of deltas and valleys. *Nature Geoscience*, *3*(7), 459. https://doi.org/10.1038/ngeo891

Fassett, C. I., & Head, J. W. III (2008). Valley network-fed, open-basin lakes on Mars: Distribution and implications for Noachian surface and subsurface hydrology. *Icarus*, *198*(1), 37–56. https://doi.org/10.1016/j.icarus.2008.06.016

Forget, F., Wordsworth, R., Millour, E., Madeleine, J.-B., Kerber, L., Leconte, J., et al. (2013). 3D modelling of the early Martian climate under a denser CO2 atmosphere: Temperatures and CO2 ice clouds. *Icarus, 222*(1), 81–99. https://doi.org/10.1016/j.icarus.2012.10.019

Goudge, T. A., Aureli, K. L., Head, J. W., Fassett, C. I., & Mustard, J. F. (2015). Classification and analysis of candidate impact crater-hosted closed-basin lakes on Mars. *Icarus*, *260*, 346–367. https://doi.org/10.1016/j.icarus.2015.07.026

Haberle, R. M., Zahnle, K., Barlow, N. G., & Steakley, K. E. (2019). Impact degassing of H2 on early Mars and its effect on the climate system. *Geophysical Research Letters, 46*, 13,355–13,362. https://doi.org/10.1029/2019GL084733

Hartmann, W. K., & Neukum, G. (2001). Cratering chronology and the evolution of Mars. *Space Science Reviews*, 96(1–4), 165–194. https://doi.org/10.1023/A:1011945222010

Irwin, R. P., Howard, A. D., Craddock, R. A., & Moore, J. M. (2005). An intense terminal epoch of widespread fluvial activity on early Mars: 2. Increased runoff and paleolake development. *Journal of Geophysical Research, 110*, E12S15. https://doi.org/10.1029/2005JE002460

Johnson, S. S., Mischna, M. A., Grove, T. L., & Zuber, M. T. (2008). Sulfur-induced greenhouse warming on early Mars. *Journal of Geophysical Research, 113*, E08005. https://doi.org/10.1029/2007JE002962

Kite, E., Gao, P., Goldblatt, C. et al. (2017). Methane bursts as a trigger for intermittent lake-forming climates on post-Noachian Mars. *Nature Geoscience 10*, 737–740. https://doi.org/10.1038/ngeo3033

Kite, E. S., Steele, L. J., Mischna, M. A. & Richardson, M. I. (2021). Warm early Mars surface enabled by high-altitude water ice clouds. *Proceedings of the National Academy of Sciences of the USA 118*, e2101959118. https://doi.org/10.1073/pnas.2101959118

Koeppel, A.H.D., et al. (2022). A fragile record of fleeting water on Mars. *Geology, v. 50*, p. 152–157. https://doi.org/10.1130/G49285.1

Luo, W., Cang, X., & Howard, A. D. (2017). New Martian valley network volume estimate consistent with ancient ocean and warm and wet climate. *Nature Communications, 8*, 15766. https://doi.org/10.1038/ncomms15766

Luo, W., Howard, A. D., Craddock, R. A., Oliveira, E. A., & Pires, R. S. (2023). Global spatial distribution of Hack's law exponent on Mars consistent with Early arid climate. *Geophysical Research Letters*, *50*, e2022GL102604. https://doi.org/10.1029/2022GL102604

Mandon, L., Quantin-Nataf, C., Thollot, P., Mangold, N., Lozac'h, L., Dromart, G., et al. (2020). Refining the age, emplacement and alteration scenarios of the olivine-rich unit in the Nili Fossae region, Mars. *Icarus*, 336, 113436. https://doi.org/10.1016/j.icarus.2019.113436

Morgan, A. M., Wilson, S. A., and Howard, A. D. (2022). The global distribution and morphologic characteristics of fan-shaped sedimentary landforms on Mars, *Icarus, 385*, 115137. https://doi.org/10.1016/j.icarus.2022.115137

Palumbo, A. M., Head, J. W., & Wordsworth, R. D. (2018). Late Noachian Icy Highlands climate model: Exploring the possibility of transient melting and fluvial/lacustrine activity through peak annual and seasonal temperatures. *Icarus, 300*, 261–286. https://doi.org/10.1016/j.icarus.2017.09.007

Ramirez, R. M., & Craddock, R. A. (2018). The geological and climatological case for a warmer and wetter early Mars. *Nature Geoscience, 11*(4), 230. https://doi.org/10.1038/s41561-018-0093-9

Ramirez, R. M., & Kaltenegger, L. (2018). A methane extension to the classical habitable zone. *The Astrophysical Journal, 858*(2), 72. https://doi.org/10.3847/1538-4357/aab8fa

Ramirez, R. M., Craddock, R. A., & Usui, T. (2020). Climate simulations of early Mars with estimated precipitation, runoff, and erosion rates. *Journal of Geophysical Research: Planets*, *125*, e2019JE006160. https://doi.org/10.1029/2019JE006160

Ramirez, R. M., & Kasting, J. F. (2017). Could cirrus clouds have warmed early Mars? *Icarus, 281*, 248–261. https://doi.org/10.1016/j.icarus.2016.08.016

Ramirez, R. M., Kopparapu, R., Zugger, M. E., Robinson, T. D., Freedman, R., & Kasting, J. F. (2014). Warming early Mars with CO2 and H2. *Nature Geoscience, 7*(1), 59–63. https://doi.org/10.1038/ngeo2000

Rapin, W. et al. (2023). Sustained wet–dry cycling on early Mars. *Nature 620*, 299–302. https://doi.org/10.1038/s41586-023-06220-3

Rivera-Hernández, F., & Palucis, M. C. (2019). Do deltas along the crustal dichotomy boundary of Mars in the Gale crater region record a northern ocean? *Geophysical Research Letters, 46*, 8689–8699. https://doi.org/10.1029/2019GL083046

Sholes, S. F., Montgomery, D. R., & Catling, D. C. (2019). Quantitative high-resolution reexamination of a hypothesized ocean shoreline in Cydonia Mensae on Mars. *Journal of Geophysical Research: Planets*, *124*, 316–336. https://doi.org/10.1029/2018JE005837

Tanaka, K.L., Skinner, J.A., Jr., Dohm, J.M., Irwin, R.P., III, Kolb, E.J., Fortezzo, C.M., Platz, T., Michael, G.G., and Hare, T.M. (2014). Geologic map of Mars: U.S. Geological Survey Scientific Investigations Map 3292, scale 1:20,000,000, pamphlet 43 p. https://dx.doi.org/10.3133/sim3292

Turbet, M., Tran, H., Pirali, O., Forget, F., Boulet, C., & Hartmann, J.-M. (2019). Far infrared measurements of absorptions by CH4+ CO2 and H2+ CO2 mixtures and implications for greenhouse warming on early Mars. *Icarus, 321*, 189–199. https://doi.org/10.1016/j.icarus.2018.11.021

Wordsworth, R. D., Forget, F., Millour, E., Head, J. W., Madeleine, J.-B., & Charnay, B. (2013). Global modelling of the early Martian climate under a denser CO2 atmosphere: Water cycle and ice evolution. *Icarus, 222*(1), 1–19. https://doi.org/10.1016/j.icarus.2012.09.036

Wordsworth, R. D., Kerber, L., Pierrehumbert, R. T., Forget, F., & Head, J. W. (2015). Comparison of "warm and wet" and "cold and icy" scenarios for early Mars in a 3-D climate model. *Journal of Geophysical Research, Planets, 120*(6), 1201–1219. https://doi.org/10.1002/2015JE004787

Chapter 2

BEDROCK CHUTE FORMATION BY DRY ROCKFALL IN ENDEAVOUR CRATER, MARS

Kanine, O[1]., Cardenas, B.T. [2], Beer, A.R.[3], Golombek, M.[4], Lamb, M.P.[1].

[1]Division of Geological and Planetary Sciences, California Institute of Technology, Pasadena, California 91125, USA
[2]Department of Geosciences, The Pennsylvania State University, University Park, PA 16802
[3]Department of Geosciences, University of Tübingen, D-72076 Tübingen, Germany
[4]Jet Propulsion Laboratory, California Institute of Technology, Pasadena, CA, 91109

Corresponding author: Michael Lamb (mpl@caltech.edu)

Accepted with minor revisions, JGR: Planets

KEY POINTS

- Rockfall erosion is a plausible mechanism to form bedrock chutes in the western Endeavour crater wall.
- Rockfall initiated in locally steep rocky outcrops can traverse lower gradients downslope.
- Rockfall is funneled into some alcoves and chutes, which could lead to focused erosion and landform development.

PLAIN LANGUAGE SUMMARY

Rocks sourced from steep bedrock outcrops can bounce downhill and erode the underlying material. Numerical modeling of falling rocks and study of images from the Opportunity rover and orbital satellites suggest that the some of the erosion of the interior wall of the Endeavour crater rim on Mars might have been driven by rockfall instead of flowing water.

ABSTRACT

Degradation of crater topography is important on planetary surfaces as it can record environmental conditions through rates and processes of erosion. Regolith creep is classically thought to dominate crater wall degradation, leading to smooth crater walls. Processes that create rough topography, such as chutes and alcoves, are often attributed to volatiles. Here we explore an alternate hypothesis for chute formation by erosion from dry rockfall. We mapped the western rim of Endeavour crater, Mars, including the Marathon and Perseverance valleys visited by NASA's Mars Exploration Rover (MER) Opportunity. Marathon Valley is a broad alcove with locally steep, rubbly outcrops, a moderately sloping (18˚) bedrock floor dissected by a network of shallow grooves, and boulders downslope. When initiated from these steep (>45˚) outcrops, rockfall modeling shows focused impacts near the headwall of Marathon Valley and rocks that traverse the valley floor even at gradients below the angle of repose. Perseverance Valley is a smaller chute with relief that is too subtle to be captured in the digital elevation model, and therefore the model does not produce funneled rockfall there. Across the Endeavour crater rim, the rockfall-erosion hypothesis is consistent with locally steep rock outcrops as rockfall sources, boulder fields, and the rough chute-and-spur topography. We propose that through topographic steering, rockfall can be funneled into chutes and alcoves, concentrating impacts and erosion there, and further developing these landforms in the absence of flowing water.

1 INTRODUCTION

Many rocky planetary bodies, including the Moon and Mars, are heavily cratered. The density and size-distribution of craters give insight into the impact history as well as degradation processes (e.g., Craddock and Howard, 2000; Golombek et al., 2014). As craters age, they degrade; following the initial impact, the slope of the crater rim relaxes, rim height decreases, and the bowl of the crater is infilled (e.g., Howard, 2007). Degradation can erase some craters entirely. Ultimately, the pace and processes of surface degradation inform us about the environmental history of the planet, including the presence and activity of volatiles such as water (e.g., Bamber et al., 2022; Dundas et al., 2015; Tebolt et al., 2020). In addition, the rate at which craters fill can be compared to the rate at which the rim degrades, providing clues to the dominant degradational process (e.g., Golombek et al., 2006, 2014; Grant et al., 2006; Sweeney et al., 2018). Thus, understanding the pace of crater degradation and the role of volatiles helps address some major questions of planetary science, such as the history of surface water on Mars and the timescale of environmental history recorded in landforms. In addition, the size frequency distribution of craters, in combination with models of orbital dynamics and impact rates (e.g., Hartmann and Neukom, 2001; Hartmann, 2005), is the primary chronometer used to date rocky planetary terrains. Crater modification can influence age dating by removing some crater populations entirely or changing their diameter and depth (e.g., Palucis et al., 2020).

The process controlling crater wall degradation on Mars and the Moon, and hillslope and scarp degradation on Earth, is typically regolith creep (e.g., Howard, 2007; Fassett and Thomson, 2014). Disturbance-driven regolith creep occurs when expansion and contraction of regolith under gravity produces a slow and gradual downslope movement of regolith proportional to topographic slope (Gilbert, 1909). For such a case, regolith creep can be described well by topographic diffusion (Pelletier, 2008). Regolith expansion can be caused by a myriad of factors, such as thermal gradients, seismicity, changes in pore volatiles, or micrometeorite impacts (e.g., Armitage et al., 2011; Fassett and Thomson, 2014; Golombek et al., 2014; Sweeney et al., 2018). Non-linear transport laws also have been developed to represent mass movement on steep slopes, such as avalanches and landslides, where regolith flux beyond a threshold slope becomes large and produces a more planar (rather than convex) topographic profile (Roering et al., 1999; Roering et al., 2001).

While linear and nonlinear hillslope diffusion models appear to capture the general topographic relaxation of aging craters (e.g., Fassett and Thomson, 2014; Golombek et al., 2014; Sweeney et al., 2018), they fail to fully describe the three-dimensional morphologies observed on many degrading crater walls, such as alcoves, rocky promontories, chutes, and channel-like landforms (Figure 1). The presence of these landforms suggests that processes in addition to regolith creep are important in crater degradation. Channelized landforms, such as gullies, are commonly attributed to volatile activity such as fluvial processes (Malin and Edgett, 2000; Hughes et al., 2019), debris flows (Costard et al., 2002; Christensen,

2003), snowmelt (Dickson et al., 2007), groundwater sapping (Malin and Edgett, 2000) and CO_2 frost (Ishii and Sasaki, 2004; Dundas et al., 2010; Diniega et al., 2010). Thus, the deviation from diffusive topography is potentially an important indicator of volatile activity. For example, some crater degradation models include both water runoff and regolith creep (Howard, 2007), and the degree to which crater roughness deviates from the smooth topographic-diffusion endmember has been used to infer the magnitude of fluvial incision (Hughes et al., 2019).

In addition to volatile activity, dry processes may shape crater topography and smaller-scale morphological features. Wind abrasion can create ventifacts (e.g., Sullivan et al., 2005) and carve valleys. On Mars, aeolian transport can remove crater infill and create features ranging in scale up to Aeolis Mons (Mt. Sharp) (e.g., Day et al., 2016). Our focus here is on dry rockfall, which has been shown to be an important mechanism to create bedrock chutes and rocky spurs on degrading hillslopes (Kumar et al., 2013; Levin et al., 2022; Cardenas et al., 2025). Theory tested by physical experiments shows that rockfall can create and then be funneled into topographic lows in much the same way as flowing water, forming discontinuous proto-channels that become chutes through differential erosion (Sun et al. 2022; Beer et al., 2024a). Each rock makes successive impacts on the underlying substrate as it traverses downslope, causing erosion and chute formation similar to how bedrock river incision is driven by impacts from saltating particles (Beer and Lamb, 2021; Sun et al., 2022; Beer et al., 2024a). Although dry mass movements are sometimes considered unlikely and ineffective at slopes below the

angle of repose, numerical modeling (Pelletier et al., 2008; Kolb et al., 2010), field experiments (DiBiase et al., 2017), and physical models (Sun et al., 2022) have shown that rockfall can traverse lower gradients when large rocks are traveling over a relatively smooth bedrock surface owing to low rolling/bouncing friction.

Bedrock chutes have been documented on the Moon and are more abundant on Mars (Figure 1) (Kumar et al., 2013; Levin et al., 2022). While also present on Earth (e.g., Beer et al., 2024a), it is difficult to disentangle dry formation mechanisms from water-mediated ones on a planet with near-ubiquitous aqueous activity. Chute abundance and relief show some latitude and aspect dependence on Mars, especially at mid latitudes, suggesting at least some role for volatile activity in cases (Levin et al., 2022). Water or frost could also play a role in rockfall initiation (Sylvest et al., 2016, Hugenholtz, 2008; Pilorget and Forget, 2016). Nonetheless, chutes are found over a wider range of latitudes than gullies on Mars (Levin et al., 2022), including low latitudes, and they also occur on the Moon (Kumar et al., 2013), suggesting that the formation of bedrock chute-and-spur topography has occurred by rockfall erosion alone in the absence of volatiles (Sun et al., 2022; Beer et al., 2019). A survey of rockfall boulder-and-trail signatures also did not find a correlation between rockfall locations and volatile abundance or (predicted) diurnal or seasonal frost cover (Bickel et al., 2024).

In this work we leverage high-resolution observations of the heavily degraded western wall of Endeavour crater, made by the Mars Explorer Rover (MER) Opportunity (Figure 2) from 2011 to 2018, to explore the rockfall erosion

hypothesis. The rover focused its final campaign on two bedrock troughs on the inner western wall of Endeavour crater, named Marathon Valley and Perseverance Valley. These landforms deviate from the smooth slopes one would expect from degradation by regolith creep. The shapes of these landforms, along with their gradients less than the angle of repose, led to the hypothesis that volatile activity played a role in their formation (e.g., Fraeman et el., 2017; Squyres et al., 2018). However, upon exploring the terrain, evidence for water-driven erosion was inconclusive. Fluvial and debris-flow deposits were not found. Multiple hypotheses emerged for the troughs and the features within them, including incision by fluid or fluidized flow (Parker et al., 2018; Squyres et al., 2018; Hughes et al., 2019), subsurface fluid flow controlled by faults and fractures (Crumpler, et al., 2016, 2017, 2018), aeolian abrasion funneled by the same faults, and impact-related fractures that reactivated after the Noachian (Sullivan et al., 2018; Fraeman et al., 2017). In addition, dry rockfall was proposed as a potential erosive agent and explored as a formation mechanism for Perseverance Valley (Beer et al., 2019).

Given recent advances in our understanding of the effectiveness of rockfall driven bedrock incision (Sun et al. 2022; Beer et al. 2024a), we revisit observations from the MER rover of the Endeavour crater rim to examine the hypothesis that dry rockfall played a role in the formation of Marathon Valley and Perseverance Valley, as well as the degradation of the crater rim as a whole. In the following section, we review the MER traverse in Endeavour crater and previous work on crater degradation processes. Next, we present our methods that include mapping and

rover observations pertinent to the rockfall hypothesis, and a numerical model for rockfall erosion (Beer et al., 2024a; Cardenas et al., 2025). Results include documentation of landform morphology, rockfall sources and runout locations, and comparison to rockfall model predictions. Finally, we discuss the potential importance of rockfall erosion as a degradation process at Endeavour crater and elsewhere on Mars.

2 ENDEAVOUR CRATER AND *OPPORTUNITY* TRAVERSE

Opportunity landed in Eagle crater, Mars, on January 24th, 2004 PST, and roved 45.16 km across Meridiani Planum over the course of nearly 15 years (Figure 2). One of the mission objectives was the search for signs that the ancient martian surface hosted liquid water and habitable environments. Opportunity reached Endeavour crater, a 22-km diameter, Noachian-aged crater, in 2011. The last transmission from Opportunity was received on Sol 5111 (June 10, 2018), and the mission ended on February 13, 2019, with Opportunity remaining in Perseverance Valley in Endeavour crater.

Previous work has described two primary phases of degradation in the region of the MER traverse, Meridiani Planum. The first was one of higher erosion rates of ~ 1 m/Myr (Golombek et al., 2006; Golombek et al., 2014) in the Noachian, where denudation was comparable to the slowest terrestrial rates in the presence of water (Golombek et al., 2006). Fluvial activity (Grant et al., 2016) in a warm and

wet climate (Golombek et al., 2006 and references therein) may have dominated erosion. The second phase represented the desiccated climate from the late Noachian to the early Hesperian (3.7-3.5 Ga) and continuing to the present, with erosion rates of ~0.0003 m/Myr to 0.1 m/Myr, consistent with aeolian weathering and infill by sand grain saltation (Golombek et al., 2006). In total, Grant et al. (2016) estimated that the Endeavour crater rim has experienced 100-200 m of vertical degradation. Through study of small (< 100 m diameter) craters along the traverse that date to this second phase of degradation, Golombek et al. (2014) observed a decrease in erosion rate over time, consistent with the relaxing of crater slope, infill by transported sand, and a corresponding decrease of regolith flux downhill in accordance with a linear diffusion model with a diffusivity of ~10^{-6} m^2/yr, similar to the diffusivity of 8×10^{-7} m^2/yr for the Hesperian and Amazonian found for small craters in Elysium Planitia (Sweeney et al., 2018). The modification of Endeavour over billions of years has yielded lower-relief geometry, a generally rounded and segmented rim (regions where the rim is completely buried are interspersed with stretches of protruding rim, Figure 2), removal of large amounts of its impact ejecta blanket, and infilling of the crater bowl (e.g., Grant et al., 2016).

However, there is evidence for modification processes of the rim beyond aeolian erosion and regolith creep, including incised bedrock chutes (also referred to previously as valleys; Figure 2c and 2d), blocky outcrops, and extensive boulder fields originating from the crater rim. Hughes et al. (2019) sought to understand the

degradation state by comparing the topography of the Endeavour rim to a numerical model that simulated the evolution of the nearby, similarly-sized, and relatively fresh Bopolu crater. The model described regolith creep and fluvial incision under different climate parameters (Howard et al., 2007), and from comparison of modern Endeavour topography to the model outputs, the authors concluded that Endeavour crater likely evolved in a semi-arid climate and under fluvial activity that produced the channel-like landforms on the crater wall (Hughes et al., 2019). Regolith creep alone could not produce these landforms. However, chute formation by dry avalanching or other processes were not included in the model (Howard et al., 2007), such that any deviation from the smooth topography expected from topographic diffusion was attributed to fluvial activity.

The rover team directed Opportunity to investigate Marathon Valley (Figure 2c) and Perseverance Valley (Figure 2d) because of the potential for aqueous activity given that: (i) their channel-like morphologies do not conform to models for degradation by regolith creep alone, and (ii) they have downslope gradients of around 10-22˚, which was considered at that time to be too shallow for dry rockfall and granular flows to be effective (Squyres et al., 2018; Fraeman et al., 2017). Here we revisit these MER observations and previously proposed formation hypotheses and re-evaluate dry rockfall as a potential degradation process in light of recent work that shows that rockfall can be effective at eroding chutes on rocky slopes less than the angle of repose (Sun et al., 2022; Levin et al., 2022; Beer et al., 2024a; Cardenas et al., 2025).

3 METHODS

We considered three criteria for rockfall to be a plausible mechanism for forming bedrock chutes: 1) rockfall must be generated at steep outcrops upslope; 2) rockfall must run out across the relatively low gradient valley floors across bedrock surfaces where impacts can drive erosion; 3) rockfall must be funneled into chutes such that impacts would be concentrated there, leading to preferential erosion of chute floors and further development of the chute (Sun et al., 2022). To evaluate these criteria, we used a combination of observations from orbital and rover imagery as well as a process-based model for rockfall transport and erosion (Beer et al., 2024a; Cardenas et al., 2025).

3.1 Photogeologic mapping and MER Opportunity image analysis

Photogeologic mapping from orbit of Endeavour crater to identify potential sources for rockfall, resting boulders that may have been sourced from rockfall events, and exposed or eroded bedrock on valley floors relied upon a HiRISE (High-Resolution Imaging Experiment) (McEwen et al., 2007) Mars Reconnaissance Orbiter (MRO) visual orthomosaic at ~25 cm/pixel resolution. Topographic analyses (measurements of feature slopes and widths) relied on a USGS-Astrogeology HiRISE stereogrammetric digital elevation model (DEM) at ~1 m per elevation posting. Analysis of finer-scale fabrics, grain sizes, and features not visible from orbit used MER Pancam and Navcam images. The Opportunity

Pancam was a stereo multispectral camera that had a focal length of 43 mm and an instantaneous field of view (IFOV) or angular resolution of 0.27 mrad/pixel (Bell et al., 2003); Opportunity Navcam was a monochrome stereo camera with a focal length of 14.67 mm and an IFOV of 0.82 mrad/pixel (Maki et al., 2003). Images shown here are from sols 4082 to 5111 and include Pancam enhanced color images to increase interpretability and contrast (e.g., between lithologies, grain sizes, etc.).

3.2 Rockfall model

We used a numerical rockfall model to further evaluate where rockfall might be initiated, whether rockfall could traverse the exposed bedrock of the valley/chute floors, and whether rockfall could be funneled into chutes allowing for enhanced erosion that could grow the chute-and-spur topography (Sun et al., 2022). The numerical model is described by Beer et al. (2024a, b) and adapted to Python by Cardenas et al. (2023, 2025); here we summarize its key components.

In the model, falling rocks follow ballistic trajectories according to classical mechanics and neglecting air drag (Beer et al., 2024a). Each event consists of a single rock that is explicitly tracked including hop heights and hop lengths. Thus, the model is representative of isolated rockfall events, consistent with observations of individual boulder trails (e.g., Vijayan et al., 2021), not rock avalanches with many interacting particles. Particles accelerate down steep gradients owing to larger hop heights such that potential energy is converted into kinetic energy.

Energy losses at impacts were computed using a shock term that has been calibrated in experiments (Beer et al., 2024a); rocks stop moving when their velocity declines to zero or when they land in a local topographic depression. At impact locations, further local rockfall azimuthal trajectories are determined by a weighted average of rockfall momentum and the local gravitational driving stress as determined by the local slope, following DiBiase et al. (2017). The rockfall trajectories have been calibrated and validated against laboratory and field data (DiBiase et al., 2017; Sun et al. 2022; Beer et al. 2024a). Because the model is physics-based, gravity is explicitly included in the rockfall transport and bedrock erosion equations and can be readily parameterized for Mars. Although the code can be employed in a landscape-evolution model, evolving topography as the ground surface is raised or lowered (Beer et al., 2024a; Cardenas et al., 2025), here we focused only on the routing of falling rocks. We tracked rockfall initiation locations, impacts sites, and resting points, with each rock run over the modern topography. We infer that more erosion would occur where rockfall impacts into bedrock are concentrated (e.g., Beer and Lamb, 2021).

To apply the model to Endeavour crater, we used as an initial condition the HiRISE DEM. Based on sizes of rocks observed at Endeavour crater (see *Section 4, Results*), we set rockfall grain diameter to be 0.25 m and rock density of basalt (2900 kg/m^3). The location of each falling rock was randomly selected from cells where local slopes exceeded 45˚, consistent with the location of rockfall generation on Earth (DiBiase et al., 2017). Rocks are released from the elevation of the

generating cell, with the launch angle and initial velocity randomly selected between 5-10˚ above horizontal and 1-5 m/s, respectively. Roughness of underlying topography is incorporated as variability in bounce direction, wherein 10˚ azimuth is added or subtracted from the next ballistic trajectory as determined by a routing algorithm (DiBiase et al., 2017). The resultant heatmaps of rockfall initiation sites, bounce locations, and resting points accumulated over 730,400 rocks releases (which may be thought of as trials) are best understood as "probability" maps designed to evaluate the plausibility of rockfall as a process active across the modern Endeavour topography, not as predictions of a future state of the crater rim.

4 RESULTS

4.1. Marathon Valley Observations

Marathon Valley is an alcove with a U-shaped to flat-floored (in cross section) topographic trough, 135 m at its widest, which incises the approximate latitudinal center of the western rim of Endeavour crater (Figures 3, 4). This trough continues to the highest point in the crater rim, where it loses coherent expression as the rim gently slopes to the plains outside of the crater (Figure 4). Closest to the rim peak, the slope of the trough is ~10˚. Downslope it steepens to ~18˚, before beginning to shallow again near the contact of the Lower Shoemaker formation (impact breccias, e.g., Arvidson et al., 2014) and the Burns formation (post-impact, overlying sulfate-rich sandstones, e.g., Grotzinger et al., 2005) in the crater bowl,

at which point the valley loses topographic expression. The southern half of the trough's head appears to extend through the crater rim, meaning it is not a continuous amphitheater-shaped hollow (Figures 3, 4). Steep scarps, expressed in orbital data as blocky or rubbly terrain, are present at the head and sides of the trough (Figure 4c, 3d). The blocky and rubbly textures are typically found only in regions of steep slope; nearly all of the scarp areas having slopes > 23˚, and all of the mapped rubbly regions contain cells with slopes 34˚-45˚, and some even steeper than 45˚ (Figure 4d). Meter-scale boulders are found in a small field near the head of Marathon Valley (Figure 4c).

Marathon Valley contains several dark-toned grooves that transect its bedrock floor (Figure 4b and Figure 5) through Shoemaker formation breccias (Fraeman et al., 2017). These linear grooves are less than ~2 m in width, are continuous for tens of meters, and have slopes up to 18˚ (Figure 4d and e) as measured from the HiRISE DEM. The grooves are only 5-15 cm deep as measured on Navcam orthomosaics (Fraeman et al., 2017). These grooves are of low sinuosity and split and rejoin each other to outline irregular light-toned rocky patches (Figure 4). The dark tone of the grooves comes from sandy regolith infill, which can be distinguished in rover images from the light-toned bedrock (Figure 5). In the grooves, lighter-toned material that emerges from the darker, finer-grained fill (Figure 5) is likely exposure of the substrate into which the grooves were carved. Downslope in the trough, as viewed from HiRISE, dark toned material becomes more abundant, such that the light-toned material eventually forms bedrock ridges

(Figure 4). Some of the grooves are lined by subtle topographic ridges (Figure 5), which appear to be the light-toned bedrock. Within the grooves, we did not recognize any fluvial bedforms or barforms. The grooves terminate by the end of Marathon Valley, when the trough opens into the bowl of the crater.

Also visible throughout Marathon Valley in the rover images are abundant boulders up to ~1.5 m in diameter as measured on HiRISE (Figure 6). The boulders are found for hundreds of meters onto the plains downslope of the valley, forming lobate boulder deposits downslope of the rocky escarpments (Figure 4). Downslope of the larger boulder deposits, some boulders are even found amongst aeolian dunes. Just to the south of Marathon Valley, the light-toned Burns formation appears to be covered by one of these boulder fields.

4.2. Perseverance Valley Observations

South of Marathon Valley, Perseverance Valley is a network of shallow bedrock chutes (Figures 3, 7). There is a shallow depression on the highland terrain that borders Perseverance Valley that could be a possible upslope catchment area to where Perseverance Valley breaches the crater rim (Figure 7b), but the relationship between the upslope depression and the chutes is unclear. Perseverance Valley is much more subdued in topographic expression than Marathon Valley. The single main alcove in the crater rim at the head of Perseverance Valley is characterized by subtle concave elevation contours, but the meters-wide downslope

chutes are indistinguishable topographically from surrounding terrain in the HiRISE DEM, so we may infer that, like the grooves of Marathon Valley, they are < 1 m in depth. The two main chutes or branches bifurcate and merge downslope for a span of ~180 m, including notably around a bedrock knob (Figure 9). Both branches have linear longitudinal profiles (Figure 8) and low sinuosity, though greater than that of the nearly straight grooves of Marathon Valley. The slope of the northern chute is 19˚; the southern chute is nearly 20˚. Adjacent to but not within the troughs, the crater wall has ~17˚ slope. Other bedrock alcoves are present along the nearby crater rim, but these do not appear to have associated channel-like forms.

In MER images, Perseverance Valley closely resembles the grooves in Marathon Valley, with dark-toned depressions incising topographically higher light-toned rock. There appear to be subtle ridges of blocky material on the sides of Perseverance Valley (Figure 9), similar to the ridges that bounded the grooves in Marathon Valley. Boulders are present in Perseverance Valley (Figure 9e), though less abundant than in Marathon Valley. The boulders may have been sourced from steep rocky areas upslope (Figure 9d) that have similar expression to the bedrock scarps in Marathon Valley. Notably, the bedrock scarps are visible in the rover imagery but not in HiRISE, implying they are smaller (< ~1-2 m) in Perseverance Valley than in Marathon Valley. Boulder fields are not apparent downslope of Perseverance Valley in orbital images, unlike for Marathon Valley. Perseverance Valley ends abruptly at the most downslope extent of the Shoemaker breccias and is not observed to cross into the Burns formation in either rover or orbital images.

4.3 Rockfall Model

Using the rockfall model, we simulated the release of an arbitrary number (730,400) of rocks over the Endeavour rim HiRISE digital elevation model. The rockfall model results show that rockfall would not have been limited to Marathon and Perseverance Valleys, but instead there are locally steep bedrock outcrops that could source rockfall across the entire length of the Endeavour rim remnant. Rockfall runout and impacts are similarly possible across the entire western rim (Figure 10a) despite much of the terrain having slopes less than ~20˚. Much of the rim wall below the crest is modeled as likely to experience rockfall impacts (Figure 10a), and grain bounces occur even hundreds of meters downslope into the crater bowl (Figure 10d, e). However, stop locations do not always cluster in lobes in the crater bowl as would be consistent with the lobate boulder fields observed in HiRISE (example in Figure 4b). Rather, stopped boulders display a dispersed pattern downslope of the crater wall.

The model predicts concentrated rockfall impacts (more than two impacts per cell for a run of 730,400 rocks) in several locations, wherein erosion may have been enhanced (Sun et al., 2022). The most prominent of these sites sits between Marathon and Perseverance Valleys (approximate center, Figure 10a, teal patch), where a relative abundance of steep scarps causes high numbers of rockfall. This area has a similar topographic expression as Marathon Valley, complete with a well-defined rocky alcove, and dark-toned grooves and light-toned streaks (located

primarily near the valley head with some subtle examples at the toe), as well as boulder fields downslope.

For Marathon Valley, blocky scarps that exceed the 45˚ threshold for rockfall initiation are found near the head and on the edges of the valley (Figure 10d). Rockfall impacts are focused near the floor of Marathon Valley due to topographic funneling of rockfall, where impacts exceed 5 per cell for much of the valley (Figure 10b). The most densely-populated stop locations are consistent with observations of a lobate boulder field (dotted black line in Figure 10d) within the valley.

In Perseverance Valley, we do not expect topographic funneling of rockfall (at least not in the model) since the valley is not resolved in the HiRISE DEM. Nonetheless, the model does identify some local rockfall source scarps (45˚ or greater local slope) in the region of Perseverance Valley, but fewer than in Marathon Valley (Figure 10e). Rockfall is predicted to traverse downslope despite the low gradients and create dispersed rockfall deposits, consistent with observations of scattered rocks.

5 DISCUSSION

Though the rim of Endeavour crater is heavily degraded, the rim morphology is not consistent with canonical predictions of degradation by regolith

creep, which tends to smooth topography (Golombek et al., 2014; Hughes et al., 2019). Instead, the rim is dissected by alcoves and chutes of widely varying scale with steep rocky escarpments (Figures 3, 4, 8). Some topographic troughs have floors cut by smaller grooves, as in Marathon Valley (Figures 4, 5), and Perseverance Valley itself is of similar scale to these grooves (Figures 8, 9). Dry avalanching was initially dismissed as an erosion mechanism at Endeavour Crater because the crater wall has lower slopes (<~20˚) than the typical angle of repose of colluvium (30-45˚) (Squyres et al., 2018; Fraeman et al., 2017). However, no deposits from lake overspill (Parker et al., 2018), fluvial transport, or debris flows were found by the Opportunity Rover. In rover images of Marathon Valley and Perseverance Valley we observe neither clast imbrication, as might be expected for the proposed fluid-mediated incision, nor poorly-sorted, matrix-supported deposits that are ubiquitous in debris flows.

We sought to test the plausibility of dry rockfall as an alternative process in crater rim degradation and in the development of bedrock chutes. We found that, across the western rim, there are abundant rubbly outcrop scarps, some occurring on the edges of alcoves, that are sufficiently steep to initiate rockfall and source boulders. These steep regions are more common in Marathon Valley (Figure 4d) than in Perseverance Valley (Figure 8b), consistent with the much more developed relief of Marathon Valley. Importantly, rockfall is predicted along the entire degraded crater rim. Gradients downslope of these source regions are sufficiently steep for rockfall transport, with modeled rockfalls running out over relatively low

slopes (Figures 4d, 8c) for long distances resulting in multiple impacts (Figure 10a) that would erode the underlying substrate (Beer and Lamb, 2021). Physical experiments confirm that rocks can readily be transported and can erode bedrock at gradients similar to those of the Endeavour western rim (Sun et al., 2022, Beer et al., 2024a) (Figures 4, 8). Boulders are visible in images of Marathon Valley and Perseverance Valley and in fields extending into the crater bowl in multiple locations, indicating that rockfall has occurred on the crater wall.

Modeled rockfall impacts are not homogenously distributed in space. In some of the chutes and alcoves, they are concentrated, which could allow for the further development of incised landforms via differential erosion rates. Rockfall can erode underlying bedrock through impact abrasion, and topographic steering into proto-chutes can lead to enhanced impacts there, further developing the chute (Sun et al., 2022; Beer et al., 2024a). We found that impacts are more frequent in troughs large enough to be discernible on the HiRISE DEM, including Marathon Valley (Figure 10b). These results are consistent with recent numerical models of idealized craters in which rockfall erosion generates networks of chutes during crater degradation, including examples that bifurcate and merge similar to Perseverance Valley (Cardenas et al., 2025). A more resistant bedrock knob in Perseverance Valley also might have deflected rockfall resulting in the bifurcation of the chute.

While Perseverance Valley appeared initially to be relatively unique along the crater rim in HiRISE imagery, rover observations revealed that Perseverance

Valley is not a valley, but rather a subtle chute. It is just meters wide with only decimeters of relief, similar in scale and texture to grooves in Marathon Valley as well as the grooves in the areas between the two valleys. The grooves may be analogous to the "rills" observed in rockfall flume studies (Beer et al., 2024a) or the "proto-chutes" in landscape evolution model runs (Cardenas et al., 2025). We argue that Perseverance Valley could be part of a suite of landforms—alcoves, chutes and grooves—potentially formed by rockfall erosion along much of the degraded crater rim (Figure 10a).

Faults and fractures might also have played a role in shaping the Endeavour rim by focusing aeolian abrasion (Fraeman et al., 2017; Crumpler et al., 2018; Sullivan et al., 2018) and rockfall erosion. Evidence of aeolian abrasion includes the planing off via saltating sand of weak Burns formation sulfate blocks ejected from craters in Meridiani Planum (Golombek et al., 2014); "tails" or stalks of weaker rock extending downwind behind more resistant material, ventifacts, and elongated surface pits in and around Endeavour crater (e.g., Sullivan et al., 2018); and contemporary dune migration in Endeavour (Chojnacki et al., 2011). However, unlike aeolian abrasion, rockfall does not require planes of weakness to produce bedrock chutes (Sun et al., 2022).

Our findings do not contradict the identification of groundwater-produced alteration products (Crumpler et al., 2016, 2017). Indeed, Perseverance Valley incises the Shoemaker formation but appears to stop before crossing the Burns formation on the crater floor. Most of the deflation of Endeavour crater is

hypothesized to have occurred in the Noachian prior to the Burns formation (Grant et al., 2016). If Perseverance Valley formed in the Noachian, water might have been present. However, substantially less water may be required to produce hydrated minerals in fractures than to incise a bedrock chute through fluvial flow. Moreover, the relatively fresh appearance of Perseverance Valley, being well-defined in imagery, combined with its low relief point to a potentially young landform that postdates the Noachian and thus formed when erosion attributed to aeolian activity is estimated to have been slow (Golombek et al., 2006). Likewise, the boulder fields downslope of Marathon Valley likely cover the Burns formation, and therefore rockfall there might post-date hypothesized times of aqueous activity. In this scenario, alteration products in the Shoemaker breccias may have been gradually exhumed by dry erosion processes. While we cannot rule out the presence of surface or subsurface water, we argue that it is plausible to develop the incised landforms on the Endeavour crater wall by dry processes.

The erosion rates generated by rockfall would ultimately be paced by the frequency of rockfall events. Such events could be triggered by marsquakes, generated either internally or by meteorite impacts, or volatile activity – seasonal changes in CO_2 frost, presence of brines, or pore water may be a driver/trigger of dry rockfall (e.g., Dickson et al., 2007; Levin et al., 2022). The spatial distribution of rockfall may indicate that multiple, spatially heterogeneous, or temporally variable forces are the drivers of rockfall events (Bickel et al., 2024). Rockfall events would need to occur repeatedly to incise deep bedrock valleys, likely

requiring thousands to millions of years (Cardenas et al., 2025), and thus the topography we see today might not be representative of the topography when the incised landforms formed. For example, the bedrock that once filled the gap in the crater rim topography just upslope of Perseverance Valley might have been the source for the rockfall events that created the initial Perseverance Valley topography. As rockfall shapes the landscape, new rocky escarpments can emerge, creating new rockfall generation sites. In this way, rockfall can self-perpetuate over substantial time (Cardenas et al., 2025).

Determining the process(es) driving crater rim incision at Endeavour helps contextualize geologic findings within a plausible paleoclimate – i.e., does the erosional regime require that this region was warm and wet, or could the environment have been desiccated? Here we demonstrated how dry rockfall incision might have taken the place of fluvial incision in crater wall degradation and landform development. Beyond local environments at Endeavour, considering dry processes as channelization mechanisms has implications for estimating Mars's water budget and environmental history. Bedrock chutes are widespread across Mars, and rockfall has been proposed as a dominant process in their formation (Levin et al., 2022). Dry rockfall abrasion could similarly contribute to ongoing crater degradation on other rocky planetary bodies, as well as cliff or scarp evolution on Earth.

6 CONCLUSIONS

We sought to evaluate whether dry rockfall abrasion could have shaped the Endeavour crater rim including Marathon Valley and Perseverance Valley. We mapped regions near Marathon Valley and Perseverance Valley with steep rocky outcrops that could be potential rockfall sources. We also identified scattered boulders and boulder fields downslope of these source regions, showing that rockfall has occurred. These observations are consistent with a numerical model of dry rockfall transport, which demonstrates that rockfall, sourced from regions with local slopes exceeding 45˚, can traverse the terrain of the rim despite relatively shallow (<20˚) slopes. The simulated rock impacts exhibit some concentration in topographic lows, such as the floor of Marathon Valley, which supports the idea that topographic funneling of rockfall can focus erosion, leading to the development of alcoves and chutes. Modeled impacts were more frequent in Marathon Valley than in Perseverance Valley, consistent with Perseverance Valley's fewer steep and rubbly outcrops, its more subtle and unresolved topographic expression, and the scarcity of boulders within the valley and downslope. Together our results show that dry rockfall is a plausible process of degradation at Endeavour crater. While we cannot rule out the presence of water, we argue that it is not necessary to explain the formation of bedrock grooves, chutes and alcoves on steep bedrock walls on Mars and other planets.

ACKNOWLEDGMENTS

This study was supported by NASA grant 80NSSC19K1269 to M.P. Lamb. O. A. K. is partially supported by a NASA FINESST award #80NSSC22K1373 (PI Bethany L. Ehlmann). We thank Abigail Fraeman for comments on initial drafts and discussion. We are thankful for the work by the MER Opportunity team that made in-situ observations possible. A portion of the research described in this paper was done by the Mars Exploration Rover project, Jet Propulsion Laboratory, California Institute of Technology, under a contract with the National Aeronautics and Space Administration (80NM0018D0004).

Open Research

HiRISE data are available publicly through the Orbital Data Explorer (ODE) NASA PDS node (https://ode.rsl.wustl.edu/mars/) and are also posted on the University of Arizona HiRISE website (https://www.uahirise.org/). The HiRISE DEM (product ID DTEEC_018701_1775_018846_1775_U01) is available on the Planetary Data System at https://pds-geosciences.wustl.edu/). LROC images may also be found on the PDS (https://pds.lroc.asu.edu/data/), or the image in Figure 1 may be downloaded here: https://wms.lroc.asu.edu/lroc/view_lroc/LRO-L-LROC-3-CDR-V1.0/M1391542697LC. The MER rover traverse and images may be viewed using the *Analyst's Notebook* (https://an.rsl.wustl.edu/mer/); individual calibrated images

may be found on the PDS (Maki, 2004; Bell, 2009) https://pds-geosciences.wustl.edu/mer/mer1-m-pancam-3-radcal-sci-v2/mer1pc_1002/ and https://pds-geosciences.wustl.edu/mer/mer1-m-navcam-3-radiometric-sci-v1/mer1nc_1xxx/. Pancam mosaics (Bell et al., 2005) are on the Arizona State University Pancam website: http://pancam.sese.asu.edu/images.html. Code for the numerical model may be found here: https://doi.org/10.26207/rdex-en91 (Cardenas et al., 2023) and is described further in Cardenas et al., 2025. The code was modified from Beer et al., 2024b, which is in a repository here: https://fdat.uni-tuebingen.de/records/98546-hfv72.

REFERENCES

Armitage, J.J., Warner, N.H., Goddard, K., & Gupta, S. (2011). Timescales of alluvial fan development by precipitation on Mars. *Geophysical Research Letters, 38.* https://doi.org/10.1029/2011GL048907

Arvidson, R. E., Squyres, S. W., Bell, J. F., Catalano, J. G., Clark, B. C., Crumpler, L. S., et al. (2014). Ancient aqueous environments at Endeavour crater, Mars. *Science, 343*(6169), 1248097, https://doi.org/10.1126/science.1248097

Bamber et al. (2022). Constraining the formation of paleolake inlet valleys across crater rims. *Icarus 378*, 114945, https://doi.org/10.1016/j.icarus.2022.114945

Beer, A. R., Lamb, M. P., Ulizio, T. P., Ma, Z., Hughes, M. N., Fraeman, A. A., et al. (2019). Bedrock gully formation by dry rockfall. In *Ninth International Conference on Mars*, Abstract # 6084, LPI, Pasadena, 2019. Retrieved from https://www.hou.usra.edu/meetings/ninthmars2019/pdf/6431.pdf

Beer, A. R. and Lamb, M. P. (2021). Abrasion regimes in fluvial bedrock incision. *Geology 49* (6): 682–386, https://doi.org/10.1130/G48466.1

Beer, A. R., Fischer, J. N., Ulizio, T. P., Ma, Z., Sun, Z., & Lamb, M. P. (2024a). A mechanistic model and experiments on bedrock incision and channelization by rockfall. *Journal of Geophysical Research: Earth Surface, 129*, e2023JF007504, https://doi.org/10.1029/2023JF007504

Beer, A. R., Fischer, J. N., Luizio, T. P., Ma, Z., Sun, Z., & Lamb, M. P. (2024b). Experimental data and modelling code for bedrock incision and channelization by dry rockfall [Data set]. University of Tübingen. https://doi.org/10.57754/FDAT.98546-hfv72

Bell, J. F., III, et al. (2003). Mars Exploration Rover Athena Panoramic Camera (Pancam) investigation. *Journal of Geophysical Research, 108(E12*), 8063, https://doi.org/10.1029/2003JE002070

Bell III, J.F., H.M. Arneson, W.H. Farrand, W. Goetz, A.G. Hayes, K. Herkenhoff, M.J. Johnson, J.R. Johnson, J. Joseph, K. Kinch, M.T. Lemmon, M.B. Madsen, E. McCartney, R.V. Morris, J. Proton, D. Savransky, F. Seelos, J. Soderblom, J.N. Sohl-Dickstein, R.J. Sullivan, M.J. Wolff, and the Athena Science Team. (2005). Large multispectral and albedo panoramas acquired by the Pancam instruments on the Mars Exploration Rovers *Spirit and Opportunity*. In *Lunar and Planetary Science XXXVI*, Abstract #1337, LPI, Houston, 2005. [images posted at http://pancam.sese.asu.edu/mosaics.html]

Bell, J. (2009). 'MER 1 Mars Navcam Radiometrically Calibrated RDR V1.0', NASA Planetary Data System, MER1-M-NAVCAM-3-RADIOMETRIC-SCI-V1.0. [Dataset]. https://doi.org/10.17189/1520327

Bickel, V. T., Daubar, I. J., Sokolowska, A. J., Bonab, A., Haut, I., & Conway, S. J. (2024). The first global catalog of rockfall locations on Mars. *Geophysical Research Letters, 51*, e2024GL110674, https://doi.org/10.1029/2024GL110674

Cardenas, B., Beer, A., Donohoe, P., Kanine, O., Dickson, J., and Lamb, M. (2023). Model and data for "Crater-wall degradation and bedrock-chute formation from dry rockfall erosion" [Data set]. Scholarsphere. https://doi.org/10.26207/rdex-en91

Cardenas, B., Beer, A., Donohoe, P., Kanine, O., Dickson, J., and Lamb, M. (2025). Crater-wall degradation and bedrock-chute formation from dry rockfall erosion. *Geology, 53,* p. 456-460, https://doi.org/10.1130/G53096.1

Chojnacki, M., Burr, D. M., Moersch, J. E., and Michaels, T. I. (2011). Orbital observations of contemporary dune activity in Endeavor *[sic]* crater, Meridiani Planum, Mars. *Journal of Geophysical Research 116*, E00F19, https://doi.org/10.1029/2010JE003675

Christensen, P.R. (2003). Formation of recent martian gullies through melting of extensive water-rich snow deposits. *Nature 422*, 45–48, https://doi.org/10.1038/nature01436

Costard, F., Forget, F., Mangold, N., Peulvast, J.P. (2002). Formation of recent martian debris flows by melting of near-surface ground ice at high obliquity. *Science 295*, 110–113, https://doi.org/10.1126/science.1066698

Craddock, R.A. and Howard, A.D. (2000). Simulated degradation of lunar impact craters and a new method for age dating farside mare deposits. *Journal of Geophysical Research*, 105(E8), 20387–20401, https://doi.org/10.1029/1999JE001099

Crumpler, L. S., Arvidson, R. E., Mittlefehldt, D. W., Jolliff, B. L., Farrand, W. H., Fox, V., Golombek, M. P. and the Athena Science Team (2016). Opportunity, geologic and structural context of aqueous alteration in Noachian outcrops, Marathon Valley and rim of Endeavour crater. In *Lunar and Planetary Science XLVII,* Abstract # 2272, LPI, Houston, 2016. Retrieved from: https://www.hou.usra.edu/meetings/lpsc2016/pdf/2272.pdf

Crumpler, L. S., Arvidson, R. E., Golombek, M., Grant, J. A., Jolliff, B. L., Mittlefehldt, D. W., and the Athena Science Team (2017). Rim structure, stratigraphy, and aqueous alteration exposures along Opportunity rover's traverse of the Noachian Endeavour crater. In *Lunar and Planetary Science XLVIII,* Abstract # 2276, LPI, Houston, 2017. Retrieved from: https://www.hou.usra.edu/meetings/lpsc2017/pdf/2276.pdf

Crumpler, L. S. and the MER Athena Science Team (2018). In situ mapping of fault-control and regolith diversity at the head of Perseverance valley, Endeavour crater, Mars. In *Lunar and Planetary Science XLVIV,* Abstract # 2205, LPI, Houston, 2018. Retrieved from: https://www.hou.usra.edu/meetings/lpsc2018/pdf/2205.pdf

Day, M., Anderson, W., Kocurek, G., and Mohrig, D. (2016). Carving intracrater layered deposits with wind on Mars. *Geophysical Research Letters, 43*, 2473–2479, https://doi.org/10.1002/2016GL068011

Dickson, J.L., Head, J.W., Kreslavsky, M. (2007). Martian gullies in the southern mid-latitudes of Mars: Evidence for climate-controlled formation of young fluvial features based upon local and global topography. *Icarus 188*, 315–323, https://doi.org/10.1016/j.icarus.2006.11.020

DiBiase, R.A., Lamb, M.P., Ganti, V., and Booth, A.M. (2017). Slope, grain size, and roughness controls on dry sediment transport and storage on steep hillslopes. *Journal of Geophysical Research: Earth Surface, 122*, p. 941–960, https://doi.org/10.1002/2016JF003970

Diniega, S., Byrne, S., Bridges, N.T., Dundas, C.M., McEwen, A.S. (2010). Seasonality of present-day Martian dune-gully activity. *Geology 38*, 1047–1050, https://doi.org/10.1130/G31287.1

Dundas, C.M., McEwen, A.S., Diniega, S., Byrne, S., Martinez-Alonso, S. (2010). New and recent gully activity on Mars as seen by HiRISE. *Geophysical Research Letters, 37,* L07202, https://doi.org/10.1029/2009GL041351

Dundas, C. M., Diniega, S., and McEwen, A. S. (2015). Long-term monitoring of martian gully formation and evolution with MRO/HiRISE, *Icarus, 251*, 244-263, https://doi.org/10.1016/j.icarus.2014.05.013

Fassett, C. I., and Thomson, B. J. (2014). Crater degradation on the lunar maria: Topographic diffusion and the rate of erosion on the Moon. *Journal of Geophysical Research: Planets, 119*, 2255–2271, https://doi.org/10.1002/2014JE004698

Fraeman, A. et al. (2017). Opportunity observations of grooves in Endeavour crater's rim. In *Lunar and Planetary Science XLVIII,* Abstract # 2196, LPI, Houston, 2017. Retrieved from: https://www.hou.usra.edu/meetings/lpsc2017/pdf/2196.pdf

Gilbert, G. K. (1909). The Convexity of Hilltops. *The Journal of Geology*, *17*(4), 344–350. http://www.jstor.org/stable/30057970

Golombek, M. P. et al. (2014). Small crater modification on Meridiani Planum and implications for erosion rates and climate change on Mars. *Journal of Geophysical Research: Planets*, *119*, 2522–2547, https://doi.org/10.1002/2014JE004658

Golombek, M. P., et al. (2006). Erosion rates at the Mars Exploration Rover landing sites and long-term climate change on Mars. *Journal of Geophysical Research*, 111, E12S10, https://doi.org/10.1029/2006JE002754

Grant, J.A., et al. (2006). Crater gradation in Gusev crater and Meridiani Planum, Mars. *Journal of Geophysical Research,* 111, E02S08. https://doi.org/10.1029/2005JE002465

Grant, J. A., Parker, T. J., Crumpler, L.S., Wilson, S. A., Golombek, M. P., Mittlefehldt, B. W. (2016). The degradational history of Endeavour crater, Mars. *Icarus, 280*, p. 22-36, https://doi.org/10.1016/j.icarus.2015.08.019

Grotzinger, J. P., et al. (2005). Stratigraphy and sedimentology of a dry to wet eolian depositional system, Burns formation, Meridiani Planum, Mars. *Earth and Planetary Science Letters*, *240*(1), 11–72, https://doi.org/10.1016/j.epsl.2005.09.039

Hartmann, W.K. and Neukum, G. (2001). Cratering chronology and the evolution of Mars. *Space Science Reviews, 96*, 165-194, https://doi.org/10.1023/A:1011945222010

Hartmann, W. K. (2005). Martian cratering 8: Isochron refinement and the chronology of Mars. *Icarus, 174*, 2, 294-320, https://doi.org/10.1016/j.icarus.2004.11.023.

Howard, A. D. (2007). Simulating the development of Martian highland landscapes through the interaction of impact cratering, fluvial erosion, and variable hydrologic forcing. *Geomorphology 91*, 332–363. https://doi.org/10.1016/j.geomorph.2007.04.017

Hugenholtz, C.H. (2008). Frosted granular flow: A new hypothesis for mass wasting in martian gullies. *Icarus, 197*, 65–72, https://doi.org/10.1016/j.icarus.2008.04.010.

Hughes, M. N., Arvidson, R. E., Grant, J. A., Wilson, S. A., Howard, A. D., & Golombek, M. P. (2019). Degradation of Endeavour crater based on orbital and rover-based observations in combination with landscape evolution modeling. *Journal of Geophysical Research: Planets*, 124, 1472–1494. https://doi.org/10.1029/2019JE005949

Ishii, T., & Sasaki, S. (2004). Formation of recent Martian gullies by avalanches of CO2 frost. In *Lunar and Planetary Science XXXV,* Abstract # 1556, LPI, Houston, 2004. Retrieved from: https://www.lpi.usra.edu/meetings/lpsc2004/pdf/1556.pdf

Kolb, K. J., Pelletier, J. D., & McEwen, A. S. (2010). Modeling the formation of bright slope deposits associated with gullies in Hale Crater, Mars: Implications for recent liquid water. *Icarus*, *205*(1), 113-137, https://doi.org/10.1016/j.icarus.2009.09.009

Kumar, P.S., Keerthi, V., Kumar, A.S., Mustard, J., Krishna, B.G., Amitabh, Ostrach L.R., Kring, D.A., Kumar, A.S.K., Goswami, J.N. (2013). Gullies and landslides on the moon: Evidence for dry-granular flows. *Journal of Geophysical Research: Planets 118*, 206–223, https://doi.org/10.1002/jgre.20043.

Levin, J. N., Dickson, J. L., & Lamb, M. P. (2022). Evaluating the role of volatiles in bedrock chute formation on the Moon and Mars. *Icarus*, 373, 114774. https://doi.org/10.1016/j.icarus.2021.114774

Maki, J. N., et al., (2003). Mars Exploration Rover engineering cameras. *Journal of Geophysical Research, 108(*E12*),* 8071, https://doi.org/10.1029/2003JE002077

Maki, J. N., (2004). MER 1 Mars Panoromic Camera Mosaic Images Ops RDR V1.0, NASA Planetary Data System, MER1-M-PANCAM-5-MOSAIC-OPS-V1.0. [Dataset]. https://doi.org/10.17189/1520361

Malin, M. C. and Edgett, K. S. (2000). Evidence for recent groundwater seepage and surface runoff on Mars. *Science 288*, 2330–2335. https://doi.org/10.1126/science.288.5475.2330

McEwen, A.S., Eliason, E.M., Bergstrom, J.W., Bridges, N.T., Hansen, C.J., Delamere, W. A., Grant, J.A., Gulick, V.C., Herkenhoff, K.E., Keszthelyi, L., Kirk, R.L., Mellon, M.T., Squyres, S.W., Thomas, N., Weitz, C.M., (2007). Mars Reconnaissance Orbiter's High Resolution Imaging Science Experiment (HiRISE*). Journal of Geophysical Research: Planets*, 112, E05S02, https://doi.org/10.1029/2005JE002605

Palucis, M., Jasper, J., Garcynski, B., and Dietrich, W. E. (2020). Quantitative assessment of uncertainties in modeled crater retention ages on Mars. *Icarus, 341*, https://doi.org/10.1016/j.icarus.2020.113623.

Parker, T. J., Golombek, M. and the Athena Science Team (2018). Origin of Perseverance Valley by spillover of a small lake. In *Lunar and Planetary Science XLVIV,* Abstract # 2623, LPI, Houston, 2018. Retrieved from https://www.hou.usra.edu/meetings/lpsc2018/pdf/2623.pdf

Pelletier, J.D. (2008). *Quantitative Modeling of Earth Surface Processes*. Cambridge University Press. https://doi.org/10.1017/CBO9780511813849

Pelletier, J.D., Kolb, K.J., McEwen, A.S., and Kirk, R.L. (2008). Recent bright gully deposits on Mars: Wet or dry flow? *Geology*, *36*, p. 211-214, https://doi.org/10.1130/G24346A.1.

Pilorget, C., and Forget, F. (2016). Formation of gullies on Mars by debris flows triggered by CO2 sublimation. *Nature Geoscience, 9*, p. 65–69, https://doi.org/10.1038/ngeo2619.

Roering, J. J., J. W. Kirchner, and W. E. Dietrich (1999). Evidence for nonlinear, diffusive sediment transport on hillslopes and implications for landscape morphology. *Water Resources Research*, 35(3), 853–870, https://doi.org/10.1029/1998WR900090.

Roering, J. J., J. W. Kirchner, and W. E. Dietrich (2001). Hillslope evolution by nonlinear, slope-dependent transport: Steady state morphology and equilibrium adjustment timescales. *Journal of Geophysical Research*, *106(B8)*, 16499–16513, https://doi.org/10.1029/2001JB000323

Squyres, S. W., Arvidson, R. E., Golombek, M., Fraeman, A., Lamb, M., Palucis, M., Parker, T. J. and the Athena Science Team (2018). Opportunity's exploration of Perseverance Valley. In *Lunar and Planetary Science XLVIV,* Abstract # 1758, LPI, Houston, 2018. Retrieved from https://www.hou.usra.edu/meetings/lpsc2018/pdf/1758.pdf

Sun, Z., et al. (2022). Formation of low-gradient bedrock chutes by dry rockfall on planetary surfaces. *Geology*, *50*, p. 174–178, https://doi.org/10.1130/G49286.1

Sullivan, R., Banfield, D., Bell, J., et al. (2005). Aeolian processes at the Mars Exploration Rover Meridiani Planum landing site. *Nature 436*, 58–61. https://doi.org/10.1038/nature03641

Sullivan et al. (2018). Multiple working hypotheses at Perseverance Valley: Fracture and aeolian abrasion. In *Lunar and Planetary Science XLVIV,* Abstract # 2516, LPI, Houston, 2018. Retrieved from https://www.hou.usra.edu/meetings/lpsc2018/pdf/2516.pdf

Sweeney, J., Warner, N. H., Ganti, V., Golombek, M. P., Lamb, M. P., Fergason, R., & Kirk, R. (2018). Degradation of 100-m-scale rocky ejecta craters at the InSight landing site on Mars and implications for surface processes and erosion rates in the Hesperian and Amazonian. *Journal of Geophysical Research: Planets, 123*, 2732–2759. https://doi.org/10.1029/2018JE005618

Sylvest, M.E., Conway, S.J., Patel, M.R., Dixon, J.C., and Barnes, A. (2016). Mass wasting triggered by seasonal CO2 sublimation under Martian atmospheric conditions: Laboratory experiments. *Geophysical Research Letters, v. 43*, p. 12,363–12,370, https://doi.org/10.1002/2016GL071022.

Tebolt, M., Levy, J., Goudge, T. and Schorghofer, N. (2020). Slope, elevation, and thermal inertia trends of martian recurring slope lineae initiation and termination points: Multiple possible processes occurring on coarse, sandy slopes. *Icarus*, *338*, 113536, https://doi.org/10.1016/j.icarus.2019.113536

Vijayan, S., Harish, Kimi, K., Tuhi, S., Vigneshwaran, K., Sinha, R., et al. (2021). Boulder fall ejecta: Present day activity on Mars. *Geophysical Research Letters*, *49*(1), https://doi.org/10.1029/2021gl096808

FIGURES

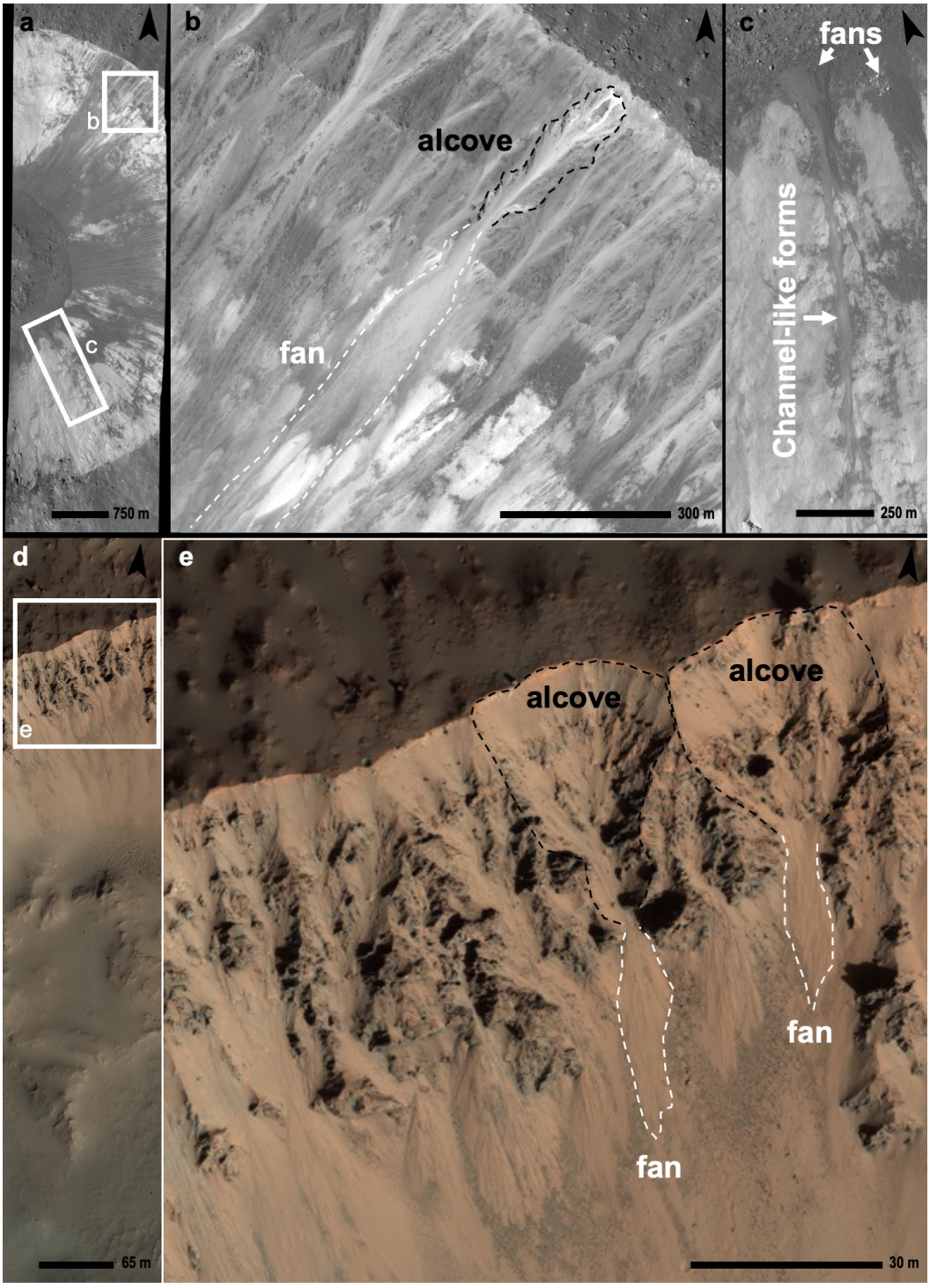

Figure 1: Examples of chute morphologies on the Moon and Mars. Panels **a**, **b**, and **c** show alcoves, chutes and fans in a low-latitude lunar crater captured in LROC image M152451994R. Panels **d** and **e** show alcoves, bedrock chutes and fans on the rim of a martian crater captured by HiRISE image ESP_019120_1585, centered at ~-21˚latitude.

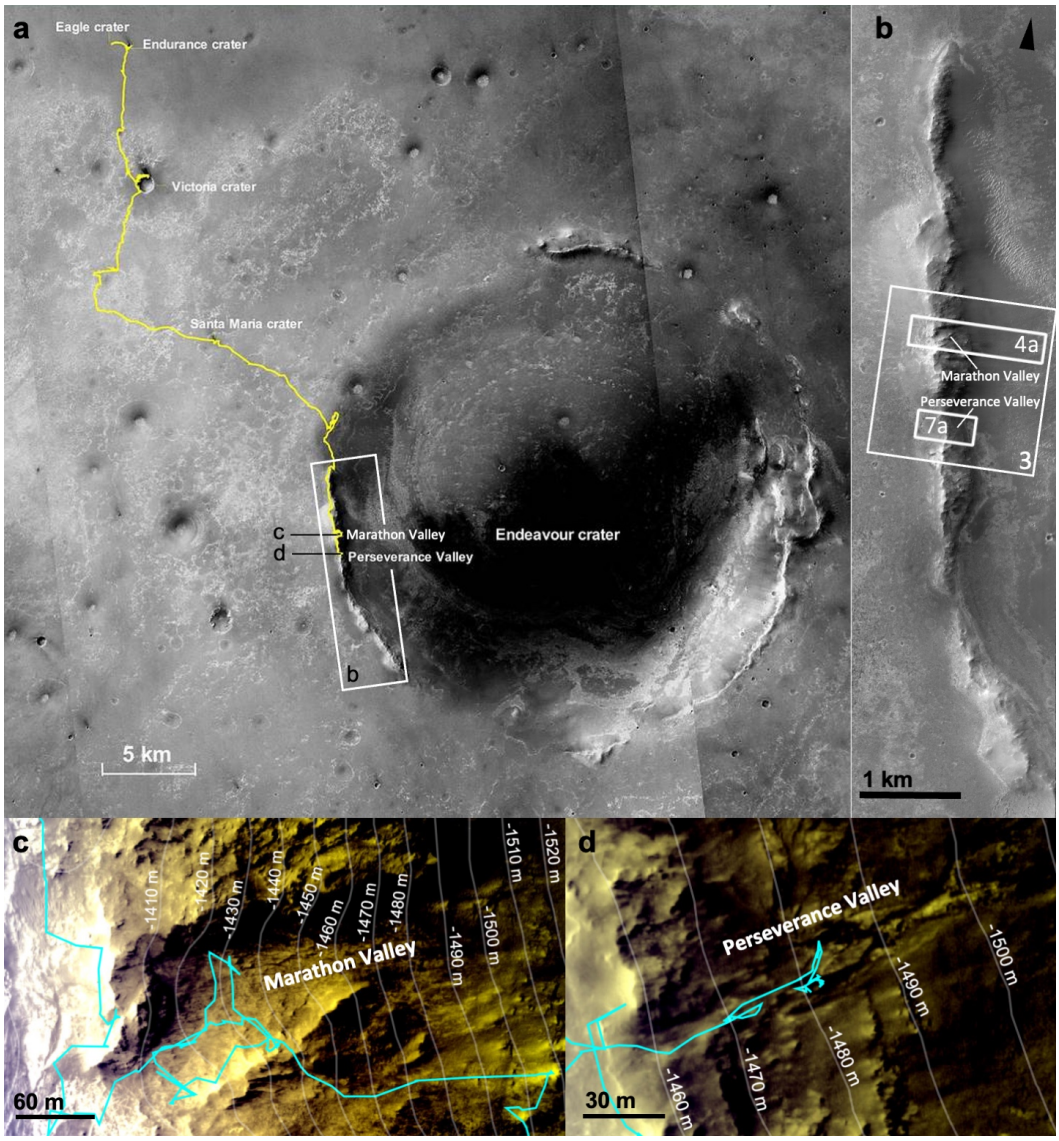

Figure 2: Orbital views of Endeavour crater, Perseverance Valley, and Marathon Valley**. a**. MER Opportunity traverse (yellow) overlaid on NASA Mars Reconnaissance Orbiter Context Camera images B02_010486_1779_XN_02S005W, P15_006847_1770_XN_03S005W, and P13_006135_1789_XN_01S005W. Credit: NASA/JPL-Caltech/MSSS/NMMNHS. **b**. HiRISE image ESP_018701_1775 of the western rim of Endeavour crater, with locations of Figures 3, 4a and 7a noted. Panels **c** and **d** show Opportunity traverse (teal line) details in Marathon Valley and Perseverance Valley, respectively. Basemaps were constructed from three HRSC bands fused with a HiRISE mosaic. 10 meter contours (white lines) are derived from HiRISE DEMs. Basemap details may be found in the *Analyst's Notebook* under "Traverse Map" at https://an.rsl.wustl.edu/help/Content/Using%20the%20Notebook. North is up in all images except panel **b** where indicated.

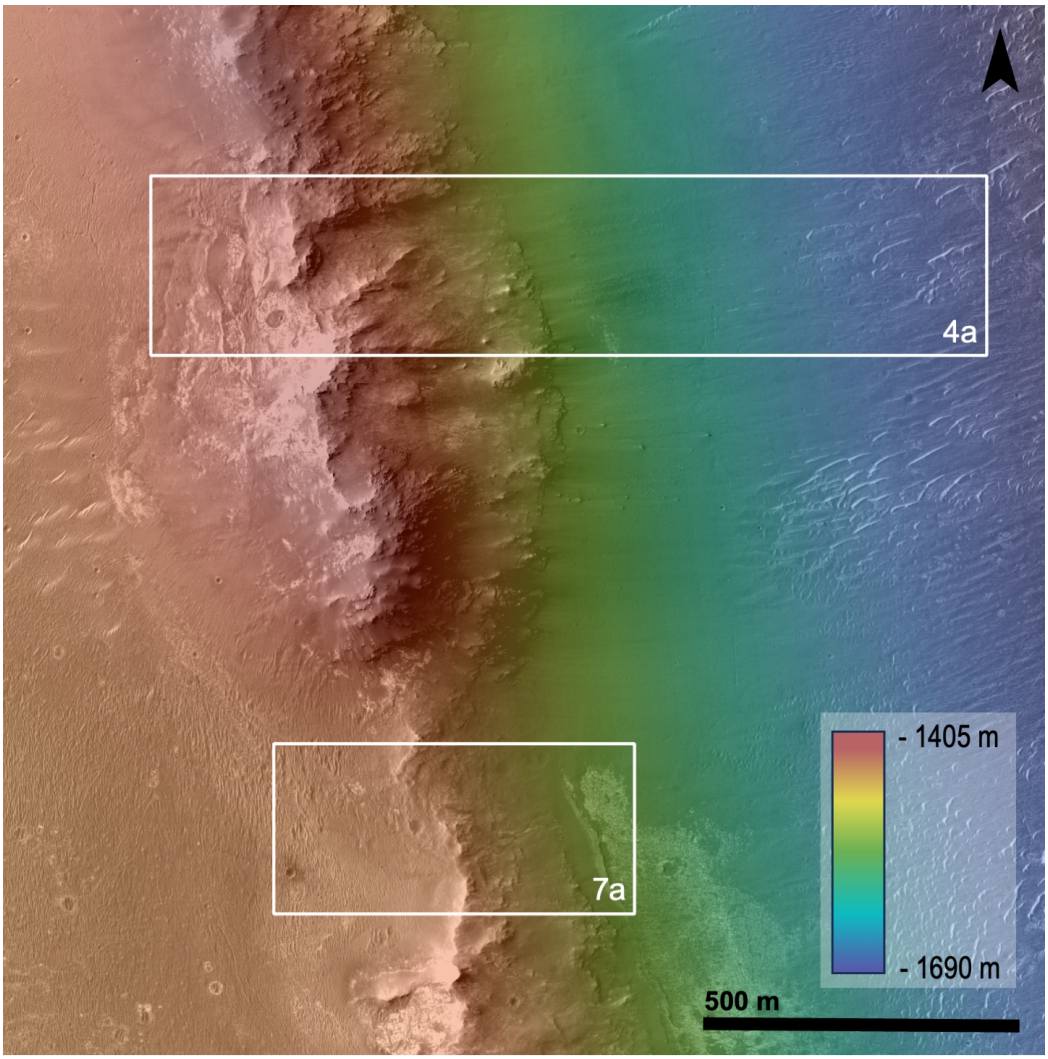

Figure 3: HiRISE image ESP_018701_1775 overlaid with partially transparent HiRISE DEM. Boxed locations show the locations of Figure 4a (Marathon Valley) and 7a (Perseverance Valley).

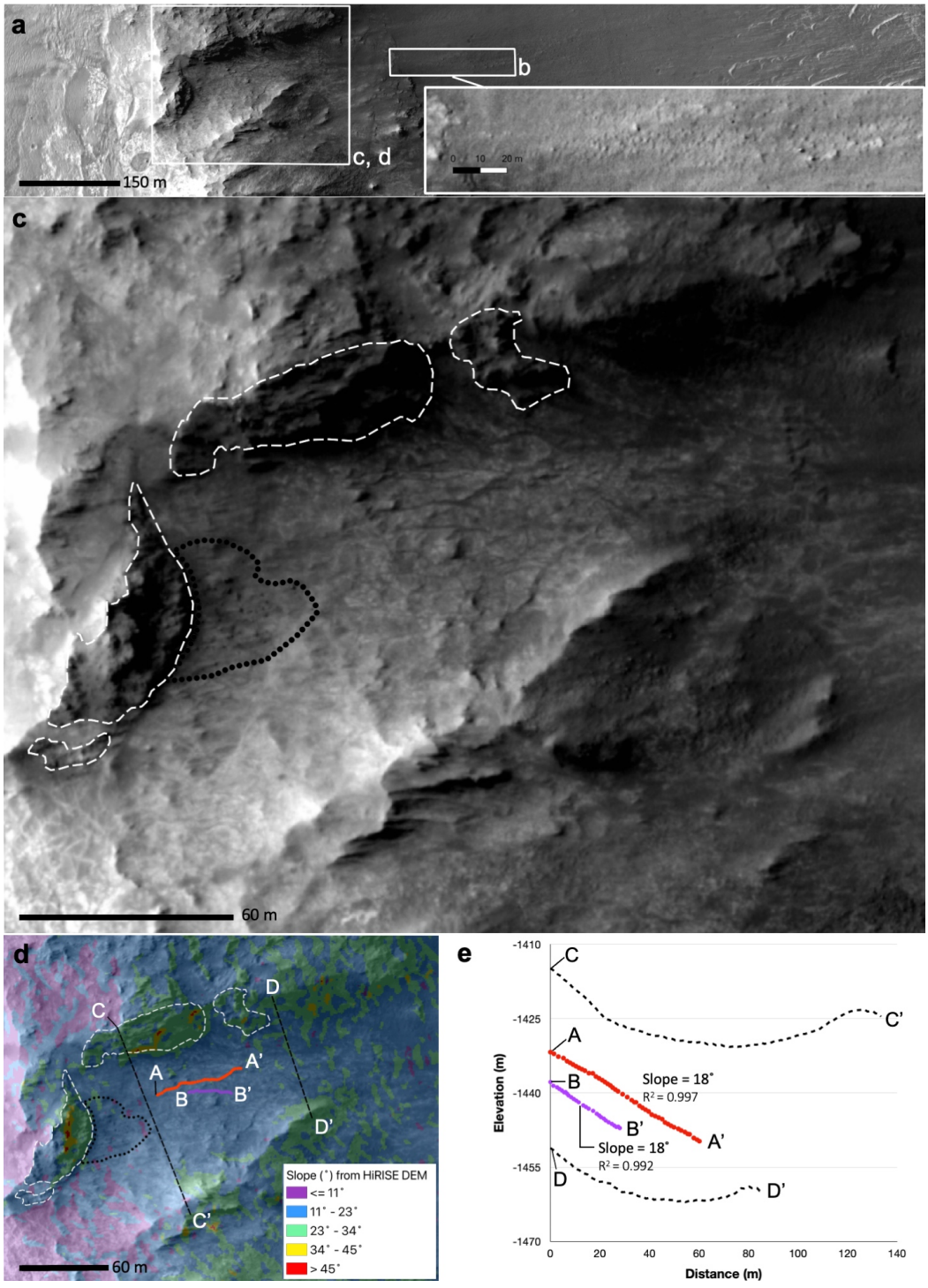

Figure 4: Marathon Valley. Parts **a**-**d** use HiRISE image ESP_018701_1775. The extent of **a** is shown in Fig. 2b. Part **a** shows an overview of Marathon valley, with locations of parts **c** and **d**. Inset **b** shows a boulder field downslope of Marathon Valley. **c**: Detail view of Marathon Valley with outlines of steep rubbly outcrops that are potential sources of rockfall in dashed white lines …

Figure 4 caption, continued: … and a boulder field in dotted black line. Just downslope of the boulder field is a series of dark-toned lineations, shown as the grooves in Figure 5. The same area as **c** is shown in part **d**, with a partially transparent slope map overlaid on the HiRISE image. Traces of two of the linear downslope features are in red and purple dotted lines, and two valley cross-sections are in dashed black lines. The profiles of these features are shown in part **e**, with two times vertical exaggeration.

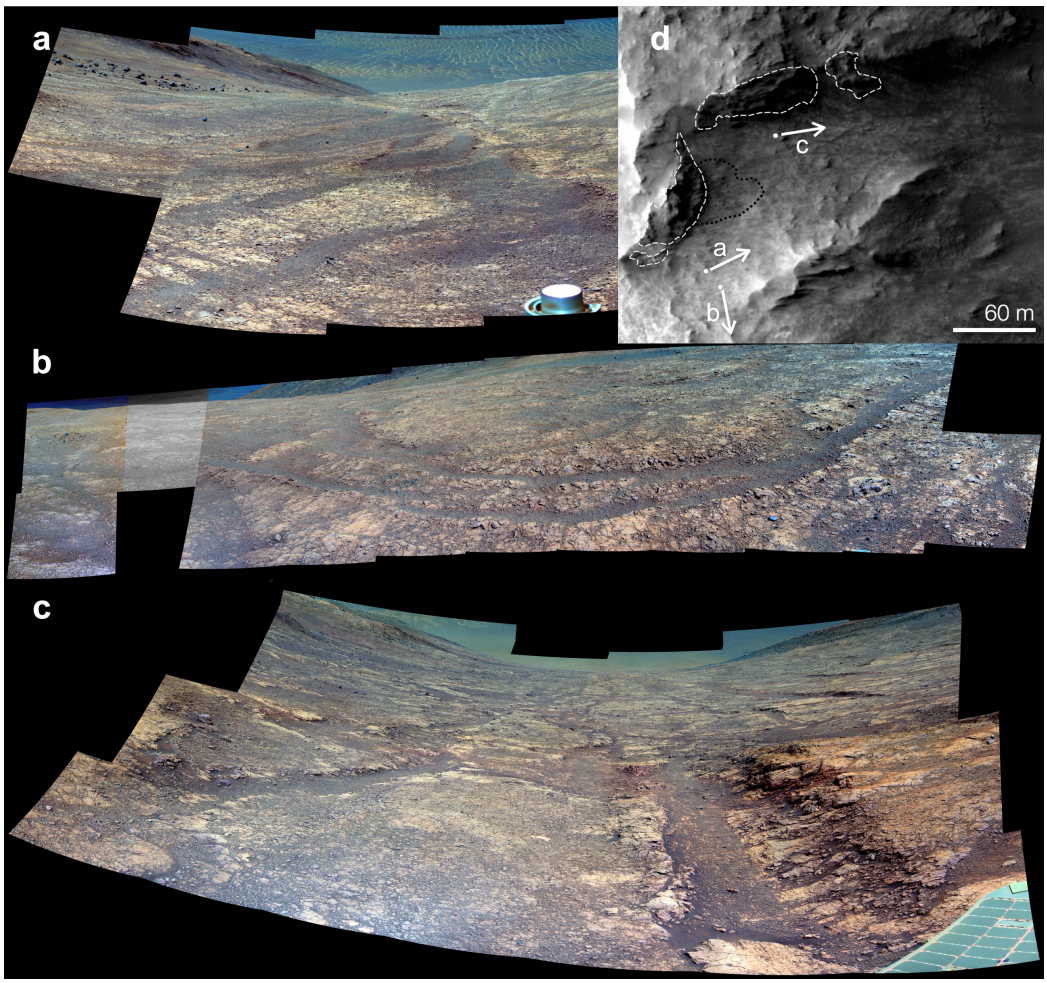

Figure 5: Multiple views of grooved terrain in Marathon Valley at three points in Opportunity's traverse. The topographic depressions are filled with dark sand and diverge and rejoin around light-toned rocky substrate. **a**: Pancam sol 4424. Note the boulder field in upper left of image. **b**: Pancam sol 4338. **c**: Pancam sol 4461. Rover locations and approximate look directions for these figures are in part **d**, which uses HiRISE image ESP_018701_1775 and the same extent as **Figure 4c**.

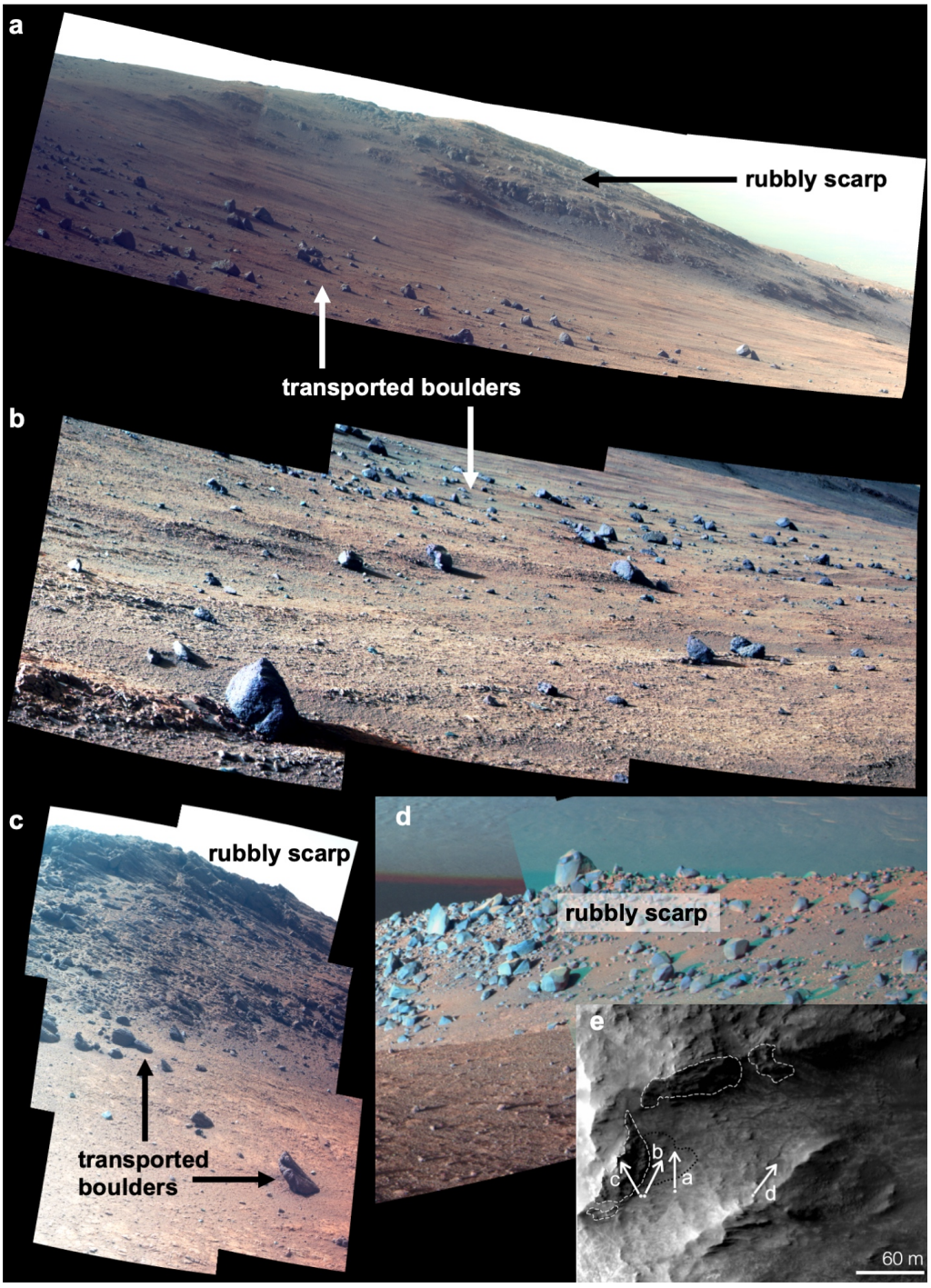

Figure 6: Pancam images of rubbly scarps and transported boulders in Marathon Valley. All images are of enhanced color to highlight subtle differences. **a**: Sol 4104, north wall of Marathon Valley. **b**: Sol 4092, rock survey near head of Marathon Valley. **c**: Sol 4082, north wall. **d**: Sol 4267 (cropped), ridge on southeast rim of the valley. Rover locations and approximate look directions are in **e**, which uses HiRISE image ESP_018701_1775 and the same extent as **Figure 4c**.

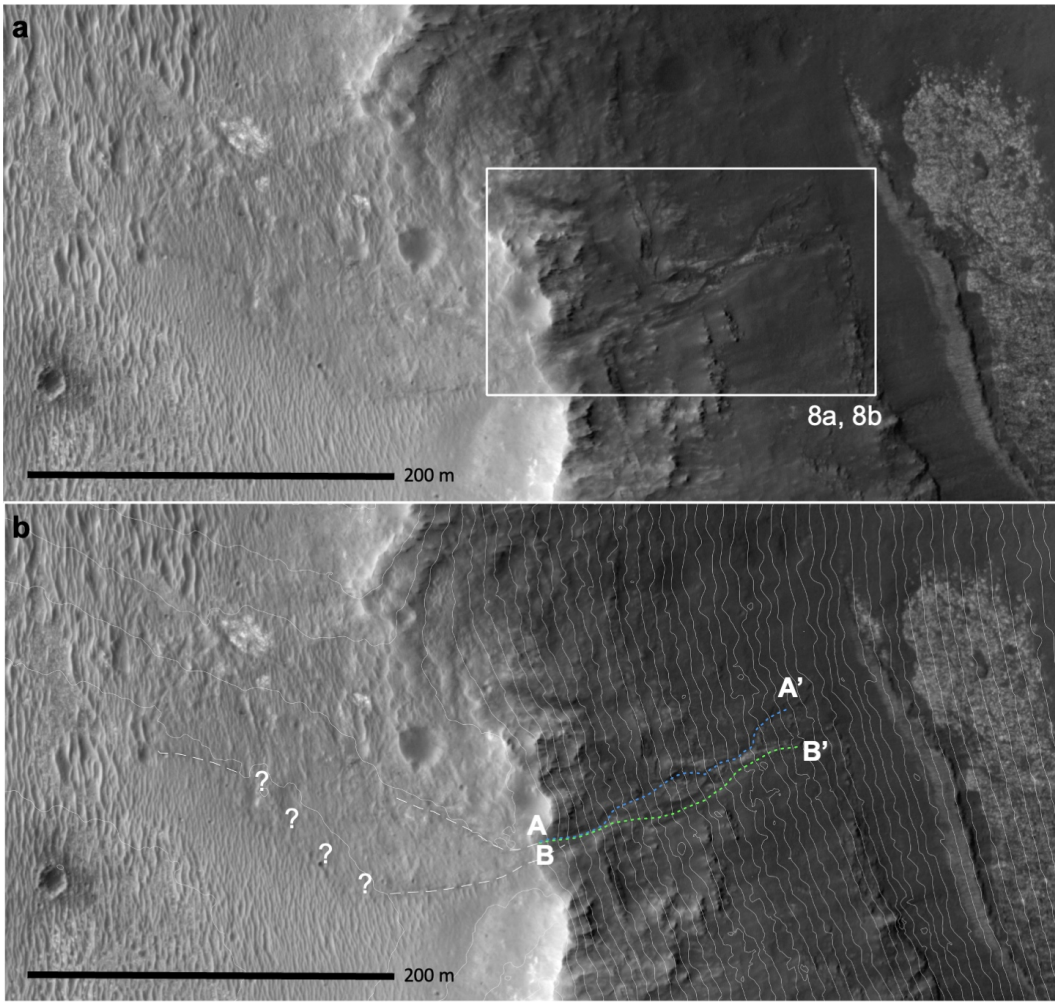

Figure 7: Overview of Perseverance Valley, HiRISE image ESP_018701_1775. The extent is shown in context of the crater rim in **Figures 2b and 3**. Part **a** shows the location of panels in **Figure 8**. The image is overlain with 2 m contours in part **b**. In this part, the locations of two darker-toned grooves leading from the surrounding terrain to the mouth of the valley are marked by white dashed lines. The traces of two grooves in Perseverance Valley are shown in blue and green dotted lines.

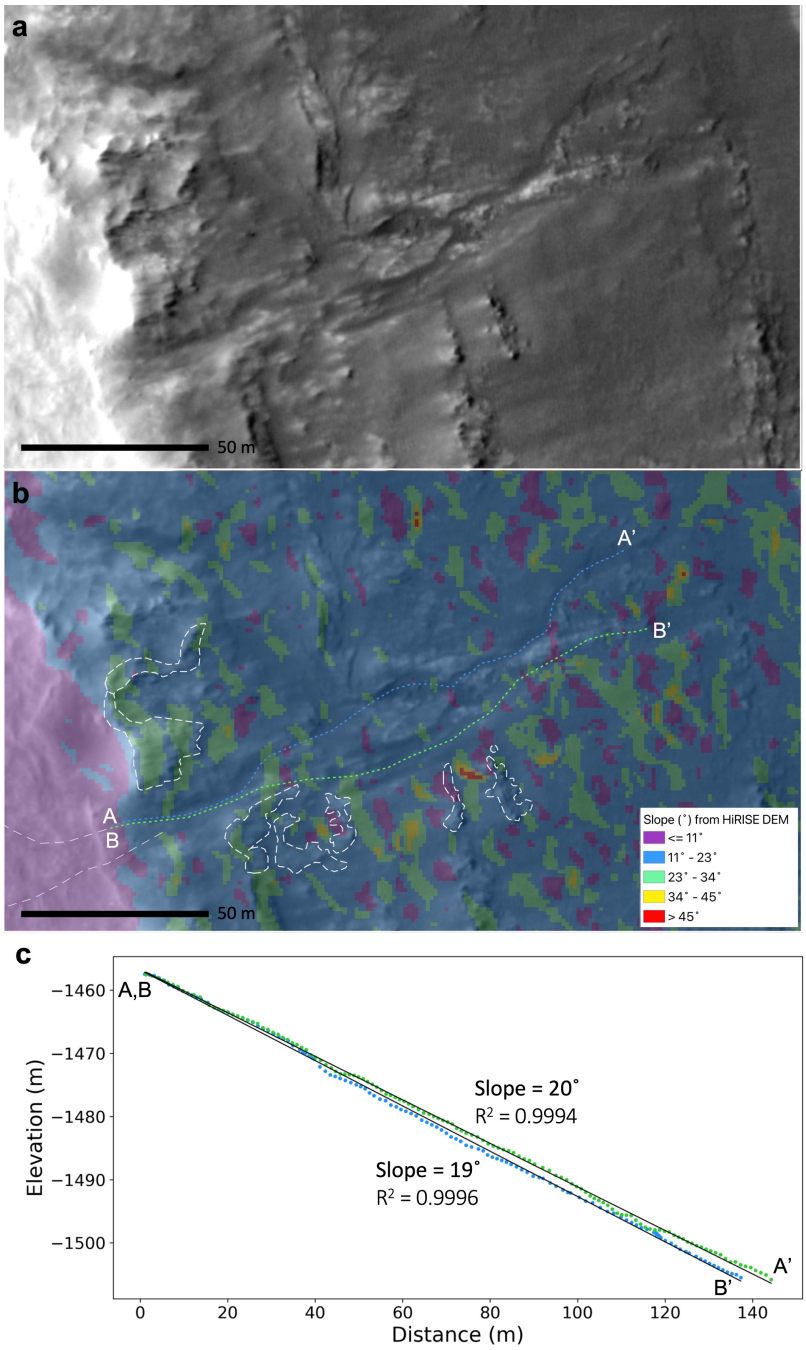

Figure 8: Detail view of Perseverance Valley is shown in **a** and **b,** extents shown in **Figure 7a**. HiRISE image is overlain with slope map in part **b**, with rubbly outcrops outlined in bold white dashed line, the dark-toned features on the highland terrain discussed in **Figure 7** in fine white dashed line, and the traces of grooves shown in blue and green dotted lines. The long profiles of these grooves are shown in **c**.

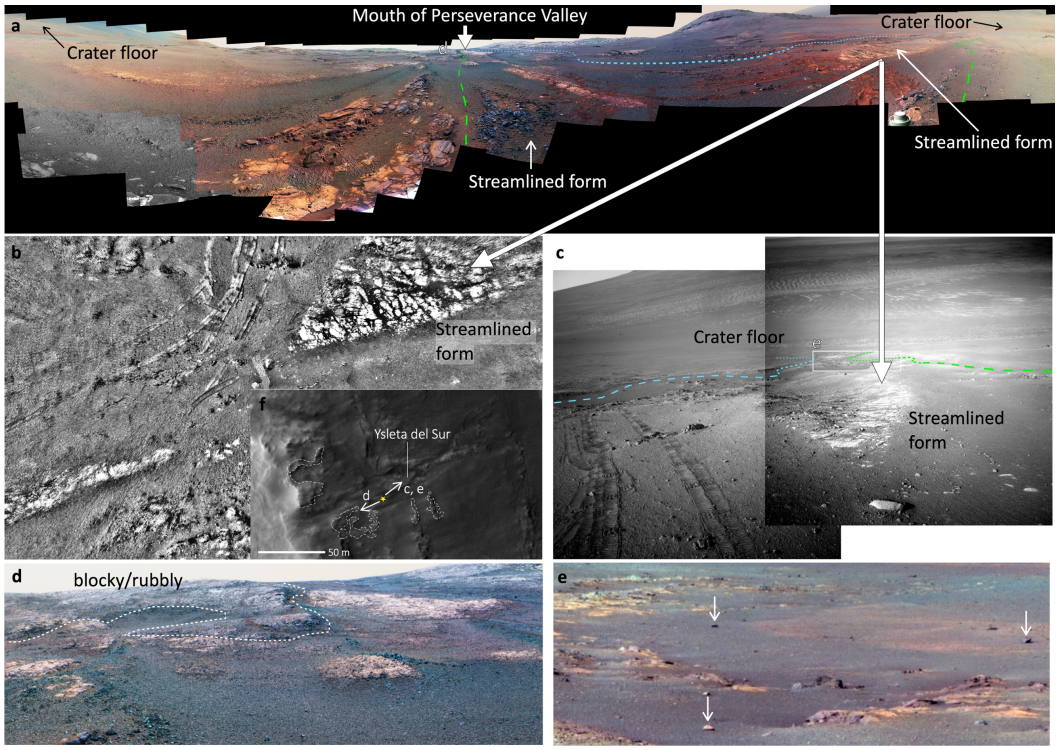

Figure 9: Grooves in Perseverance Valley. **a**: Enhanced color 360˚"Legacy Panorama," of 354 images taken on sols 5,084 through 5,111 by Opportunity's Pancam. Regolith-filled linear depressions incise lighter-toned rock. To the far left and right in the panorama the crater floor is visible. Near the center of the image is a streamlined form of dark-toned vesicular rock, and on the right is a light-toned streamlined form called "Ysleta del Sur." This outcrop also appears parts **b** and **c**. Green and blue dotted lines approximate the channel traces of grooves in Figure 8. Location of part **d** is noted near the mouth of the valley. Part **b** is a mosaic of Navcam images. Distance between the Opportunity rover wheels is ~ 1 m. Part **c** shows Yselta del Sur in sol 4997 Navcam images, looking toward the crater floor, and notes the approximate location of part **e**. Note imprints of rover wheels in tracks demonstrate that the dark regolith is composed of fine-grained sandy material, which also fills the grooves. The rubbly outcrops identified from orbit in Figure 8 are shown from the ground in a cropped portion of the Legacy Panorama in **d**. **e**: Boulders both within and outside of the depressions as seen in Pancam sol 5030. **f**: A summary of viewing directions show in planview on HiRISE image image ESP_018701_1775, same extent as **Figure 8a**. After sol 4997 until the end of the mission, the rover remained in a relatively small area just east (upslope) of the streamlined form Yselta del Sur; this location is approximated with a yellow star. **c** and **e** look downslope (~ENE) toward the crater floor; **d** looks upslope (~WSW) toward the valley mouth.

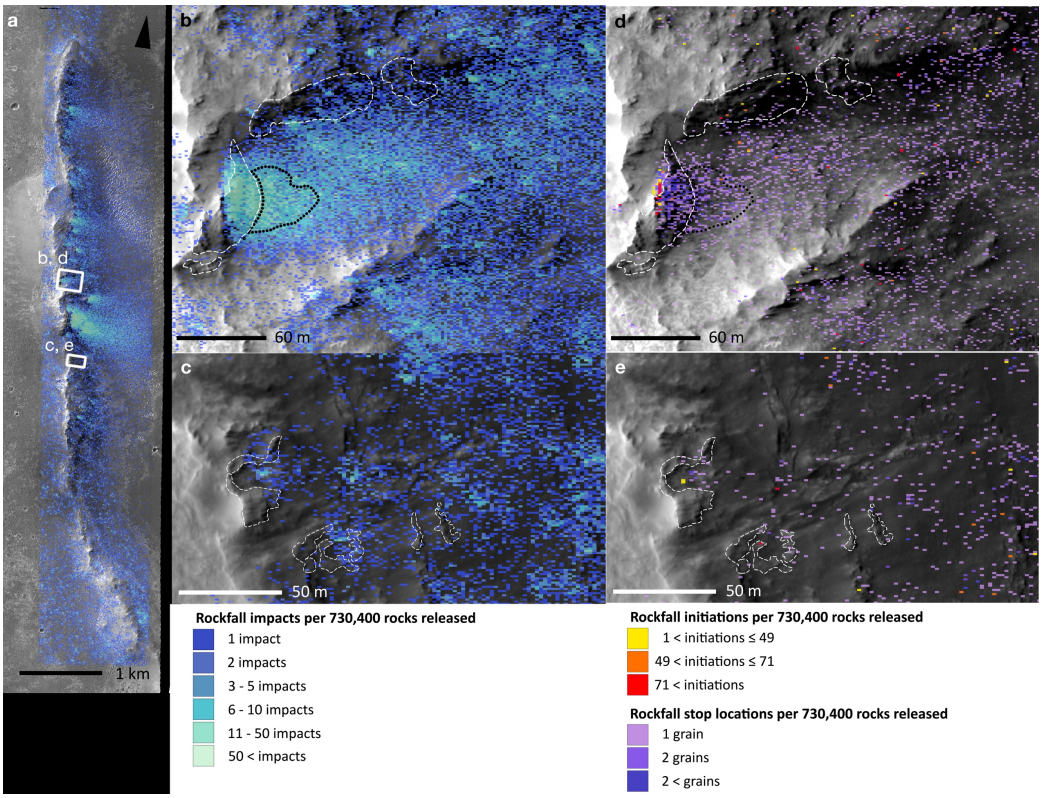

Figure 10: Heatmaps of 730,400 simulations of the Beer et al. (2024) model on the Endeavour crater western rim. **a**: map of predicted impacts (cobble bounces) per cell over the entire rim; **b** and **c** show Marathon Valley and Perseverance Valley, respectively. White dashed lines outline rocky, steep regions, and black dotted line shows location of boulder field near head of Marathon Valley. The same locations are shown in **d** and **e** for number of rockfall events initiated per cell and the number of grains that came to rest in each cell.

C h a p t e r 3

3D ARCHITECTURE OF KODIAK BUTTE AS EVIDENCE OF FLUVIAL OR SHOAL-WATER ENVIRONMENTS IN JEZERO CRATER, MARS

O. A. Kanine[1], M. P. Lamb[1], B. L. Ehlmann[1], J. P. Grotzinger[1], C. D. Tate[2]

[1]Division of Geological and Planetary Sciences, California Institute of Technology, Pasadena, CA

[2]Department of Astronomy, Cornell University

Corresponding author: Oak Kanine (oak.kanine@gmail.com)

In revision, JGR: Planets

Key Points:

- Kodiak butte in Jezero Crater preserves evidence of fluvial or shoal-water environments in a closed basin.
- Complex stratal geometries may be explained by deposition as a series of downstream-migrating river braid bars or deltaic mouth bars.
- Channelized flow at Kodiak is estimated to have been ~4.2 m deep with flow directions to the south-southwest.

Abstract

The Mars 2020 mission has explored depositional environments recorded in a fan-shaped deposit on the western side of Jezero crater. Kodiak butte is an isolated outcrop of sedimentary rock ~ 1 km south of the scarp at the edge of this main fan and may be an erosional remnant of that fan. Sedimentary strata of Kodiak butte were first interpreted to represent Gilbert delta foresets and a lake depth of at least 10 m. Subsequent closer-range images of the northern face of Kodiak have resolved additional details of stratal geometries, permitting alternative interpretations of depositional environments. Rover visible-wavelength images, a three-dimensional digital outcrop model, and principal component analysis-based plane-fitting allow detailed facies mapping and measurements of stratal geometries in Kodiak. We observed three sets of steeply inclined beds ~3 m, ~7 m, and ~10 m thick with local accretion directions ranging from ~NW clockwise to ~SW (covering ~230˚ azimuth). These sets are interpreted as deposits from downstream migrating fluvial bars with lobate geometries, consistent with mid-channel bars in a braided river or mouth bars on a delta top. Thus, rather than reflecting lake depth, the relief of the inclined beds reflect river depth (~4.2 $\frac{+4.2}{-2.1}$ m) and indicate a moderately sized gravel-bedded river flowing ~south-southwest.

Plain Language Summary

The Perseverance rover has explored Jezero Crater, hypothesized to be a once-habitable environment, to examine the geologic history of Mars and seek clues to

help evaluate if life developed on Mars. Understanding the significance of rock samples cached by the rover requires understanding the geological context in which they were found. We used rover-based images and a 3-D model of rock strata exposed in a butte named Kodiak to understand the ancient depositional environment that created the deposit. Within the sedimentary rocks, we found evidence for migrating, lobate river bars formed in a braided river or river delta, where the river channel was about 4 m deep and flowed south-southwest.

1 Introduction

Building on the legacy of the Curiosity rover, which identified ancient habitable fluvio-lacustrine environments on Mars (Grotzinger et al, 2014, 2015), the Mars 2020 mission seeks to understand Martian geologic history; identify ancient habitable environments; and explore, sample, and cache for return to Earth scientifically-compelling rock samples, including those with potential to preserve organic compounds (Beaty et al., 2019; Farley et al., 2020; Stack et al., 2020). Characterizing both paleo-habitability and potential to preserve biosignatures is therefore essential in establishing the value, context, and significance of a given sample.

The landing site for the Mars 2020 rover, 45 km-wide Jezero Crater, may have hosted a range of fluvial to lacustrine environments (e.g., Fassett and Head, 2005; Ehlmann et al., 2008; Schon et al., 2012; Goudge et al., 2017). Two fan-shaped sedimentary deposits are observed within the crater: the most well-preserved deposit—referred to henceforth as the Western fan—is located at the

terminus of Neretva Vallis, a sinuous valley thought to have hosted a braided river (Mangold et al., 2020) where it breaches the western side of the crater rim (Figure 1a). The second fan is a more eroded deposit called the Northern fan at the mouth of Sava Vallis (Jodhpurkar et al., 2024). The presence of an outlet valley, Pliva Vallis, incising the eastern side of the crater rim at -2395 m elevation might indicate the presence of an open-basin (i.e., overflowing) lake sometime in the crater's history (Fassett and Head, 2005). The western and northern fans have been interpreted to be river deltas, a conclusion supported by the existence of the inlet and outlet valleys and the presence of minerals indicative of aqueous activity, such as phyllosilicates and carbonates (Ehlmann et al., 2008; Goudge et al., 2015; Horgan et al., 2020). Schon et al. (2012) stipulate that the strata exposed in the fans (at least those visible from orbit) were likely deposited subaerially as part of the delta plain or delta top, with the modern morphology strongly controlled by differential erosion.

River deltas are of particular scientific interest for Mars Sample Return due to the high biosignature preservation potential of fine-grained bottomsets in analogous terrestrial deposits. Lakes are likely to concentrate both detrital and in-situ organics, especially in association with clay minerals capable of adsorbing organic molecules, and to preserve those organics through rapid sedimentation rates and protection from oxidation (e.g., Ehlmann et al., 2008; Summons et al., 2011). Fluvial and fan deposits may have lower preservation potential (*sensu* Summons et al. 2011). Therefore, it is important to establish the occurrences of deltaic and fluvial environments preserved in Jezero strata (e.g. Mangold et al., 2021, Stack et

al., 2024) to provide context for interpreting the collected samples and assessing Mars habitability over time. Here we contribute to this goal through detailed sedimentological analysis of Kodiak butte, an isolated outcrop of sedimentary rock that is likely an erosional remnant of the western fan.

2 Geologic Context

2.1 Orbital mapping and interpretations of environment

The Western fan has been divided into four units by orbital expression (Stack et al., 2020) (Figure 1a). The two uppermost units have been interpreted using orbital data as fluvial deposits in a delta topset environment (e.g., Fassett and Head 2005; Ehlmann et al. 2008; Schon et al., 2012; Goudge et al., 2018). The lower of these two expresses light-toned arcuate lineaments that are continuous for hundreds of meters (referred to in Stack et al. (2020) as "delta truncated curvilinear layered unit") (Figure 1e); the upper is a rough-textured, boulder-shedding unit that is organized in raised, low-sinuosity ridges up to ~300 m wide ("delta blocky unit" in Stack et al. (2020)) (Figure 1c and 1d). The curvilinear unit has been interpreted as scroll bars or point bar lateral accretion sets from meandering rivers (Schon et al., 2012; Ehlmann et al., 2008; Goudge et al., 2018) and the blocky unit was suggested to be gravelly channel bodies (Fassett and Head, 2005; Schon et al., 2012; Goudge et al., 2018). Strata exposed at elevations below the blocky and curvilinear units in the erosional scarp of the fan ("delta thickly layered unit" and "delta thinly layered unit" in Stack et al. (2020)) (Figure 1a) were initially

interpreted as a continuation of the delta plain environment (Schon et al., 2012), but later proposed to be delta front foresets transitioning into bottomsets (Goudge et al., 2017). East and south of the Western fan are several buttes and hills thought to be erosional remnants of a formerly more extensive deposit (e.g., Ehlmann et al., 2008; Schon et al., 2012, Goudge et al., 2015). The hypothesis that the crater floor once had more significant cover that has since undergone significant erosion is supported by observations of variations in crater density throughout the currently exposed crater floor (Shahrzad et al., 2019; Quantin-Nataf et al., 2023).

2.2 Rover (in-situ) mapping and interpretations of environment

After landing in 2021, the Perseverance rover explored first the crater floor units, largely agreed to be igneous in origin (e.g. Farley et al., 2022; Sun et al., 2023; Liu et al., 2023). The rover then approached and began to ascend the western fan scarp. The lower ~25 m of the fan deposit was named the "Shenandoah" formation (Stack et al., 2024), which corresponds broadly to the "delta thinly layered unit" and the lowest occurrence of "delta truncated curvilinear unit" (Figure 1) encountered along the rover's traverse (Stack et al., 2020). Stack et al. (2024) interpreted the sandstone to conglomerate lithologies at the base of the formation as a distal alluvial plain. The overlying thin interval of finer-grained (mudstone and fine sandstone) rocks were interpreted as delta bottomsets or lakebed sediments; the authors also considered an alluvial floodplain setting, though assess that scenario to be less likely (Stack et al., 2024). At the top of the formation, lenses or lobate bodies of cross-stratified and sub-horizontal medium sandstones to granule

conglomerates which scour the underlying deposits were interpreted as sediment gravity flows at the toe of a delta front, though the authors also consider mid-channel bars (at a delta mouth or in a braided river channel) or a distal, unconfined alluvial fan to be plausible depositional settings (Stack et al., 2024).

Also exposed on the fan scarp are several packages of steeply-inclined strata. Some of these strata are arranged in antiformal (domed or concave-down) structures 80-100 m wide and ~20-25 m thick (Gupta et al., 2022; Gupta et al., 2023; Mangold et al., 2024); others form cliffs wherein the bed orientation appears consistent (e.g., Franklin Cliffs, Gupta et al., 2023). Some of these packages are locally conglomeratic (Gupta et al., 2023, Gupta et al., 2024) while others are primarily sand (Mangold et al., 2024). One of the antiformal bodies directly overlies the Shenandoah formation (called Whale Mountain, Gupta et al., 2023); others are located further north on the scarp (Mangold et al., 2024) and the contact with underlying strata was not studied at close range. The inclined beds were interpreted as Gilbert delta foresets (Mangold et al., 2021; Gupta et al., 2022; Gupta et al., 2023; Mangold et al., 2024) and the antiformal packages as delta lobes (Gupta et al., 2022; Gupta et al., 2023), or delta lobes and mouth bars (Mangold et al., 2024).

Atop the western fan within the curvilinear unit are steeply-dipping beds similar to those found in the fan scarp (Gupta et al., 2024; Caravaca et al., 2024a). One such outcrop, Pinestand Mountain, was suggested to be antiformal in cross-section (Caravaca et al., 2024a). Here, inclined beds were again interpreted as Gilbert delta foresets, and the antiformal structure as a delta lobe or mouth bar (Gupta et al., 2024; Caravaca et al., 2024a). Lower-lying packages of medium sandstone

alternating with coarse sandstone to conglomerate lithologies form the inclined, curvilinear strata in the Tenby formation (Ives et al, 2023) interpreted as foresets in delta lobes (Ives et al., 2023; Caravaca et al., 2024a), mouth bars (Ives et al., 2023; Caravaca et al., 2024a; Gupta et al., 2024), or downstream-migrating fluvial bars (Ives et al., 2023; Gupta et al., 2024).

Bedded pebble-to-boulder conglomerates sit over the packages of steeply-inclined strata, both on the fan scarp (Mangold et al., 2021; Mangold et al., 2024) and atop the fan (Caravaca et al., 2024a; Gupta et al., 2024). These may have formed as braided river deposits in delta topsets (Mangold et al., 2021; Caravaca et al., 2024a; Mangold et al., 2024). Structureless boulder deposits, in contrast, have been proposed to represent a later stage highly-energetic flood, possibly unrelated to the deposition of the Western fan (Mangold et al., 2021; Catuneanu et al., 2023; Gupta et al., 2024; Mangold et al., 2024). These deposits might signify a transition to a debris-flow dominated alluvial fan environment (Catuneanu et al., 2023), expressed from orbit as the delta blocky unit (Mangold et al., 2024).

2.3 First observations of Kodiak butte and depositional hypotheses

Kodiak butte is a flat-topped hill ~1 km south of the nearest frontal scarp of the Western fan, measuring ~250 m across its longest axis (northeast to southwest) and rising ~80 m above the surrounding terrain. Kodiak is interpreted as an erosional remnant of the once more extensive fan (Goudge et al., 2015, Mangold et al., 2021). The modern topography of Kodiak butte, which provides outcrop exposure on multiple faces, provides an opportunity to study stratal architecture in

three dimensions. Specifically, the butte exposes the depositional sequences in two roughly orthogonal cross-sections that are otherwise visible only in planview on the fan top.

The eastern face of Kodiak butte (Figure 2a) was imaged at ~2.4 km distance on sol 63 by mast-based rover instruments (Bell et al. 2021, Maurice et al., 2021), revealing two multi-meter-scale packages of southward-dipping steeply-inclined beds containing coarse grains (Mangold et al., 2021). These packages are bracketed by low-angle strata above and below. Higher in the stratigraphy are instances of local cross-stratification, and at the top of the butte lies a boulder conglomerate that was mapped from orbit as continuous with the delta blocky unit atop the main fan (Stack et al., 2020). Images of the northeast corner (Figure 2b) and northern face of Kodiak (Figure 2c) acquired later in the mission revealed: 1) an additional sequence containing beds nearly orthogonal to those in previously observed sequences (Kanine et al., 2023), and 2) that the steeply-inclined beds are structured in antiforms (Kanine et al., 2024; Caravaca et al., 2024b).

Depositional hypotheses for the strata contained within Kodiak have evolved since the receipt of initial images as more data have been acquired. Mangold et al. (2021) interpreted the packages of inclined strata exposed on Kodiak's east face as two southward-progradational sequences of a Gilbert-type delta, with the steep strata representing delta foresets and the underlying and overlying strata representing delta bottomsets and topsets, respectively. Catuneanu et al. (2023) considered each sequence a distinct delta lobe. Mangold et al. (2021) inferred that foresets and topsets to be cobbly sandstones and the bottomsets to be

mudstones or sandstones, while Catuneanu et al. (2023) suggested that the steeply inclined beds may be coarse sandstones to fine conglomerates (clasts up to ~ 2 cm) based on the angle of repose. Mangold et al. (2021) proposed that the Kodiak strata were deposited after the breach of the Jezero crater rim and the deposition of most of the Western fan and therefore are evidence of a falling lake level. Mangold et al. (2021) and Catuneanu et al. (2023) also both interpreted the strata as recording fluctuations in lake level, with each set of inclined beds on the east face deposited into a falling or stable lake, the deposition of the two sets separated by a lake level rise of ~10 m, and each set truncated by a lake level fall of unknown amount. Caravaca et al. explained the variation in bed orientations between the two sequences visible on the north face (approximate center, Figure 2c and described in Section 2.3) as varying progradation directions of Gilbert delta mouth bars in a shallow lake, with progradation first to the northeast, then to the southwest, and finally south-southeast (Caravaca et al., 2024a, 2024b). Migration and accretion of large bars as a mechanism for generating the stratal architecture at Kodiak was first introduced by Kanine et al. (2023) and extended in Kanine et al. (2024), wherein it was suggested that the antiformal structures and three sequences of inclined beds could result from the downstream-accretion of either mid-channel bars in braided river channels or mouth bars under net flow roughly to the south.

We evaluated three hypotheses (Figure 3) for the origin of Kodiak butte, focusing on mechanisms for generating the large-scale steeply-inclined beds: 1) the inclined strata are Gilbert delta foresets on a subaqueous delta slope; 2) the strata are mouthbars in a shoal-water delta, and 3) the strata are migrating fluvial mid-

channel bars. The locations and relationships of these depositional environments (hypotheses 1-3) are illustrated in a terrestrial example in Figure 4 and an idealized schematic in Figure 5. While we acknowledge other settings and processes can produce lobate landforms or steeply-inclined beds (such as beach spits, Nielsen et al.,1988; Hiroki and Masuda, 2006; Mäkinen and Räsänen, 2003; Spaggiari and Bordy, 2023), we focus on the ones in our current understanding to be most relevant to a Martian setting in general (e.g., inferred to lack significant tides) and most consistent with depositional processes inferred to have taken place elsewhere on the Jezero fan.

In brief, delta foresets, or delta front clinoforms, are subaqueous basinward-inclined sedimentary deposits (Steel and Olsen, 2002; Patruno and Helland-Hansen, 2018) emplaced across delta lobes (Figure 4a, Figure 5a) (Vakerelov and Ainsworth, 2013; Ainsworth et al., 2016; van Yperen et al., 2020). The delta lobe assemblage stratigraphy is bounded by changes in depositional process or major shoreline shifts (e.g., Vakerelov and Ainsworth, 2013), and the duration of activity at a given lobe is determined by the timescale of avulsion of the trunk channel (e.g., Longhitano, 2008; Caldwell and Edmonds, 2014). Gilbert-type deltas are a specific type of river deltas characterized by a tripartite architecture (Gilbert, 1885) of topsets, foresets, and bottomsets. Spanning the subaqueous delta slope (Figure 4b, Figure 5d), the height of Gilbert delta foresets (from topset to bottomset) are understood to record a lower bound on lake depth (e.g., Postma, 1990; Postma, 1995; Mortimer et al., 2005; Patruno et al., 2015). Mouth bars are deposited due to the decrease in sediment transport capacity that occurs from expansion and

deceleration of flow at the river mouth (e.g., Edmonds and Slingerland, 2007; Rowland et al., 2009; Fagherazzi et al., 2015). Mouth bar growth advances the delta basinward by building out the delta top or plain; these bars therefore prograde near the transition from delta top to delta front, or from proximal to distal portions of a subaqueous fan (Gruszka and Zielinski, 2021). In comparison, we use the term "mid-channel bar" or "braid bar" to define a non-bank-attached, freely migrating bar within a river channel.

We used a 3D model and rover images (described in *Section 3*) taken from multiple perspectives to conduct a detailed analysis of Kodiak's facies and architecture (observations presented in *Section 4*). In *Section 5* we discuss the environmental characteristics associated with each depositional hypothesis as supported by terrestrial analogs and evaluate the plausibility of each hypothesis. We then estimate the paleohydraulic conditions associated with the deposition of Kodiak butte in *Section 6*. Finally, the implications for scientific understanding Jezero crater's history of aqueous activity, the Western fan, and the Perseverance rover sample cache are explored in *Section 7*.

3 Methods

Orbital-based geologic context was established using a ~25 cm/pixel mosaic of HiRISE (High Resolution Imaging Science Experiment) images and mosaicked digital elevation models, derived from HiRISE stereopair images (Fergason et al., 2020), with ~ 1m/pixel resolution and sub-meter elevation precision. Observations of units, facies, and stratigraphy of Kodiak butte relied upon rover-based images

from Mastcam-Z and SuperCam; these images were used to construct a 3-D model upon which we performed fine-scale geometric analyses.

Mast Camera Zoom (Mastcam-Z) (Bell et al., 2021) is a pair of multispectral cameras located on the rover mast, 1.985 m above the ground (Bell et al., 2021). Mastcam-Z images shown in this study (Figure 2) are lossless products, rendered in enhanced color for the purpose of exaggerating color differences to better see details. The color was enhanced by scaling the data in each RGB color channel to the minimum and maximum radiance-calibrated (RAD) values, then using ± 3 standard deviations from the median value to produce the final image. At 110 mm focal length (maximum zoom), the field of view is 6.2° × 4.2° and the instantaneous field of view (IFOV) is 67.4 μrad/pixel (Bell et al., 2021). At 478 m (distance from rover to north-facing side of the butte for sol 416 images), the pixel size is 3.3 cm/pixel, while at 2.4 km (distance from rover to the east-facing side of the butte for the sol 63 images) the pixel size is ~17 cm/pixel. For example, if we require a bed to be 3-5 pixels thick to be confidently traceable, we can resolve beds ~10-17 cm thick using the sol 416 Mastcam-Z mosaic. Further details on image resolutions may be found in Table S1.

SuperCam remote micro-imager (RMI) (Maurice et al., 2012; Maurice et al., 2021) images have a much smaller field of view than Mastcam-Z (20 μrad/pixel IFOV) but higher resolution (pixel sizes of 2.47 cm at ~2.4 km distance for sol 63 and 0.73 cm at ~0.7 km distance on sol 580). SuperCam coverage of the butte is incomplete but was used to complement Mastcam-Z images for analysis where

available. RGB values and brightness for SuperCam images were manually stretched to balance contrast, lighting, and feature visibility unless otherwise noted.

A digital outcrop model (DOM) (Figure 3) was created as a Structure-from-Motion (SfM) product in which long-baseline Mastcam-Z and SuperCam RMI images spaced throughout the rover's traverse were used to photogrammetrically solve the outcrop's structure using Agisoft (methods in Tate et al. (2024). The model textural overlay, composed of Mastcam-Z images draped over the 3-D mesh, was oversampled for a smoother appearance. Error in the mesh is greatest in the look direction, aligned roughly radially outward from the butte to the rover. We used pixel scale (Table S1) to represent the minimum range error; however, the error could be at least 2-3 times the pixel scale in some areas (Tate et al., 2024). The DOM was aligned to JPL's rover Octavia E. Butler landing site frame.

The software Planetary Robotics 3D Viewer (PRo3D) (Barnes et al., 2018) was used to view the model, trace beds where they may be locally approximated as planar, and to extract these traces. We performed in-application plane-fitting on the bedding traces using a sampling covariance-based principal component analysis (PCA) regression, which fit a plane through the two orthogonal directions of most variance in the x-y-z coordinates of the traces and returned a best-fit solution for plane orientation along with a fit error in both the strike and dip (Quinn and Ehlmann, 2019). Bed orientations were visualized in dip angle-dip azimuth space (plots in Figures S1-S5).

Units were defined primarily as depositional sequences (pulses of sedimentation) and their associated lithofacies contained within stratigraphic

bounding surfaces. Mastcam-Z mosaics were used to describe outcrop character at the scale of decimeters to meters, including bedding geometries, significant structures within units, unit thicknesses, and behavior at unit contacts. SuperCam images were used where available to study bedding fabric, low-order surfaces, and grain size at sub-meter to centimeter scale. Grain sizes were classified using the modified Udden-Wentworth scale (Blair and McPherson, 1999) in which gravels (containing subclasses granule, pebble, cobble, and boulder) are defined as grains 2 - 4096 mm, and sand grains as 0.063 - 2 mm.

4 Observations

4.1 Unit definitions

The east face of Kodiak butte exposes ~220 m of strata laterally and nearly 40 m vertically, and the northern face exposes strata spanning nearly 150 m laterally and 34 m vertically. We divide these strata into 6 units (Figure 6) and describe their expression (from stratigraphically lowest to highest) as viewed on the eastern face, the northern face, and the northeast corner of the butte where the two faces join.

4.1.1 Unit 1

Located at the base of the outcrop, Unit 1 contains wedge-like low-angle crossbedding with planar beds typically ~10-30 cm thick (Figure 7, Figure 8). We do not resolve cobbles or boulders in SuperCam images; the grains that can be identified are not larger than ~5 cm (a coarse pebble) and are typically 2-4 cm,

around the limit of feature detection with available images (Table S1). The majority of the sediment is therefore inferred to be grains <~2 cm in diameter. Unit 1 is thickest on the northeast point of the butte, where it spans ~7 m in height before being covered by talus at its base. Unit 1 is only visible on northern portion of the eastern face and occurs on average at a lower elevation on the eastern face than the northern (Figure 2, Figure 6). On the northern face, the boundary between Unit 1 and Unit 2 is mostly obscured by talus. Some Unit 3 beds appear to pass conformably into Unit 1 on the northern face; in this location we distinguish Unit 1 beds as lacking genetically related steeply-inclined portions, in contrast to the overlying Unit 3 beds which steepen upwards tangentially, or as lacking abundant coarse grains.

4.1.2 Unit 2

Unit 2 is a sequence of steeply-inclined, parallel planar beds typically a few centimeters thick. These beds are arranged in an antiform near the center of the unit. The well-defined portion of the structure is ~6 m wide and ~1.3 m tall, containing concentric convex-up beds (Figure 8), with one side dipping northeast (54˚ mean azimuth, groups R and S in Figures S1, S2) at a 27˚ angle on average, the other dipping northwest (318˚ mean azimuth, group T in Figures S1, S2) at 33˚ on average, and a rollover in the middle. Isolated rounded cobbles are present, most frequently found in lenses in the downslope portion of beds or concentrated in coarse-grained beds. Unit 2 is on average ~ 2 m thick and ~ 3 m thick at maximum. It is exposed for ~60 m horizontally on the northern face of Kodiak (Figure 6c); the

corresponding elevation on the eastern face is covered in talus. Beds that do not roll over in the center of the antiform are planar and truncated at their tops by overlying low-angle to subhorizontal strata at the base of Unit 4. Unit 2 appears to locally scour Unit 1 (Figure 8), but this determination is uncertain due to limited exposure of the Unit 2-1 contact and resolution constraints.

4.1.3 Unit 3

Unit 3 also contains convex-up or antiformal bedding geometries: beds dip west on the northern face and south on the eastern face with a rollover visible at the northeast corner of Kodiak (Figure 6b). This structure is characterized by steeply inclined beds that are centimeters to decimeters (~50 cm maximum) thick. On average, beds on the eastern face dip at a 29˚ angle at 186˚ azimuth (south) (east half of group A and groups B-G, Figure S1 and S3) and those on the north face of Kodiak dip 27˚ at 253˚ azimuth (west-southwest) (north half of group A and groups N-Q, Figures S1, S2).

From north to south along the eastern face, the inclined beds transition from sharp to tangential bases. Some poorly-expressed beds appear to be complete sigmoids, while others further south terminate abruptly at an overlying broad erosional surface (the lower bound of Unit 4) (Figure 7c). Pebbles, cobbles and a few boulders are present in this unit (Figure 7c; Figures S6-S9, Table S2), concentrated in coarse lenses (Figures S7 and S8) or within beds showing weak downslope coarsening (Figure 7c). The largest grains (coarse cobbles to fine

boulders) are predominantly rounded to subrounded; angularity of the smaller grains cannot be confidently determined.

From east to west along the north face (Figure 8c) Unit 3 exhibits a similar transition from sharp-based, planar beds to sigmoidal beds—some complete, with vertical heights typically ~4 m and sometimes reaching nearly 5 m in height (Figure S10, Table S3)—to beds with tangential bases truncated at their tops by overlying subhorizontal beds. Coarser lenses or beds of subrounded gravels are present, though no consistent grading can be determined from available images. On both the east and north faces there are abundant reactivation surfaces creating a mature stratigraphic hierarchy in Unit 3.

Unit 3 is 4.5 m thick near the northeast corner and increases in thickness along the eastern face, forming a possible scour surface that descends ~3 m in elevation and truncates Unit 1 beds (Figure 7c, 7d), until it reaches just over 10 m in thickness at ~35 m from the northeast corner. The base of the unit is obscured by regolith (Figures 2a, 6a). On the northern face the Unit 3 sequence extends for ~80 m horizontally before contacting Unit 2 (Figure 2c, Figure 6c). Notably, Unit 2 and Unit 3 occur at the same elevation range and have the same position relative to Unit 1 and Unit 4 but have nearly opposite bedding dip directions at their contact (Figure 8d, 8f; Figure 9). Unit 3 reaches nearly 7 m in thickness on the north face, though it thins to ~2 m near the contact with Unit 2 (Figure 6c). The precise nature of the boundary between the two units is difficult to determine, but appears non-erosional: some Unit 3 beds form troughs (Figure 8f) up to 2 m wide and 20-30 cm deep that onlap (terminate up-dip against) the underlying Unit 2 beds, while other

Unit 3 beds may downlap (terminate in the down-dip direction) with a sharper base at the contact, though this determination is hindered somewhat by image quality. There is a higher proportion of coarse grains in Unit 3 near this contact. The uppermost boundary of Unit 3 is the base of the overlying truncating packages of subhorizontal Unit 4 beds.

4.1.4 Unit 4

Unit 4 lies above both Unit 2 and Unit 3 and contains a variety of facies. On the northern half of the eastern face (right in Figure 2a and 6a) Unit 4 is expressed as subhorizontal stratification, while near the center of the eastern face, Unit 4 develops a small-scale package of inclined beds (marked with "#" in Figure 6a). We infer this package is continuous with the larger-scale inclined beds on the southern half of the eastern face (left in Figure 2a and 6a; Figure 7b). Steeply-dipping (average 31˚, Groups H, J, and part of group K, Figure S4) and gravel-bearing beds that coarsen upslope constitute the upper ~7 m, at maximum, of this sequence. These beds are ~10-40 cm thick and contain well-rounded cobbles and boulders up to 36 cm in width. The beds are sharply truncated by Unit 5 at their tops and shallow in dip angle at their base, appearing to pass conformably into the underlying ~11 m of more gently-inclined beds. Together the steep and shallow beds, which we interpret as a single, genetically-related depositional sequence, have a mean azimuth of 146˚ (southeast) (Groups H - M, Figures S1, S4).

We interpret the Unit 3-4 boundary on the east face to descend across the butte from north to south in a similar, if more pronounced, fashion as the Unit 1-3

boundary, such that Unit 4 reaches at least 18 m in thickness. Unit 4 beds truncate the inclined beds of Unit 3 in places (Figure 7c). However, regolith cover in the center of the eastern face makes this portion of the boundary uncertain in terms of location and contact behavior.

On the northern face, the same stratigraphic position is occupied by a succession of cross stratification with planar set boundaries and isolated gravel-sized clasts as large as boulders (Figure 8b). Bedsets are frequently ~1 m thick but range from 0.7 to ~2 m in thickness. Individual crossbeds are parallel planar and centimeters to ~ one decimeter in thickness (Figure 8b) with have variable dip directions; i.e., a given set might contain crossbeds with apparent dips to the east while another set has crossbeds with apparent dips to the west. At the base of this succession, the crossbedding transitions into subhorizontal bedding, as on the east face, with instances of very low-angle cross stratification. We interpret these facies on the north face as a continuation of Unit 4, though we cannot rule out the possibility of an unseen truncation surface in the middle of the butte between the northern and eastern faces.

Unit 4 reaches 14 m thick on the north face, with the base of the unit occurring at a higher elevation on the northern face than the eastern face (Figure 6b). As on the east face, the subhorizontal Unit 4 beds seen on the north face in places truncate inclined beds of the underlying Unit 2 (Figure 8e) and Unit 3 (Figure 8c). Part of Unit 4 extends to the top of the modern topography of Kodiak; part is scoured by Unit 5 (Figure 7b).

4.1.5 Unit 5

Unit 5 is expressed as planar crossbedding on the east face (Figure 6a, 7a). Bedsets here are typically 1-2 m thick, with most crossbeds a few centimeters to ~20 cm thick and with apparent dips to the north. Isolated rounded cobbles are present, with no obvious grading of these visible grains. Unit 5 reaches ~10 m thick on the east face. It truncates the inclined beds of Unit 4 at its base (Figure 7b) and itself is scoured at its top by Unit 6.

The exposure on the north face (Figure 6c) reveals multiple concave-up (scoop-shaped) scours with coarser grains (cobbles or fine-to-medium boulders) concentrated at their bases (Figure 8a). These scours frequently truncate subhorizontal beds. We infer this succession of trough-crossbedding is laterally continuous with the (apparently) planar crossbedding seen on the east face, with the variation in geometry produced by differences in cross-sectional view, though again it is possible that a truncation surface occurs between the exposures. We define the boundary between Unit 5 and Unit 4 as the lowest occurrence of trough cross-stratification; this boundary itself constitutes a larger concave-up trough 16 m wide and ~3 m deep.

4.1.6 Unit 6

Kodiak is capped by a ~4 m thick boulder-bearing deposit which we designate Unit 6. The unit is massive and lacks evidence for grading, preferred clast orientation, or other clast-based fabrics. Unit 6 is visible on both the eastern

and northern faces and scours into the underlying crossbedding of Unit 5 (Figures 6, 7, 8) with an irregular contact.

4.2 Outcrop geometry

We fit planes to 289 beds in the steeply-inclined sequences across the outcrop (Figures S2-S4; Data Set S1, *ds01.xlsx*.). These orientations, presented in planview in Figure 9c, are placed into 21 groups and spatially averaged to better visualize geometric patterns across the butte. Overall, the bed orientations agree with initial measurements reported by Tate et al. (2023).

Beds in Unit 3 fan outward in dip azimuth from an axis through the Unit 3 antiform aligned north-south or northeast-southwest such that beds to the east of this centerline axis dip on average to the south while those to the west of the axis dip on average southwest (Figure 6, Figure 9c; Figure S5). The width of Unit 3 normal to this axis is ~70 m; as the east face appears to cut near the center of the antiform, we infer the pre-erosional width of this antiform is ~140 m.

Unit 2, like Unit 3, has bidirectional dips associated with an antiform, with beds on one side dipping on average northeast and beds on the other side dipping on average northwest, making a center axis oriented north-south or northeast-southwest plausible. Where Unit 3 contacts Unit 2, the beds of the two sequences are nearly orthogonal (Kanine et al., 2023). The portion of Unit 2 with bidirectional dips associated with the antiform and the beds with consistent orientation on its eastern flank is ~34 m wide.

Finally, the inclined beds of Unit 4 on the east face dip on average southeast. If these beds are associated with an antiform, the form's center would be within the butte and not visible.

5 Evaluating depositional models

Any depositional model of the ancient environment that Kodiak represents must explain the following key observations (*points 1-8*):

1. **Sequence geometry**: Stratal geometries seen in outcrop define lobate forms. There are two concave-down ("domed") structures or antiforms in Units 2 and 3 wherein beds roll over from one side to the other (Figure 6b, Figure 8e) with bidirectional local dip azimuths (Figures S2, S3, S5). The dip azimuths in Units 3 and 4 are also not in a consistent direction, but rather fan out from ~south to ~west and within the southeast quadrant, respectively. This range of dip directions is consistent with arcuate surfaces with center axes aligned ~north-northeast—south-southwest (Figure 9a, 9b) (through the center of the antiforms). Sequences in Units 2 and 3 are at the same stratigraphic level and have nearly opposed dip azimuths at their contact: here, Unit 2 beds dip ~northeast (Group R) while Unit 3 beds dip ~southwest (Group Q) (Figures 6c, 8d, 8f, 9c; Figure S2).

2. **Scale**: These lobate antiforms have relief to first order >2 m (thickness of Unit 2) and possibly up to ~18 m (thickness of Unit 4) and widths < 200 m (see *Section 4.2*).
3. **Stacking pattern**: The center axes of the lobate forms in Units 2, 3 and (presumably) 4 are offset laterally, i.e. east-west, from each other, as well as vertically, with Units 2 and 3 aligned at roughly the same elevation and Unit 4 overriding Units 2 and 3. Thus the lobate forms are shingled with deposits filling in the topographic lows similar to stratigraphic compensational stacking (e.g., Straub et al., 2009).
4. **Grain size and fabric**: Gravel-sized grains (pebbles, cobbles, and boulders) are observed in Units 2, 3, 4, 5, and 6 (Figures 7 and 8). Both normal (fining up-dip, Figure 7c) and inverse (coarsening upwards, Figure 7b) grading is observed in the sequences of steeply-inclined beds in Units 3 and 4, respectively.
5. **Dip angle**: The large-scale inclined strata associated with the antiforms are steep, dipping 29˚ on average for all traces of steeply-inclined beds (29˚ as the average for Unit 2, 29˚ as the average of Unit 3 east face traces, 27˚ for Unit 3 north face traces, and 31˚ for the Unit 4) with 21˚ as the maximum recorded well-constrained (<10˚ maximum angular error) dip angle for Unit 2 beds, 43˚ for Unit 3, and 37˚ for Unit 4. These angles are consistent with the angle of repose for cohesionless sediment (coarse or angular sand, sandy gravel, or gravel) (e.g., Kleinhans et al., 2011b; Glover, 1997; Mellmann, 2001).

6. **Tripartite geometry**: the steeply-inclined beds of Units 2-4 occur between packages of low-angle or subhorizontal beds.
7. **Contact relationships** at unit boundaries vary significantly. The bases of Units 3 (Figure 7d), 4 (Figure 7c), 5 (Figure 7b), and possibly 2 (Figure 8e) are at least locally erosional, truncating underlying strata and creating up to several meters of erosional relief (Figure 6a, 6c, 7c, 8a) and scour surfaces that extend up to tens of meters laterally. The Unit 4-5 boundary is concave-up, containing trough crossbedding that scours underlying planar crossbedding in Unit 4. In other cases, the unit contacts are non-erosional: for example, Unit 3 is locally conformably with Unit 4 on the north face where the rollover at the top of inclined beds is preserved to create a sigmoid (Figure 8c), and with Unit 1 where tangential Unit 3 beds do not scour the underlying deposit.
8. **Associated facies**: low-angle to subhorizontal beds as are found overlying the steeply-inclined sets (Figures 7b, 7c, 8c, 8f), low-to-moderate-angle planar cross-stratification (Units 1 and 4, Figures 7d, 8b), and trough cross-stratification (Unit 5, Figure 8a).

In summary, the convex-up geometries and radial spread of dip azimuths of the inclined beds are consistent with deposition by lobate or linguoid landforms with arcuate fronts prograding in a persistent direction approximately south-southwest. Progradation of a lobate form in a consistent direction can explain dip directions that vary locally and systematically due to the 3-D arcuate front of the

landform producing local accretion directions that fan out from the net transport direction. This process is recorded in local bedding dip directions that are roughly orthogonal to the front of the advancing landform. The east face exposes a section near parallel to the net transport direction along the center axes of Unit 3 landform whereas the north face exposes a plane that transects the landforms roughly perpendicular to the net transport direction and reveals the center and flanks of the Unit 2 form and one flank of the Unit 3 form (Figure 9). The convex-up shape of the Unit 3 lobate landform is preserved at the northeast corner of Kodiak (Figure 6b), such that looking ~south-southwest at the northeast corner of Kodiak provides a view approximately down the form's center axis.

We now use these observations to assess the depositional hypotheses. We focus on the inclined beds and lobate forms, and do not assess further Unit 6, the capping boulder deposit, as it has been inferred in previous work (Mangold et al., 2021, Catuneanu et al., 2023) to represent a shift to a higher energy paleoenvironment.

5.1 Mid-channel bars

We first evaluate *hypothesis 3* (Figure 3), which is our preferred interpretation. Mid-channel bars can occur in a braided river, an alluvial or fluvial fan, or delta top. Rivers can produce convex-up strata in the form of mid-channel bars viewed in flow-perpendicular cross-section (Figure 5b) (Zhang et al., 2021; Miall, 2006; Lunt et al., 2004; Ramanthan et al., 2010; Ashmore, 1991). As river bars prograde downstream, local accretion directions are roughly orthogonal to the

front of the advancing landform and thus fan out to high angles from the net transport direction (as described in Miall, 1977; Miall, 2006, "downstream-accretion macroforms"). Fluvial bars are typically 1-10 m in height and 10s to 100s of meters in width (Miall, 2006; Lunt et al., 2004; Li et al., 2023) and can be overlapping or shingled in the stratigraphic record (e.g., Miall, 1977; Miall, 2006). Rivers are capable of transporting gravel-sized grains as bedload which constructs angle of repose slip faces on the fronts of downstream-migrating linguoid or lobate bars (Miall, 1977; Bridge, 1993; Herbert et al., 2019). Such bar deposits may have a tripartite structure of angle-of-repose strata between low-angle 'topsets' and 'bottomsets' (Herbert et al., 2019). These slip-face or lee-side strata can be angular or tangential at their bases (Figure 5c) (Miall, 1977; Herbert et al., 2019) and demonstrate variable grading or sediment sorting (e.g., Herbert et al., 2019; topsets described in Gobo et al., 2015; Miall, 2006). Asymptotic shallowing of dip angle at bar tops (i.e., preserved rollover in sigmoidal beds) is predicted by vertical aggradation of an antiformal structure and has been observed on Earth (e.g., Mohrig et al., 2000; Chamberlin and Hajek, 2019). Rivers also host a variety of scour surfaces that can be laterally extensive: within the channels themselves, erosional surfaces, frequently scoop or spoon shaped, can be found upstream of bars or at confluences (Bridge, 1993; 'hollows' in Miall, 2006; Best, 1988; Best and Ashworth, 1997; Ashmore and Parker, 1983; Ashmore, 2022), and outside of the channel, the bases of overbank deposits may also be erosive (Slingerland and Smith, 2004; Hajek and Edmonds, 2014). Rivers can produce a great diversity of facies, including low-angle bedload gravel or sand sheets (Woolridge and Hicken,

2005; Miall, 2006), subhorizontal finer-grained floodplain deposits, and cross-stratification (planar or trough) from migrating bedforms (e.g., Bridge 1993; Miall, 2006; Ashmore, 2022).

Figure 9a shows a simple interpretive model of three shingled mid-channel braid bars with morphologies following those described on Earth (Ashmore, 1991; Bridge, 1993; Li et al., 2023) that have been eroded post-deposition into the topography of Kodiak butte (Figure 9b). The geometric model shows—even while neglecting confounding factors such as varying flow direction, bilateral asymmetry and irregularities in bar front shape, combined lateral and downstream migration, bar rotation, and preservation of bar backs—remarkable similarity to bed orientation measurements from the Kodiak DOM (Figure 9c). We note that in this schematic we are not attempting to reconstruct the exact depositional past of Kodiak, but rather to illustrate that even a very simplified scenario of predominantly downstream-accreting lobate bars migrating south-southwest can plausibly explain the majority of our observations. Bedding geometries at the real-life, more extreme limits of this depositional system could explain what anomalies remain between the modeled bed orientations and those observed such as the beds in the Unit 2 bar dipping northwest.

We conclude that narrow, arcuate fronts of lobate or linguoid barforms within a river channel prograding in a persistent direction — approximately south-southwest — under a spatially and stratigraphically consistent (i.e., broadly unidirectional and temporally constant) current can explain observations without the need to rely on significant changes in transport direction or lake level rise over

short temporal and spatial scales, as has been invoked for *hypothesis 1* (delta front) (Mangold et al., 2021; Caravaca et al., 2024a, 2024b).

5.1.1 Possible terrestrial analogs

If the Kodiak deposit is primarily sand with only isolated gravel lenses, analogous examples of multi-meter foresets of downstream-migrating unit bars are relatively common in ancient Earth systems (Almeida et al., 2015 and sources within) (Table S6). In the case that the majority of sediment in Kodiak is gravel, terrestrial analogs of large, coarse bars are less abundant (Bluck 1971; Smith 1989), but examples do exist in modern deposits and in Earth's geologically recent sedimentary record.

In the Sagavanirktok River, Alaska, ground-penetrating radar has revealed steeply-inclined (up to angle of repose) gravel unit bar avalanche faces with heights up to 2 meters, interbedded with sand or sandy gravel strata (Lunt et al. 2004). These unit bars can reach 400 m long (Lunt et al., 2004).

The Triassic Sherwood Sandstone Group 'Bunter' Pebble Beds in England contain cross-stratified pebble conglomerate sequences typically 2-5 m thick and continuous for more than 100 m in the direction of transport (Steel and Thompson, 1983). Steel and Thompson (1983) interpret the deposits as downstream-accreting mid-channel bars in a confined braided river with depth greater than that of a proglacial outwash plain or alluvial fan, but less than that of a catastrophic outburst flood (Steel and Thompson, 1983). At fine (< 1 m) scale the bar foresets exhibit alternating clast-supported pebble conglomerate strata and bimodal, medium-to-

coarse sandstone matrix-supported pebble/cobble conglomerate strata (Steel and Thompson, 1983). The authors attribute the bimodality of the matrix-supported conglomerate to the sourcing of sand from underlying strata by way of erosion and entrainment and subsequent transport as sediment-gravity flows, while the grading is attributed to sorting which deposits the coarsest fraction at the base of the slope during the avalanching process (Allen, 1965) or decreases in discharge (Smith, 1974). The variation in textural maturity and matrix abundance in the cross-strata are argued as indicative of regular (non-ephemeral) but variable discharge (Steel and Thompson, 1983). Horizontal strata frequently capping the inclined beds are explained by Steel and Thompson (1983) as the bar supraplatform (Bluck, 1971; Bluck, 1976), exposed during low flow.

Large-scale gravel bars are also found in the Miocene Arikaree Group in Nebraska, U.S. Korus et al. (2020) analyzed this outcrop using a DOM produced from drone imagery, a dataset comparable to the one utilized in this study. They observe crossbedding in a boulder conglomerate with a sand-to-pebble matrix, with bedsets typically ~10 m thick (vertically) but as much as 24 m thick (Korus et al., 2020). Korus et al. (2020) observe multiple stories, or generations, of channel fill in this system, and broad scours at the base of the inclined strata units. They conclude that the cross strata formed by accretion on bar margins via avalanching and propose the notable thickness of the bar deposit was due to an increase in discharge in a trunk channel within a narrow or confined valley (Korus et al., 2020).

Terrestrial outburst flood deposits may serve as additional potential analogs for Kodiak's strata. Outburst floods typically are associated with the

catastrophic failure of pro-glacial lake ice dams or sudden ice melt driven by climate change or volcanic eruptions (e.g., Bretz et al., 1956; Teller, 2004; Montgomery et al., 2004). Similar processes may have occurred on Mars, but in addition, Mars outburst floods may also have been driven by other, non-climate-related mechanisms such as deep groundwater discharge (Baker et al., 2009; Coleman and Baker, 2009; Burr et al., 2009). Floods of this extreme magnitude can deposit large bars, whose preservation is enhanced by large sediment grain sizes (e.g., Fahnestock and Bradley, 1973; Marren, 2005). For example, the Pleistocene Bonneville flood, resulting from the overtopping of glacial Lake Bonneville, deposited downstream-accreting bars with ~6 m relief of exposed bar front strata (O'Connor, 1993). These beds are 0.25 - 1.5 m thick and dip 15 - 34˚ with azimuths typically within ~30˚ of the local flow direction, though some are perpendicular to the flow (O'Connor, 1993). Additionally, the repeated catastrophic failures of ice dams during the Quaternary initiated outpourings of glacial lake water across the globe: in the Altai Mountains of Siberia, megafloods produced gravel bar deposits 300 m thick (Baker et al., 1993; Herget 2005; Carling et al., 2009), composed mostly of planar gravel sheets but also including sequences of inclined beds reaching several meters in height (Carling, 2013); in the Channeled Scablands of the U.S., the glacial lake Missoula floods (e.g., Pardee, 1942; Bretz, 1956) deposited gravel bars with downstream-dipping strata ~18 m high (Baker 1973).

Given terrestrial instances of ~2 m to ~18 m (maximum) thick sets of gravel-bearing inclined beds, deposition in outburst floods is a plausible scenario for Kodiak strata. However, it is also possible to deposit and preserve meters-scale

coarse bar front strata (e.g., Steel and Thompson, 1983; Korus et al., 2020) during more typical (annual or decadal) or non-catastrophic riverine floods.

6.1.2 Interpretation of Kodiak strata in the context of the mid-channel bar hypothesis

Under the mid-channel bar hypothesis, the steeply-inclined beds in Units 2, 3, and 4 are interpreted as downstream-migrating bar front strata, with the antiforms in Units 2 and 3 as bar centers (and the center of the Unit 4 bar not visible) (Figure 9c). We agree with the assessment of Mangold et al. (2021, 2024) and Caravaca et al. (2024b) that the Kodiak antiforms are not bank-attached bars, such as alternate bars or point bars, as such bars do not produce a full linguoidal bar form of the type that is observed in Unit 3 at the northeast corner and in Unit 2 on the northern face with complete rollover and convex-up bedding geometries. Here we discuss how other observations from Kodiak butte might fit into the migrating bar hypothesis.

The cross-stratification seen on the north face exposure of Unit 4 may be smaller-scale bedforms such as straight-crested dunes migrating up the Unit 4 bar stoss and/or upstream of the Unit 4 bar. Similarly, the trough cross-stratification of Unit 5 may represent sinuous-crested dunes migrating within a scour, either representing a channel or a scour hole following another bar that was not preserved in the butte. However, as these Unit 4 and 5 cross strata are truncated by overlying beds, we can only observe a lower bound on the original bedform height, and it is possible at least some of these cross strata were more bars.

The subhorizontal beds above and sometimes truncating Units 2, 3, and 4 may be genetically-related to the inclined sets as in-channel bar top deposits such as plane bed bedload sheets transported by flow over the top of the bar (e.g., Bridge, 1993; Miall, 2006) or the bases of migrating bedforms (e.g., Herbert et al., 2019). Alternatively, they may be finer-grained falling-stage, slackwater, or overbank deposits. The low-angle beds directly underlying the steeply-inclined packages may similarly be older plane bed or overbank deposits (in the case of Unit 1) or, in the case of Unit 4, where steeply-inclined beds seem to pass non-erosionally and conformably into gently-inclined beds, genetically-related "bottomsets" (Herbert et al., 2019) formed by deposition and sediment reworking downstream of the lee face. Alternatively, these low-angle beds may be a continuation of Unit 3, as the Unit 3-4 boundary across the east face of the butte is obstructed by regolith.

Bars with angle-of-repose avalanche faces that form at confluences (e.g., Best, 1988), termed tributary mouth bars, can resemble deltas (Miall, 1977; Bridge, 1993). The spoon or trough shapes formed by confluence scours (Ashmore, 2022) are consistent with the descending base of Unit 3 as seen on the east face and the concave-up base of Unit 5 as seen on the north face. As at confluences, the scour pools trailing bars (e.g., diagram in Ashmore 2009) allow for the formation of separation eddies (Miall 2006, sources within) and angle of repose avalanche faces may then fill the scour topography. We interpret the truncated inclined beds of Unit 3 (on the east face) deposited atop a scour surface with ~3 m of relief from north to south (Figure 7c and d) as recording a local flow depth of at least ~10.6 m in a scour

hole upstream of a bar or possibly at a confluence (Smith, 1990; Mohrig et al., 2000) (Figure S10, Table S4).

6.2 Mouth bars

Mouth bars (*hypothesis 2* in Figure 3), as in the case of river bars, may have "mounded," "bell-shaped," "bidirectional," or concave-down/convex-up forms with beds that can range in dip azimuth over tens of degrees (Leszczyński and Nemec, 2015) and heights typically a few meters and widths tens to hundreds of meters or even over a kilometer (Schomacker et al., 2010; Cole et al., 2021; Gobo et al., 2015; Leszczyński and Nemec, 2015; van Yperen et al., 2020) that shingle or stack compensationally (Gobo et al., 2015; Leszczyński and Nemec, 2015; van Yperen et al, 2020; Cole et al., 2021). Like river bars, mouth bars may be composed of a range of grain sizes, including gravels (Leszczyński and Nemec, 2015; Winsemann et al., 2021; Gobo et al., 2015) with varied grading (Cole et al., 2021). Steep beds (Gobo et al., 2015; Cole et al., 2021) up to angle-of-repose if dominated by grain avalanches (Winsemann et al., 2021; Gobo et al., 2015) at mouth bar fronts can occur within a tripartite internal architecture (Winsemann et al., 2021). These inclined beds can be sigmoidal, tangential, or planar (Schomacker et al., 2010; Leszczyński and Nemec, 2015; Winsemann et al., 2021; Cole et al., 2021). The bases of mouth bars can be variably erosive or depositional (Schomacker et al., 2010; Winsemann et al., 2021; Cole et al., 2021) such that mouth bars can both generate and infill spoon/trough-shaped scours with several meters of erosional relief (Winsemann et al., 2021; Cole et al., 2021; Schomacker et al., 2010).

Associated facies include subhorizontal stratification (found at bar tops and underlying bar bottomsets) and planar and trough cross-stratification (e.g., Winsemann et al., 2021; Cole et al., 2021). We consider mouth bars a plausible explanation for the Kodiak strata.

Well-developed and prominent terrestrial mouth bars similar to strata found at Kodiak (Table S7) are described as occurring in the "proximal mouth-bar zone" on subaqueous fans (Gruszka and Zielenski, 2021), shoal-water deltas or mouth-bar type deltas (Lesczcyński and Nemec, 2015), shoal-water mouthbar deltas (Winsemann et al., 2018), shallow-water deltas (Cole et al., 2021; Winsemann et al., 2021), or simply in a shallow lake (Schomacker et al., 2010). Such deltas may be generalized as "topset-dominated," a stratigraphic category that occurs over a large range of basin and inlet parameters but is particularly predominant in shallow basins with gentle slopes (Edmonds et al., 2011) or low accommodation space (Gruszka and Zielinski, 2021). These mouth bar systems were formed by friction-dominated (Lesczcyński and Nemec, 2015; Winsemann et al., 2021) and inertia-dominated (Winsemann et al., 2021) jets where freshwater bedload-dominated feeder systems (Winsemann et al., 2021) – such as gravel-bed rivers (Lesczcyński and Nemec, 2015), braided rivers (Winsemann et al., 2021), glacial crevasses or subglacial tunnels/meltwater streams (Gruszka and Zielinski, 2021), or glacial outwash braidplains (Winsemann et al., 2021) – drain into proglacial lakes (Winsemann et al., 2021; Gruszka and Zielinski, 2021), intermontane lakes (Schomacker et al., 2010), shallow marine rift basins (Cole et al., 2021), or incised paleovalleys (Lesczcyński and Nemec, 2015). These mouth bar-dominated or

subaqueous fan systems tend to be more ephemeral and fed by highly-channelized systems (Gruszka and Zielinski, 2021; Budai et al., 2021). Currents can persist over such systems where the basin is shallow compared to inlet flow depths (Gruszka and Zielinski, 2021), meaning even finer-grained "prodelta" or distal subaqueous fan deposits basinward or underlying mouth bar deposits may experience active tractional sediment transport instead of, or in addition to, quiescent deposition of fine-grained sediment via settling from suspension.

Under the mouth bar hypothesis, the sets of steeply-inclined beds in Units 2, 3, and 4 are interpreted as the fronts of a lobate mouth bar. The subhorizontal beds overlying these sets may be either low flow or slackwater deposits deposited via settling from suspension atop the Unit 2, 3, and 4 bars, or bedload sheets or plane bed strata formed via bedload traction transport (e.g., Winsemann et al., 2021). These subhorizontal beds then transition upwards into smaller-scale bedforms, i.e. dunes (cross-bedding in Units 4 and 5) and, in the case of Unit 4, evolve laterally into the inclined beds of a younger mouth bar front deposited at higher baselevel. These Unit 4 dunes therefore may be climbing the back and top of the Unit 4 mouth bar, while the trough cross-bedding of Unit 5 may have been deposited within the trough-shaped scour in the zone of flow expansion just upstream of another mouth bar (as in figure 10 in Gruszka and Zielinski, 2021) formed after another lake level rise, whose front has since eroded away. Alternatively, in the case of a falling lake level, Unit 5 may represent in-channel fluvial bedforms. Finally, the subhorizontal to low-angle crossbedded strata of Unit 1 at the base of the Kodiak succession may be the distal portion of a very shallow-

water subaqueous fan (Gruszka and Zielinski, 2021), or more proximal deposits of saltated bedload or settled suspended load (e.g., Winsemann et al., 2021; Cole et al., 2021) contemporaneous with Units 2 and 3.

5.3 Interpretation of Kodiak strata in the context of Gilbert delta foreset hypothesis

Gilbert deltas (*hypothesis 1* in Figure 3) have been discussed in other work that interpret the Kodiak strata (Mangold et al., 2021; Catuneanu et al., 2023; Caravaca et al., 2024). Delta lobes can take convex-up forms (e.g., Gani and Bhattacharya, 2005; Graham et al., 2015) and their fronts form on a vast range of scales, with thicknesses of terrestrial examples ranging from meters to hundreds of meters (e.g., Budai et al., 2018). Delta lobes can stack to fill available accommodation space (Feng et al., 2019; Graham et al., 2015). The gravels observed in Kodiak could be transported at Gilbert delta fronts (recent descriptions found in e.g., Gobo et al., 2015; Rubi et al., 2015; Budai et al., 2018), with various mechanisms producing both normal (Kleinhans, 2005; Kostic, 2019; Gruszka and Tomasz, 2021) and inverse (Budai et al., 2021; Gobo et al., 2015) grading in angle-of-repose foreset beds (Patruno and Helland-Hansen, 2018; Gilbert, 1885). The archetypical internal geometry of a Gilbert-type delta is tripartite (Gilbert, 1885). Gilbert deltas can generate spoon/scoop-shaped scours at their toes, consistent with the morphology of the Unit 1-3 contact (Bornhold and Prior, 1990; Leszczyński and Nemec, 2015 and sources within). Their foresets may be truncated at their tops or preserve rollovers in sigmoidal bedding geometries (e.g., Patruno and Helland-

Hansen, 2018; Budai et al., 2021). Delta topsets may contain a diversity of fluvial deposits, which may generate subhorizontal planar bedding and cross-stratification.

The aspect ratio (height vs. width) and degree of curvature of the forms at Kodiak, as well as their overall scale (i.e., 10^0 - 10^1 m in height, 10^1 - 10^2 m in width), are inconsistent with delta lobes that would be commensurate with the size of the Western fan deposit, which has a radius of curvature ~4.5 km measured to the modern main fan boundary scarp or ~8.9 km if encompassing the most distal fan remnants (Goudge et al., 2018). Even if the Western fan system had multiple elongate lobes, a morphology typical of fine-grained and low-gradient systems (an assumption not supported by grain size observations at Kodiak), such systems tend to be composed of only 4 to 6 main lobes (Chadwick et al., 2022); meaning the lobate forms observed at Kodiak are too small in scale to be delta lobes associated with a system several kilometers wide like the Western fan. High-order stratigraphic surfaces on delta lobes the size expected for a deposit the size of the Western fan (hundreds of meters to over a kilometer in width), when viewed at outcrop scale (tens to a few hundred meters), would trace only very subtle concave-down geometries in shoreline-parallel cross-section (e.g., Figure 3 in Feng et al., 2019; Figure 8 in Graham et al., 2015, note vertical exaggeration; Bhattacharya, 2006). Stratigraphic surfaces traceable to a particular lobe, therefore, would record consistent orientations at outcrop scale, unlike the significant variation in bed orientation observed at Kodiak over <100 m for a single antiform.

It also would be unusual that protruding lobes would form in a delta composed of the grain sizes occurring in Kodiak and in a martian setting. Gravel

deltas tend to have lower cohesion than their muddy counterparts, which limits both levee and channel bank formation and longevity (Edmonds and Slingerland, 2010; Caldwell and Edmonds, 2014). Such deltas thus tend to be dominated by lateral channel mobility, frequent avulsions, and, for systems with friction-dominated effluents as in shallow basins, channel bifurcations (Edmonds and Slingerland, 2010; Caldwell and Edmonds, 2014). These processes tend to distribute sediment evenly along the delta front, which is why gravel-bedded deltas and fan deltas on Earth tend to have broad arcuate forms that make the semicircular planform or "delta" shape (Table S8), rather than protruding lobes (e.g., like the Mississippi delta).

Mangold et al. (2021) define Gilbert deltas as those created by inertia-dominated jets, which are homopycnal and associated with basins that are deep relative to the inlet flow (Wright et al., 1977); this is in agreement with the definition of Zavala et al. (2024) of Gilbert deltas as homopycnal littoral deltas. For evenly distributed sediments, as is typical of the coarse-grained deltas of which Gilbert deltas are a subcategory, the stable configuration of the shoreline or topset-foreset transition is a straight (shoreline-parallel) line or a radially-symmetric front (Ke and Capart, 2015). Modern or recent examples of (predominantly) homopycnal Gilbert deltas include the deltas in Lake General Carrera, Chile (Bell, 2009); the Peyto Lake Delta (Smith and Jol, 1997; Lai et al., 2019); and the Wushe Resevoir delta (Ke and Capart, 2015), which all show remarkably smooth fronts in planview (Table S8). Caravaca et al. (2024b) uses a more expansive definition of "Gilbert delta," positing that the steeply-inclined beds at Kodiak were deposited by hypo-

or hyperpycnal flows, both of which generally create more gently-sloping fronts and more extensive prodelta deposits than prototypical Gilbert deltas (e.g., Zavala et al., 2024 and sources within; Lai et al., 2019). Hyperpycnal flows in particular can readily occur in lacustrine settings (Winsemann et al., 2021; Zavala et al., 2024). Examples of coarse hyperpycnal deltas include the Noeick River delta (Bornhold and Prior, 1990) and the Lillooet Lake delta (Best et al., 2005), which, while somewhat more rugose than the aforementioned homopycnal Gilbert deltas, nevertheless also lack protruding, approximately parallel, narrow (finger-like) lobes in planview.

Forced regressions associated with the catastrophic draining of ice-dammed pro-glacial lakes, during which baselevels drop tens of meters in a couple of weeks (Winsemann et al., 2018; Kostic et al., 2019), may produce narrow, digitate or linguoid lobes for coarse-grained deltas on Earth. While these lobes are a similar scale as Kodiak (5-30 m thick foresets arranged in mounds 15-360 m wide, Kostic et al., 2019), at time of writing there is no evidence for a similar rapid drop in baselevel within Jezero crater below the elevation of the outlet channel.

We find it implausible that a coarse-grained delta several kilometers wide would produce narrow lobes with convex-up strata observable over tens of meters. More specifically, terrestrial examples of Gilbert deltas appear incompatible with an interpretation of the Kodiak antiforms as delta lobes or the inclined beds as lobe-scale delta fronts.

6 Paleohydraulic analysis

To better understand the river flows responsible for forming the barforms in Kodiak, we focus on Unit 3 and use paleo-hydraulic methods that rely on measurements of grainsize and barform relief (e.g., Hayden et al., 2020; Paola and Mohrig, 1996).

Grain size counts on the eastern face of Kodiak were performed across an area of 215 m^2 (Figure S6) that sampled representative Unit 3 strata along the beds used for paleochannel depth estimates (Figure S10). We used a ~0.11-m spaced grid overlaid on SuperCam images (Supplement Text S2; Figures S7, S8) to choose measurement locations, analogous to a Wolman pebble count (Wolman, 1954). We counted 82 grains (Dataset S2, ds02.xlsx) that could be resolved with available images (Table S1), all but 1 with diameters between 7.4 cm and 29 cm. We assume a log-normal distribution typical of fluvial bed sediment (Paola and Mohrig, 1996; Parker, 2004) to estimate the median grain size (D_{50}) between 1.1 cm and 3.6 cm from the visible coarse tail (Equation S1), similar to the grain size inference of Catuneanu et al., 2023. We utilize the value of D_{50} derived from the most heavily-sampled bin, 2.6 cm, in estimates of paleo-discharge.

Barform relief, as recorded by crossbed height, is an approximate proxy for bankfull flow depth (Miall, 2006; Smith, 1990; Mohrig et al., 2000). The height of the inclined beds at Kodiak, therefore, would record a deep river, with bed topography varying in both the streamwise (~north-south) and cross-stream (~east-west) directions. While truncated bar strata can underestimate flow depth due to

incomplete preservation (e.g., Paola and Borgman, 1991), complete sigmoidal bar strata – like those found in Unit 3 on the north face (Figure 8c) – are considered fully-preserved (Chamberlin and Hajek, 2019) and approximate the *local* depth of the morphology-controlling bankfull flow (Mohrig et al., 2000). Measurements of nine complete sigmoids in Unit 3 on the north face (Figure S10, Table S3) average 4.2 m in height.

However, local flow depths can vary significantly across space: Mohrig et al. (2000) report measurements of downstream-accreting bar heights in the modern North Loup River that range from 0.1 to 3 times the reach-averaged bankfull flow depth. The depth variation and large heights can record confluences, where field measurements of local braid channel depths are reported as being 3 or 4 (Fahnstock and Bradley, 1973), 5 (Best and Ashworth, 1997), or typically not greater than 6 (Ashmore and Parker, 1983) times deeper than mean confluent channel depth. Depth variation also results from scour holes upstream of large bars, where the local flow depth is less well-quantified but suggested to be three times deeper than mean channel depth (Cant 1976). We interpreted the Unit 3 truncated inclined beds on the east face 3 to record deposition into such a scour hole with a local flow depth of ~10.6 m (Figure 7). Using the relationships between local and reach-averaged bankfull flow depths identified by Cant (1976) and Mohrig et al. (2000), we estimate that the mean bankfull depth is ~3 times smaller than this measurement, or at least ~3.5 m. This is consistent with the average relief of the sigmoidal beds on the north face of 4.2 m in height. We use the 4.2 m value in subsequent paleohydrology calculations.

In a mouth-bar system, the descending base of Unit 3 may record a basinward scour (e.g., Winsemann et al., 2021; Cole et al., 2021; Schomacker et al., 2010) or may broadly reflect the local slope of the basin itself. Basin depths near mouth bars are often not much greater than distributary channel depths (Cole et al., 2021), or might even be shallower (Wright, 1977). Regardless, it is more likely that bar heights upstream of the scour approximate the distributary channel depth, and therefore we use a flow depth of 4.2 m for this hypothesis as well.

As the base of Unit 3 may reflect local channel bed topography and not be representative of reach-scale channel slope, we use empirical relationships to estimate the slope. Braided gravel-bed rivers typically have channel geometries such that during bankfull floods, the shear stress exceeds the threshold for mobility of the median sediment size by 40% (Paola and Mohrig, 1996). Using the constrained flow depth of 4.2 m and D_{50} = 2.6 cm, we set the bankfull Shields number to 40% larger than the critical value for motion (Paola and Mohrig, 1996) and assume a basaltic composition with a submerged specific density of 2.0. The result is a channel-bed slope estimated to be ~4 x 10^{-4} (Equation S2-S5). A relatively gentle slope such as this can produce braiding behavior at high discharges (Li et al., 2022) and terrestrial gravel-bedded braided rivers do exhibit similar slopes (Church and Rood, 1983). For comparison, the average slope in the lower section of Neretva Vallis is 0.01 (Mangold et al., 2020). It is typical for a fan, deposited in a region of increased accommodation space, to have a shallower slope downstream of its inlet bedrock canyon (e.g., Stock et al., 2008).

Using a flow resistance equation for gravel-bed rivers, we find a depth-averaged flow velocity of ~1 m/s (Ferguson, 2007) (Equation S6), which explicitly accounts for gravity. The product of flow depth and flow velocity yields the water discharge per unit channel width. While the architecture of Kodiak's strata places some constraints on the width of the individual bars (~140 m; **Section 5**), the number of channel braids or the total channel width are unknown. Braided rivers can have width-to-depth ratios that can range from 50 to over 400 (Gibling, 2006; Kleinhans et al., 2011a; Eaton et al., 2010; Li et al., 2023; Church and Rood, 1983; further discussion in Supplemental Text S3). We use width-to-depth ratios between 50 and 400, intended to capture a wide but realistic range of channel geometries. We thus estimate that the channel width could have been 210 – 1680 m, with the former representing a system just reaching the threshold of braiding and the latter a broad braid plain. With these inputs and assumptions, we found bankfull discharges that range from ~890 m^3/s – ~7,100 m^3/s (Figure S11, Table S5).

To see the sensitivity of our result to the assumed grainsize, we repeated the exercise using the same equations, but this time using an order of magnitude smaller particle size of D_{50} = 2 mm. For such a sandy braided system, Unit 3 strata could be deposited under a discharge of ~220 - ~1800 m^3/s (Figure S11, Table S5), but under very small bed slope ~ 1 x 10^{-5}, which is probably unlikely given the close proximity to the feeder canyon at Neretva Vallis.

In the case of mouth bars, we use the estimated pre-erosional width (~140 m) of the Unit 3 antiform as an upper bound for the distributary channel width,

yielding a width-to-depth ratio of 33. We find deposition of Unit 3 as a mouth bar would require a paleo-discharge of ~600 m^3/s for a gravelly deposit and ~150 m^3/s for a sandy one (Figure S11, Table S5).

In summary, we infer that for either mid-channel bars or mouth bars, the river recorded by Unit 3 strata was moderately deep (~4.2 m at bankfull) and relatively low gradient (4×10^{-4} or shallower). While some gravel-sized grains are observed directly, it is unclear if they constitute the majority of the deposit; however, a median grain size of pebbles may be derived from terrestrial grain size distributions and is consistent with the steepness of the beds. For comparison, the more conservative estimates (w:d = 50) for flows with gravel bedload are similar to spring and summer flows in the South Saskatchewan River (Pomeroy, 2005).

7 Implications for broader Jezero Basin environmental history

In summary, lobate forms may be generated in multiple settings, at multiple scales, and by different processes. We use our observations of Kodiak's facies and stratal geometry to evaluate three (frequently related) hypothetical depositional environments. While previous studies (Mangold et al., 2021; Catuneanu et al., 2023; Caravaca et al., 2024b) favored interpretation of Kodiak's sets of steeply-inclined strata as a Gilbert delta front deposit (foresets), analysis of both the north and east faces of the butte and comparison to terrestrial analogs suggests deposition as downstream-accreting lobate bars, either as mouth bars in a shallow lake or as

fluvial mid-channel bars, with a consistent net sediment transport and migration direction ~south-southwest.

While Gilbert deltas (*hypothesis 1*) are reliable recorders of lake level and shoreline trajectories (e.g., Patruno et al., 2015; Gobo et al., 2015; Patruno and Helland-Hansen, 2021), barform relief is controlled by channel geometry. The height of fluvial bars (*hypothesis 3*) reflects channel depth, with sigmoidal beds most reliably recording local bankfull depth (Mohrig et al., 2000). Mouth bar (*hypothesis 2*) morphology is strongly controlled by inlet channel hydrodynamics and sediment transport characteristics (Edmonds and Slingerland, 2007; Fagherazzi et al., 2015). Basin depths at these locales may be similar to or even more shallow than those within the channel (Wright, 1977; Cole et al., 2021). Importantly, interpretation of the Kodiak large-scale inclined sets as lobate bars (either braid bars or mouth bars) connects barform relief to channel depth, rather than serving as reliable indicators of lake level.

Deposition as fluvial downstream-accreting mid-channel bars (*hypothesis 3*), while not incompatible with a contemporaneous lake, also allows for a scenario wherein Kodiak was deposited as an alluvial or fluvial fan in the absence of a contemporaneous standing body of water. For mid-channel bars on a delta top, the shoreline would be located further basinward from Kodiak with a surface possibly below the lowest exposure of fluvial strata, ~ -2515 m for Unit 1; i.e., a closed-basin lake with a water surface lower than previously proposed lake levels (Mangold et al., 2021). Under the mid-channel bar hypothesis, the rocks with the best likelihood of preserving organic material (fine-grained, clay-mineral rich,

more quiescent sedimentation) at or above this stratigraphic level would be found in floodplains (e.g., Summons et al., 2011). Both mouth bar or mid-channel bar depositional scenarios imply an overall smaller volume of standing water than the Gilbert delta front hypothesis – with either a smaller, shallower, more ephemeral standing body of water, or no lake at all.

Our hypotheses for Kodiak's origin may reconcile seemingly disparate observations across the Western fan scarp and top by permitting continuity of depositional environment. Firstly, some of the steeply-inclined beds arranged in concave-down antiforms that have been described on the Western fan scarp and top (*Section 2.2*) bear significant similarity to the structures observed in Kodiak, possibly indicating a common depositional mechanism. Secondly, accretion packages produced from the arcuate fronts of downstream-migrating bars, when exposed in a roughly planview outcrop, could produce geometries consistent with some of the curvilinear packages on the Western fan top (Figure 1e) which were initially interpreted as point bar lateral accretion sets (e.g., Goudge et al., 2018). An alternative explanation for the origin of the curvilinear unit (Stack et al., 2020) is therefore that at least some of these sets are the product of eroded downstream-migrating bars, seen in different exposure geometry than those at Kodiak, rather than only laterally-accreting point bars. This interpretation is supported by the consistency of our calculated flow depths at Kodiak with those estimated from fluvial landforms and deposits elsewhere on the Jezero fan complex: Goudge et al. (2018) calculated a flow depth of ~6.7 m with standard deviation 2.3 m from fan

top curvilinear unit stratal geometries, and Mangold et al. (2021) estimated a flow depth of 3 - 10 m from what was interpreted as a channel-filling conglomerate lens on the western fan scarp. An extreme upper bound on flow depth is provided by the geometry of the inlet valley, Neretva Vallis, which exhibits signs of moderate braiding and mid-channel bars tens of meters wide and does not exceed 50 m in depth in its lowermost 70 km before breaching the Jezero crater rim (Mangold et al., 2020). Additionally, the boulder-bearing deposit ("delta blocky," Stack et al., 2020) with consistent expression between Kodiak and the main fan (Figure 1c, 1d), while possibly representing a different depositional event and flow regime, places a relative constraint on the timing of deposition of Kodiak and the curvilinear unit and permits for an interpretation of these deposits as time-equivalent. Altogether, our measurements and evaluation of terrestrial analogs suggest it is possible to interpret both Kodiak and the fan top as a delta plain (*hypothesis 3a*); to interpret the Shenandoah formation upwards to Kodiak and the fan top units as recording the evolution of an alluvial fan into a mouth bar-dominated shallow-water delta (*hypothesis 2*); or, as an endmember scenario, to interpret the Western fan units and Kodiak as an alluvial fan succession (*hypothesis 3b*).

8 Conclusions

Large-scale, steeply-dipping beds are not unique to delta fronts but rather can be produced in several different environments. Previous work (Mangold et al, 2021) hypothesized that steeply inclined beds in Kodiak were deposited subaqueously as delta front foresets. Alternatively, our stratigraphic mapping,

measurements of bed orientations, sedimentologic analysis, and review of terrestrial analogs indicate that deposition as downstream-accreting, lobate, mid-channel bars in a moderately deep braided river on a delta top or alluvial fan or as mouth bars in a shoal-water delta or subaqueous fan – under flow to the south-southwest – could account for the complexity and stratal geometries observed at Kodiak without invoking changing flow direction. From measurements of inclined bed heights and interval-based grain counts, we estimate river bankfull flow depths of ~4.2 m and discharges of $\sim 10^2$ – $\sim 10^4$ m^3/s transporting a bedload with D_{50} between 1.1 – 3.6 cm. Any co-eval lake would have occurred below ~ -2515 m, with a depth unconstrained by the thickness of the Kodiak strata.

The mid-channel bar or mouth bar deposits in Kodiak may be stratigraphically equivalent to geometrically similar deposits on the Western fan and therefore suggestive of a continuous environment. The upper fan front and fan top units, along with Kodiak, may represent a delta plain; it is also plausible that the succession from the Shenandoah formation upward into Kodiak or the Tenby formation records either pulses of alluvial fan deposition or the evolution of an alluvial fan into a shoal-water delta deposited into a current-dominated lake that is shallow compared to its inlet channel depths. We suggest that prodelta deposits, if they exist in Jezero crater, would be restricted to lower elevations in the fan deposit, or even beneath the crater floor units.

Acknowledgments

We thank the Mastcam-Z and SuperCam teams for the acquisition of data, the Mastcam-Z DTM Working Group for feedback on model creation, and the Mars 2020 Perseverance Rover Science Team and SedStrat Working Group for enlightening discussion and commentary. We thank the creators of PRo3D for the tools used in this study. We are grateful to Woodward Fischer for his role in hypothesis development. O.A.K. is partially supported by a NASA FINNEST award #80NSSC22K1373 to B.L.E and a NASA Co-Investigator award for Mastcam-Z to J.P.G. B.L.E. is supported by a NASA Co-Investigator award for Mastcam-Z to B.L.E.

Open Research

HiRISE data are available publicly through the NASA PDS node (https://ode.rsl.wustl.edu/mars/). The rover-based imagery may be found https://planetarydata.jpl.nasa.gov/img/data/mars2020/ and the 3D model is available for download at https://sketchfab.com/3d-models/m2020-zcam-kodiak-delta-remnant-sol-580-cb8a890bdf4d4f36aa6bc28f1293be96. Data table of individual plane fits may be found at the CaltechDATA site https://doi.org/XXXX *[doi assigned once published. For review, the data is available at https://caltech.box.com/s/wskuujpofs6q23esd66e0npk0dnz6l0v].*

References

Ainsworth, R.B., Vakarelov, B.K., MacEachern, J.A., Nanson, R.A., Lane, T.I., Rarity, F. et al. (2016). Process-driven architectural variability in mouth-bar deposits: A case study from a mixed-process mouth-bar complex, Drumheller, Alberta, Canada. *Journal of Sedimentary Research, 86*, 512–541. https://doi.org/10.2110/jsr.2016.23

Allen, J.R.L. (1965). A review of the origin and characteristics of recent alluvial sediments. *Sedimentology, 5,* 89-191. https://doi.org/10.1111/j.1365-3091.1965.tb01561.x

Almeida, R.P., Freitas, B.T., Turra, B.B., Figueiredo, F.T., Marconato, A. and Janikian, L. (2016). Reconstructing fluvial bar surfaces from compound cross-strata and the interpretation of bar accretion direction in large river deposits. *Sedimentology, 63*: 609-628. https://doi.org/10.1111/sed.12230

Ashmore, P., and Parker, G. (1983). Confluence scour in coarse braided streams. *Water Resources Research*, 19(2), 392–402, doi:10.1029/WR019i002p00392.

Ashmore, P.E. (1991). How do gravel bed rivers braid? *Canadian Journal of Earth Science 28*, 326–341, https://doi.org/10.1139/e91-030

Ashmore, P. E. (2009). Intensity and characteristic length of braided channel patterns. *Canadian Journal of Civil Engineering*, *36*(10): 1656-1666. https://doi.org/10.1139/L09-088

Ashmore, P. E. (2022). Braiding. In: Shroder, J.J.F. (Ed.), *Treatise on Geomorphology, vol.* 6. *Elsevier, Academic Press*, pp. 517–543. https://doi.org/10.1016/B978-0-12-409548-9.12086-X

Baker, V.R. (1973). Paleohydrology and sedimentology of Lake Missoula flooding in eastern Washington. *Special Paper Geological Society of America 144*, 73 pp. https://doi.org/10.1130/SPE144

Baker, V.R., Benito, G. & Rudoy, A.N. (1993). Paleo-hydrology of late Pleistocene superflooding: Altay Mountains, Siberia. *Science 259*, 348–350, https://doi.org/10.1126/science.259.5093.348

Baker, V. R. (2002). High-energy megafloods: Planetary settings and sedimentary dynamics. *Flood and Megaflood Deposits: Recent and Ancient Examples*, eds. I. P. Martini, V. R. Baker and G. Garzon. *International Association of Sedimentologists Special Publication, 32*, 3–15. https://doi.org/10.1002/9781444304299.ch1

Baker, V. R. (2009). Overview of megaflooding: Earth and Mars. In D. M. Burr, P. A. Carling, & V. R. Baker (Eds.), *Megaflooding on Earth and Mars* (pp. 1–12). *Cambridge: Cambridge University Press*. https://doi.org/10.1017/CBO9780511635632.001

Barnes, R. et al. (2018). Geological analysis of Martian rover-derived Digital Outcrop Models using the 3-D visualization tool, Planetary Robotics 3-D Viewer—Pro3D. *Earth and Space Science, 5*, 285– 307. https://doi.org/10.1002/2018EA000374

Beaty, D. M. et al. (2019). The potential science and engineering value of samples delivered to Earth by Mars sample return: International MSR Objectives and Samples Team (iMOST). *Meteoritics & Planetary Science*, https://doi.org/10.1111/maps.13242

Bell, C. M. (2009). Quaternary lacustrine braid deltas on Lake General Carrera in southern Chile. *Andean Geology, 36*(1), 51–65, http://dx.doi.org/10.4067/S0718-71062009000100005

Bell, J. F. et al. (2021). The Mars 2020 Perseverance rover Mast Camera Zoom (Mastcam-Z) multispectral, stereoscopic imaging investigation. *Space Science Reviews 217*(24). https://doi.org/10.1007/s11214-020-00755-x

Best, J.L. (1988). Sediment transport and bed morphology at river channel confluences. *Sedimentology*, 35: 481-498. https://doi.org/10.1111/j.1365-3091.1988.tb00999.x

Best, J., and Ashworth, P. (1997). Scour in large braided rivers and the recognition of sequence stratigraphic boundaries. *Nature 387*, 275–277. doi: 10.1038/387275a0

Best, J. L., R. A. Kostaschuk, J. Peakall, P. V. Villard, and M. Franklin (2005). Whole flow field dynamics and velocity pulsing within natural sediment-laden underflows. *Geology*, 33, 765–768, https://doi.org/10.1130/G21516.1

Bhattacharya, J.P., (2006). Deltas. In: Walker, R.G., Posamentier, H. (Eds.), *Facies Models Revisited. vol. 84. SEPM (Society for Sedimentary Geology) Special Publications*, pp. 237–292, https://doi.org/10.2110/pec.06.84.0237

Blair, T.C. & McPherson, J. (1999). Grain-size and textural classification of coarse sedimentary particles. *Journal of Sedimentary Research, 69,* 6-19. https://doi.org/10.2110/jsr.69.6

Blake, W., Jr. (1956). Landforms and topography of the Lake Melville area, Labrador, Newfoundland. *Canada Department of Mines and Technical Surveys Geographical Bulletin,* v. 9, p. 93–97. https://doi.org/10.4095/330685

Bluck, B. J. (1971). Sedimentation in the meandering River Endrick. *Scottish Journal of Geology,* 7, 93-138, https://doi.org/10.1144/sjg0702009

Bluck, B. J. (1976). Sedimentation in some Scottish Rivers of Low Sinuosity. *Earth and Environmental Science Transactions of The Royal Society of Edinburgh*, *69*(18), 425–456. Royal Society of Edinburgh Scotland Foundation, https://doi.org/10.1017/S0080456800015416

Bornhold, B.D. and Prior, D.B. (1990). Morphology and Sedimentary Processes on the Subaqueous Noeick River Delta, British Columbia, Canada. In Coarse-Grained Deltas (eds A. Colella and D.B. Prior). https://doi.org/10.1002/9781444303858.ch9

Bretz, J H., Smith, H. T. U., and Neff, G. E. (1956). Channeled Scabland of Washington: new data and interpretations. *Geological Society of America Bulletin*, *67*, 957–1049. https://doi.org/10.1130/0016-7606(1956)67[957:CSOWND]2.0.CO;2

Bridge, J.S. (1993). The interaction between channel geometry, water flow, sediment transport and deposition in braided rivers. *Geological Society of London, Special Publications, 75*, 13–71. https://doi.org/10.1144/GSL.SP.1993.075.01.02

Buffington, J.M., Woodsmith, R.D., Booth, D.B., Montgomery, D.R. (2003). Fluvial processes in Puget Sound river and the Pacific Northwest. In: Montgomery, D.R., Bolton, S., Booth, D.B., Wall, L. (Eds.), *Restoration of Puget Sound Rivers*. *University of Washington Press*, Seattle, WA, pp. 46–78.

Burr, D., Wilson, L., & Bargery, A. (2009). Floods from fossae: A review of Amazonian-aged extensional–tectonic megaflood channels on Mars. In D. Burr, P. Carling, & V. Baker (Eds.), *Megaflooding on Earth and Mars* (pp. 194-208). *Cambridge: Cambridge University Press*. https://doi.org/10.1017/CBO9780511635632.010

Caldwell, R. L., and Edmonds, D. A. (2014). A numerical modeling study of the effects of sediment properties on deltaic processes and morphology. *Journal of Geophysical Research: Earth Surface, 119*, https://doi.org/10.1002/2013JF002965

Cant, D.J. (1976). Braided stream sedimentation in the South Saskatchewan River. Unpublished PhD thesis, McMaster University, ON, Canada, 248 pp. http://hdl.handle.net/11375/13379

Caravaca, G., Dromart, G., Mangold, N., Gupta, S., Stack, K. M., Le Mouélic, et al. (2023). The deltaic depositional environments and stratigraphy of the Kodiak Butte (Jezero crater, Mars). In *Paper presented at the 54th Lunar and Planetary Science Conference, 2023*. Retrieved from https://www.hou.usra.edu/meetings/lpsc2023/pdf /1473.pdf

Caravaca, G. et al. (2024a). Surface expression and geometries of deltaic deposits of Jezero western fan top (Mars). In *Paper presented at the 55th Lunar and Planetary Sciences Conference*, *202*4. Retrieved from https://www.hou.usra.edu/meetings/lpsc2024/pdf/1246.pdf

Caravaca, G., Dromart, G., Mangold, N., Gupta, S., Tate, C., Randazzo, N., et al. (2024b). Depositional facies and sequence stratigraphy of the Kodiak butte, western delta of Jezero crater, Mars. *Journal of Geophysical Research: Planets, 129*, e2023JE008205. https://doi.org/10.1029/e2023JE008205

Carling, P., Martini, I., Herget, J., Borodavko, P., & Parnachov, S. (2009). Megaflood sedimentary valley fill: Altai Mountains, Siberia. *Megaflooding on Earth and Mars, Cambridge University Press,* 243-264. https://doi.org/10.1017/CBO9780511635632.013

Carling, P. (2013). Freshwater megaflood sedimentation: What can we learn about generic processes? *Earth-Science Reviews, 125*, 87-113. http://dx.doi.org/10.1016/j.earscirev.2013.06.002

Chadwick, A. J., Steele, S., Silvestre, J., & Lamb, M. P. (2022). More extensive land loss expected on coastal deltas due to rivers jumping course during sea-level rise. *Proceedings of the National Academy of Sciences of the United States of America*, 119(31), e2119333119. https://doi.org/10.1073/pnas.2119333119

Chamberlin, E. P. and Hajek, E. A. (2019). Using bar preservation to constrain reworking in channel-dominated fluvial stratigraphy. *Geology* 47 (6): 531–534. https://doi.org/10.1130/G46046.1

Church, M., and Jones, D. (1982). Channel bars in gravel-bed rivers. In: Hey, R.D., Bathurst, J.C., Thorne, C.R. (Eds.), *Gravel-Bed Rivers. Wiley, Chichester*, pp. 291–324.

Coachman, L.K. (1953). River flow and winter hydrographic structure of the Hamilton Inlet–Lake Melville Estuary of Labrador: Blue Dolphin Labrador Expedition–Winter Project 1953: Hanover, New Hampshire, Dartmouth College Museum, 19 p. http://www.dtic.mil/dtic/tr/fulltext /u2/021124.pdf

Cole, G., Jerrett, R. and Watkinson, M.P. (2021). A stratigraphic example of the architecture and evolution of shallow water mouth bars. *Sedimentology*, *68*: 1227-1254. https://doi.org/10.1111/sed.12825

Colella, A. and Prior, D. B. (Eds.). (1990). *Coarse-Grained Deltas, Special Publication of the International Association of Sedimentologists, vol. 10*, Blackwell, Oxford. https://doi.org/10.1002/9781444303858

Coleman, N., & Baker, V. (2009). Surface morphology and origin of outflow channels in the Valles Marineris region. In D. Burr, P. Carling, & V. Baker (Eds.), *Megaflooding on Earth and Mars* (pp. 172-193). *Cambridge: Cambridge University Press*. https://doi.org/10.1017/CBO9780511635632.009

Cowan, E. J. (1991). The large-scale architecture of the fluvial Westwater Canyon Member, Morrison Formation (Jurassic), San Juan Basin, New Mexico. In: Miall A. D., Tyler N. (Eds.). *The three-dimensional facies architecture of terrigenous clastic sediments, and its implications for hydrocarbon discovery and recovery*. https://doi.org/10.2110/csp.91.03.0080

Eaton, B.C., Miller, R.G., Davidson, S. (2010). Channel patterns: Braided, anabranching, and single-thread. *Geomorphology* 120, 353–364. https://doi.org/10.1016/j.geomorph.2010.04.010

Edmonds, D.A., Shaw, J.B., and Mohrig, D. (2011). Topset-dominated deltas: A new model for river delta stratigraphy. *Geology*, 39 (12): 1175–1178. https://doi.org/10.1130/G32358.1

Edmonds, D. A., and R. L. Slingerland (2007). Mechanics of river mouth bar formation: Implications for the morphodynamics of delta distributary networks. *Journal of Geophysical Research 112*, F02034. https://doi.org/10.1029/2006JF000574

Edmonds, D., and Slingerland, R. (2010). Significant effect of sediment cohesion on delta morphology. *Nature Geoscience 3*, 105–109. https://doi.org/10.1038/ngeo730

Ehlmann, B., Mustard, J., Fassett, C. et al. (2008). Clay minerals in delta deposits and organic preservation potential on Mars. *Nature Geoscience 1*, 355–358. https://doi.org/10.1038/ngeo207

Eilertsen, R.S., Corner, G.D., Aasheim, O., and Hansen, L. (2011). Facies characteristics and architecture related to palaeodepth of Holocene fjord-delta sediments. *Sedimentology 58*, 1784–1809. https://doi.org/10.1111/j.1365-3091.2011.01239.x

Fagherazzi, S., D. A. Edmonds, W. Nardin, N. Leonardi, A. Canestrelli, F. Falcini, D. J. Jerolmack, G. Mariotti, J. C. Rowland, and R. L. Slingerland (2015). Dynamics of river mouth deposits. *Reviews of Geophysics, 53*, 642–672, https://doi.org/10.1002/2014RG000451

Farley, K. A., Williford, K. H., Stack, K. M., Bhartia, R., Chen, A., de la Torre, M., . . . Wiens, R. C. (2020). Mars 2020 mission overview. *Space Science Reviews, 216*(8), 142, https://doi.org/10.1007/s11214-020-00762-y

Farley, K. A., Stack, K. M., Shuster, D. L., Horgan, B. H. N., Hurowitz, J. A., Tarnas, J. D., ... Zorzano, M. P. (2022). Aqueously altered igneous rocks sampled on the floor of Jezero crater, Mars. *Science*, *377*, 6614, https://doi.org/10.1126/science.abo2196

Fassett, C. I., and Head, J. W. (2005). Fluvial sedimentary deposits on Mars: Ancient deltas in a crater lake in the Nili Fossae region. *Geophysical Research Letters*, 32, L14201, https://doi.org/10.1029/2005GL023456

Fergason, R. L., Hare, T. M., Mayer, D. P., Galuszka, D. M., Redding, B. L., Smith, E. D., Shinaman, J. R., Cheng, Y., Otero, R. E., (2020). Mars 2020 Terrain Relative Navigation Flight Product Generation: Digital Terrain Model and Orthorectified Image Mosaics. 51st Lunar and Planetary Science Conference, Retrieved from: https://www.hou.usra.edu/meetings/lpsc2020/pdf/2020.pdf.

Ferguson, R. (2007). Flow resistance equations for gravel- and boulder-bed streams. *Water Resources Research*, 43, W05427, https://doi.org/10.1029/2006WR005422

Fahnestock, R. K. & Bradley, W. C. (1973). Knik and Matanuska Rivers, Alaska: a contrast in braiding. In: *Fluvial Geomorphology* (ed. by M. Morisawa), 220–250. *Binghampton Symposia in Geomorphology 4. Allen & Unwin*, London.

Gani, M.R. & Bhattacharya, J.P. (2005). Lithostratigraphy versus chronostratigraphy in facies correlations of Quaternary deltas: Application of bedding correlation. In: Bhattacharya, J.P. & Giosan, L. (Eds.) *River deltas: Concepts, models, and examples*. SEPM Special Publication, 83, 31–48, https://doi.org/10.2110/pec.05.83.0031

Gibling, M. R. (2006). Width and Thickness of Fluvial Channel Bodies and Valley Fills in the Geological Record: A Literature Compilation and Classification. *Journal of Sedimentary Research 76* (5): 731–770. https://doi.org/10.2110/jsr.2006.060

Gilbert, G.K., (1885). The topographic features of lake shores. U.S. Geological Survey Annual Report. 5, pp. 69–123.

Glover, T. J. (Ed.). (1997). *Pocket reference*. Sequoia Publishing.

Goudge, T.A., Milliken, R. E., Head, J.W., Mustard, J. F., Fassett, C. I. (2017). Sedimentological evidence for a deltaic origin of the western fan deposit in Jezero crater, Mars and implications for future exploration. *Earth and Planetary Science Letters*, 458, p. 357-365. https://doi.org/10.1016/j.epsl.2016.10.056

Goudge, T.A., Mohrig, D., Cardenas, B.T., Hughes, C.M., and Fassett, C.I., (2018). Stratigraphy and paleohydrology of delta channel deposits, Jezero crater, Mars. *Icarus* 301, 58–75. https://doi.org/10.1016/j.icarus.2017.09.034

Graham, G. H., Jackson, M. D., and Hampson, G. J. (2015). Three-dimensional modeling of clinoforms in shallow-marine reservoirs: Part 1. Concepts and application. *AAPG Bulletin, 99*, 6, pp. 1013-1047, https://doi.org/10.1306/01191513190

Gran, K. and Paola, C. (2001). Riparian vegetation controls on braided stream dynamics. *Water Resources Research 37*, 3275–3283, https://doi.org/10.1029/2000WR000203

Grotzinger, J. P., Sumner, D. Y., Kah, L. C., Stack, K., Gupta, S., Edgar, L., ... & Sirven, J. B. (2014). A habitable fluvio-lacustrine environment at Yellowknife Bay, Gale Crater, Mars. *Science*, *343*(6169):1242777, https://doi.org/10.1126/science.1242777

Grotzinger, J. P. et al. (2015). Deposition, exhumation, and paleoclimate of an ancient lake deposit, Gale crater, Mars. *Science, 350*, aac7575. https://doi.org/10.1126/science.aac7575

Gupta, S., Mangold, N., Caravaca, G., Gasnault, O., Dromart, G., Tarnas, J. D., et al. (2022). A delta-lake system at Jezero crater (Mars) from long distance observations. In *Paper presented at the 53rd Lunar and Planetary Science Conference, 2022*. Retrieved from http://www.hou.usra.edu/meetings/lpsc2022/pdf/2295.pdf

Gupta, S., Bell, J. F., Caravaca, G., Mangold, N., Stack, K., Kanine, O. A., et al. (2023). Fine-scale sedimentary architecture of the upper part of the Jezero western delta front. In *Paper presented at the 54th Lunar and Planetary Science Conference*, *2023*. Retrieved from https://www.hou.usra.edu/meetings/lpsc2023/pdf /2953.pdf

Gupta, S. et al., (2024). Going with the flow: Sedimentary evolution of the Jezero western fan, Mars. In *Paper presented at the 55th Lunar and Planetary Science Conference, 2024*. Retrieved from: https://www.hou.usra.edu/meetings/lpsc2024/pdf/2607.pdf

Hajek, E. & Edmonds, D. (2014). Is river avulsion style controlled by floodplain morphodynamics? *Geology, 42*, 3, 199-202, https://doi.org/10.1130/G35045

Hayden, A. T., & Lamb, M. P. (2020). Fluvial sinuous ridges of the Morrison Formation, USA: Meandering, scarp retreat, and implications for Mars. *Journal of Geophysical Research: Planets*, *125*, e2020JE006470. https://doi.org/10.1029/2020JE006470

Herbert, C., Alexander, J., Amos, K.J., & Fielding, C.R. (2019). Unit bar architecture in a highly-variable fluvial discharge regime: Examples from the Burdekin River, Australia. *Sedimentology*, *67*, 576–605, https://doi.org/10.1111/sed.12655

Herget, J. (2005). *Reconstruction of Pleistocene Ice-Dammed Lake Outburst Floods in the Altai Mountains, Siberia*. Geological Society of America Special Paper 386. https://doi.org/10.1130/0-8137-2386-8.1

Hiroki, Y. and Masuda, F. (2000). Gravelly spit deposits in a transgressive systems: The Pleistocene Higashikanbe Gravel, central Japan. *Sedimentology*, 47, 135–149, https://doi.org/10.1046/j.1365-3091.2000.00283.x

Ives, L., Stack, K., Gupta, S., Grotzinger, J. P., Lamb, M. P., Barnes, et al. (2023). Reassessing the sedimentary depositional origin of the Jezero crater western fan's curvilinear unit: Reconciling orbital and rover observations. In *Paper presented at the 2023 annual meeting of the American Geophysical Union*. https://agu.confex.com/agu/fm23/meetingapp.cgi/Paper/1367114

Jodhpurkar, M. J., Bell, J. F., III, Gupta, S., Horgan, B., Gwizd, S., Caravaca, G., & Randazzo, N. (2024). Mapping and characterizing the northern fan deposits in Jezero crater, Mars. *Journal of Geophysical Research: Planets*, 129, e2024JE008308. https://doi.org/10.1029/2024JE008308

Kanine, O. A., Ehlmann, B. L., Tate, C. D., Grotzinger, J., Paar, G., and Fischer, W. W. (2023). Stratigraphy and Sedimentology of Kodiak Butte, Jezero Crater, Mars. In *Paper presented at the 54th Lunar and Planetary Science Conference, 2023*. Retrieved from: https://www.hou.usra.edu/meetings/lpsc2023/pdf/2312.pdf

Kanine, O. A., Lamb, M. P., Grotzinger, J. P., Ehlmann, B. L., and Tate, C. D. (2024). Paleoenvironmental Analysis of Jezero Crater, Mars, from Stratigraphy and Sedimentology of Kodiak Butte. In Paper *presented at the 55th Lunar and Planetary Science Conference, 2024.* Retrieved from: https://www.hou.usra.edu/meetings/lpsc2024/pdf/1211.pdf

Ke, W.-T., and Capart, H. (2015). Theory for the curvature dependence of delta front progradation, *Geophysical Research Letters*, 42, 10,680–10,688, https://doi.org/10.1002/2015GL066455

Kleinhans, M. G. (2005). Autogenic cyclicity of foreset sorting in experimental Gilbert-type deltas. *Sedimentary Geology, v. 181*, 215–224. https://doi.org/10.1016/j.sedgeo.2005.09.001

Kleinhans, M.G. and van den Berg, J.H. (2011a). River channel and bar patterns explained and predicted by an empirical and a physics-based method. *Earth Surface Processes and Landforms, 36*: 721-738. https://doi.org/10.1002/esp.2090

Kleinhans, M. G., H. Markies, S. J. de Vet, A. C. in 't Veld, and F. N. Postema (2011b). Static and dynamic angles of repose in loose granular materials under reduced gravity. *Journal of Geophysical Research*, 116, E11004, https://doi.org/10.1029/2011JE003865

Korus, J. T, Joeckel, R. M., and Tucker, S. T. (2020). Genesis of giant, bouldery bars in a Miocene gravel-bed river: Insights from outcrop sedimentology, UAS-SfM photogrammetry, and GPR. *Journal of Sedimentary Research 90* (1): 27–47. https://doi.org/10.2110/jsr.2020.3

Lai, S. Y. J., Chiu, Y.-J., & Wu, F.-C. (2019). Self-similar morphodynamics of Gilbert and hyperpycnal deltas over segmented two-slope bedrock channels. *Water Resources Research*, 55, 3689–3707. https://doi.org/10.1029/2018WR023824

Lamb, M. P., W. E. Dietrich, and J. G. Venditti (2008). Is the critical Shields stress for incipient sediment motion dependent on channel-bed slope? *Journal of Geophysical Research,113*, F02008, https://doi.org/10.1029/2007JF000831

Leszczyński, S. and Nemec, W. (2015). Dynamic stratigraphy of composite peripheral unconformity in a foredeep basin. *Sedimentology*, 62: 645-680. https://doi.org/10.1111/sed.12155

Li, W., Colombera, L., Yue, D. and Mountney, N.P. (2023). Controls on the morphology of braided rivers and braid bars: An empirical characterization of numerical models. *Sedimentology*, 70: 259-279. https://doi.org/10.1111/sed.13040

Li, Z. Yan, C. Boota, M. W. (2022). Review and outlook of river morphology expression. *Journal of Water and Climate Change 13* (4): 1725–1747. https://doi.org/10.2166/wcc.2022.449

Liu, Y., Tice, M. M., Schmidt, M. E., Treiman, A. H., Kizovski, T. V., Hurowitz, J. A., et al. (2021). An olivine cumulate outcrop on the floor of Jezero crater, Mars. *Science*, 377(6614), 1513–1519. https://doi.org/10.1126/science.abo2756

Longhitano, S.G. (2008). Sedimentary facies and sequence stratigraphy of coarse-grained Gilbert-type deltas within the Pliocene thrust-top Potenza Basin (Southern Apennines, Italy). *Sedimentary Geology 210*, 87–110. https://doi.org/10.1016/j. sedgeo.2008.07.004.

Lunt, I.A., Bridge, J.S., and Tye, B. (2004). A quantitative, three-dimensional depositional model of gravelly braided rivers. *Sedimentology 51*, 377–414, https://doi.org/10.1111/j.1365-3091.2004.00627.x

Mäkinen, J. and Räsänen, M. (2003). Early Holocene regressive spit-platform and nearshore sedimentation on a glaciofluvial complex during the Yoldia Sea and the Ancylus Lake phases of the Baltic Basin, SW Finland. *Sedimentary Geology, 158*, 25-56. https://doi.org/10.1016/S0037-0738(02)00240-3

Mangold, N. et al., (2021). Perseverance rover reveals an ancient delta-lake system and flood deposits at Jezero crater, Mars. *Science 374*, 711-717(2021). https://doi.org/10.1126/science.abl4051

Mangold, N., Caravaca, G., Gupta, S., Williams, R. M. E., Dromart, G., Gasnault, O., et al. (2024). Architecture of fluvial and deltaic deposits exposed along the eastern edge of the western fan of Jezero crater, Mars. *Journal of Geophysical Research: Planets, 129*, e2023JE008204. https://doi.org/10.1029/2023JE008204

Marren, P. M. (2005). Magnitude and frequency in proglacial rivers: a geomorphological and sedimentological perspective. *Earth-Science Reviews 70*, 203–251. https://doi.org/10.1016/j.earscirev.2004.12.002

Maurice, S., Wiens, R.C., Saccoccio, M. et al. (2012). The ChemCam Instrument Suite on the Mars Science Laboratory (MSL) Rover: Science Objectives and Mast Unit Description. *Space Science Reviews 170*, 95–166. https://doi.org/10.1007/s11214-012-9912-2

Maurice, S., Wiens, R.C., Bernardi, P. et al. (2021). The SuperCam Instrument Suite on the Mars 2020 Rover: Science Objectives and Mast-Unit Description. *Space Science Reviews 217*, 47. https://doi.org/10.1007/s11214-021-00807-w

McEwen, A.S. et al. (2007). Mars Reconnaissance Orbiter's High Resolution Imaging Science Experiment (HiRISE), *Journal of Geophysical Research 112*, E05S04. https://doi.org/10.1029/2005JE002605

Mellmann, J. (2001). The transverse motion of solids in rotating cylinders—forms of motion and transition behavior. *Powder Technology, 118*, 3, 251-270 https://doi.org/10.1016/S0032-5910(00)00402-2

Miall, A.D. (2006). The Geology of Fluvial Deposits: Sedimentary Facies, Basin Analysis, and Petroleum Geology. 4th ed. *Springer, Heidelberg,* 582 pp., https://doi.org/10.1007/978-3-662-03237-4

Mikes, D. and Geel, C. R. (2006). Standard facies models to incorporate all heterogeneity levels in a reservoir model. *Marine and Petroleum Geology*, *23*, 943-959. https://doi.org/10.1016/j.marpetgeo.2005.06.007

Montgomery, D. R., Hallet, B., Yuping, L. et al. (2004). Evidence for Holocene megafloods down the Tsangpo River gorge, southeastern Tibet. *Quaternary Research*, *62*, 201–207, https://doi.org/10.1016/j.yqres.2004.06.008

Morgan, A.M., Howard, A.D., Hobley, D.E.J., et al. (2014). Sedimentology and climatic environment of alluvial fans in the martian Saheki crater and a comparison with terrestrial fans in the Atacama Desert. *Icarus* 229, 131–156. https://doi.org/10.1016/j.icarus.2013.11.007.

Mortimer, E., Gupta, S., and Cowie, P. (2005). Clinoform nucleation and growth in coarse-grained deltas, Loreto basin, Baja California Sur, Mexico: A response to episodic accelerations in fault displacement. *Basin Research 17*, 337–359, https://doi.org/10.1111/j.1365-2117.2005.00273.x

Nemec, W. and Steel, R.J. (Eds.). (1988). *Fan Deltas: Sedimentology and Tectonic Settings*, Blackie, London.

Nielsen, L.H., Johannessen, P.N. and Surlyk, F. (1988). A Late Pleistocene coarse-grained spit-platform sequence in northern Jylland, Denmark. *Sedimentology*, *35*, 915–937, https://doi.org/10.1111/j.1365-3091.1988.tb01738.x

Nijhuis, A. J. et al. (2015). Fluvio-deltaic avulsions during relative sea-level fall. *Geology*, *42*. https://doi.org/10.1130/G36788.1

O'Connor, J. E. (1993). *Hydrology, Hydraulics and Geomorphology of the Bonneville Flood*. Special Paper, *Geological Society of America*, 274, https://doi.org/10.1130/SPE274

Olariu, C. and Bhattacharya, J. P. (2006). Terminal distributary channels and delta front architecture of river-dominated delta systems. *Journal of Sedimentary Research* 76 (2): 212–233. https://doi.org/10.2110/jsr.2006.026

Paola, C. and Borgman, L. (1991). Reconstructing random topography from preserved stratification. *Sedimentology, 38*, 553–565, https://doi.org/10.1111/j.1365-3091.1991.tb01008.x

Paola, C. and Mohrig, D. (1996). Palaeohydraulics revisited: Palaeoslope estimation in coarse-grained braided rivers. *Basin Research*, *8*: 243-254. https://doi.org/10.1046/j.1365-2117.1996.00253.x

Pardee, J.T. (1942). Unusual currents in glacial Lake Missoula, Montana. *Geological Society of America Bulletin, 53*: 1569-1600, https://doi.org/10.1130/GSAB-53-1569

Parker, G. (1976). On the cause and characteristic scales of meandering and braiding in rivers. *Journal of Fluid Mechanics*, *76*(3), 457–480. https://doi.org/10.1017/S0022112076000748

Parker, G. and Peterson, A. W. (1980). Bar resistance of gravel- bed streams. *Journal of the Hydraulics Division, 106* (HY10), 1559–1575, https://doi.org/10.1061/JYCEAJ.000552

Parker, G. (2004). Approximate Formulation for slope and bankfull geometry of rivers in 1D sediment transport morphodynamics with applications to rivers and turbidity currents, E-book. [Available at http://hydrolab.illinois.edu/people/parkerg/morphodynamics_e-book.htm.]

Patruno, S., Hampson, G.J., Jackson, C.A. (2015). Quantitative characterisation of deltaic and subaqueous clinoforms. *Earth Science Reviews 142*, 79–119, https://doi.org/10.1016/j.earscirev.2015.01.004

Pomeroy, J. W., de Boer, D., and Martz, L. W. (2005). Hydrology and Water Resources of Saskatchewan: Centre for Hydrology Report #1, Centre for Hydrology, University of Saskatchewan. [Available at https://research-groups.usask.ca/hydrology/documents/pubs/papers/pomeroy_et_al_2005.pdf]

Postma, G., 1990. Depositional architecture and facies of river and fan deltas: a synthesis. In: Colella, A., Prior, B.D. (Eds.), *Coarse-Grained Deltas*. *International Association of Sedimentologists Special Publication. vol. 10*. *Blackwell Scientific Publications*, pp. 13–27. https://doi.org/10.1002/9781444303858.ch2.

Postma, G. (1995) Sea-Level related architectural trends in coarse-grained delta complexes. *Sedimentary Geology, 98*, 3-12. https://doi.org/10.1016/0037-0738(95)00024-3

Quantin-Nataf, C., Alwmark, S., Calef, F. J., Lasue, J., Kinch, K., Stack, K. M., et al. (2023). The complex exhumation history of Jezero crater floor unit and its implication for Mars sample return. *Journal of Geophysical Research: Planets, 128*, e2022JE007628. https://doi.org/10.1029/2022JE007628

Quinn, D. P., & Ehlmann, B. L. (2019). A PCA-based framework for determining remotely sensed geological surface orientations and their statistical quality. *Earth and Space Science*, 6, 1378–1408. https://doi.org/10.1029/2018ea000416

Rees, C., Palmer, J. & Palmer, A. (2017). Gilbert-style Pleistocene fan delta reveals tectonic development of North Island axial ranges, New Zealand. *New Zealand Journal of Geology and Geophysics*, 61(1), 64–78. https://doi.org/10.1080/00288306.2017.1406377

Rickenmann, D. and Recking, A. (2011). Evaluation of flow resistance in gravel-bed rivers through a large field data set. *Water Resources Research*, 47, W07538. https://doi.org/10.1029/2010WR009793

Rowland, J. C., M. T. Stacey, and W. E. Dietrich (2009). Turbulent characteristics of a shallow wall-bounded plane jet: Experimental implications for river mouth hydrodynamics, *Journal of Fluid Mechanics, 627*, 423–449, https://doi.org/10.1017/S0022112009006107

Schomacker, E. R. et al. (2010). Recognition and significance of sharp-based mouth-bar deposits in the Eocene Green River Formation, Uinta Basin, Utah. *Sedimentology 57*, 1069-1087. https://doi.org/10.1111/j.1365-3091.2009.01136.x

Schon, S.C., Head, J.W., and Fassett, C.I. (2012). An overfilled lacustrine system and progradational delta in Jezero crater, Mars: Implications for Noachian climate. Planet. Space Sci. 67 (1), 28–45. https://doi.org/10.1016/j.pss.2012.02.003.

Shahrzad, S., Kinch, K. M., Goudge, T. A., Fassett, C. I., Needham, D. H., Quantin-Nataf, C., & Knudsen, C. P. (2019). Crater statistics on the dark-toned, mafic floor unit in Jezero Crater, Mars. *Geophysical Research Letters*, *46*(5), 2408–2416. https://doi.org/10.1029/2018GL081402

Silberman, E., R. Carter, H. Einstein, J. Hinds, R. Powell, and ASCE Task Force on Friction Factors in Open Channels. (1963). Friction factors in open channels, *Journal of Hydraulic Engineering, 89(HY2)*, 97–143, https://doi.org/10.1061/JYCEAJ.0000865

Simon, J. I., Hickman-Lewis, K., Cohen, B. A., Mayhew, L. E., Shuster, D. L., Debaille, V., et al. (2023). Samples collected from the floor of Jezero Crater with the Mars 2020 perseverance rover. *Journal of Geophysical Research: Planets, 128*, e2022JE007474. https://doi.org/10.1029/2022je007474

Slingerland, R., & Smith, N.D. (2004). River avulsions and their deposits. *Annual Review of Earth and Planetary Sciences, 32*, 257-285. https://doi.org/10.1146/ANNUREV.EARTH.32.101802.120201

Smith, N.D. (1974). Sedimentology and bar formation in the upper Kicking Horse River, a braided meltwater stream. *Journal of Geology 82*, 205–223, https://doi.org/10.1086/627959

Smith, S.A., (1989). Sedimentation in a meandering gravel-bed river: the River Tywi, South Wales. *Geological Journal, v. 24*, p. 193–204, https://doi.org/10.1002/gj.3350240304

Smith, S.A., (1990) The sedimentology and accretionary styles of an ancient gravel-bed stream: the Budleigh Salterton Pebble Beds (Lower Triassic), southwest England. *Sedimentary Geology*, *v. 67*, p. 199–219, https://doi.org/10.1016/0037-0738(90)90035-R

Spaggiari, R. and Bordy, E.M. (2023), Anatomy of a diamondiferous gravel barrier spit at the palaeo-Orange River mouth, south-western Namibia. *Sedimentology*, *70*: 1630-1654. https://doi.org/10.1111/sed.13090

Stack, K.M., Williams, N.R., Calef, F. et al. (2020). Photogeologic map of the Perseverance rover field site in Jezero crater constructed by the Mars 2020 Science Team. *Space Science Reviews 216*, 127. https://doi.org/10.1007/s11214-020-00739-x

Steel, R.J., and Thompson, D.B. (1983). Structures and textures in Triassic braided stream conglomerates (‘‘Bunter’’ Pebble Beds) in the Sherwood Sandstone Group, North Staffordshire, England. *Sedimentology*, v. *30*, p. 341–367, https://doi.org/10.1111/j.1365-3091.1983.tb00677.x

Straub, K. M., Paola, C., Mohrig, D., Wolinsky, M. A., & George, T. (2009). Compensational stacking of channelized sedimentary deposits. *Journal of Sedimentary Research*, *79*(9), 673–688, https://doi.org/10.2110/jsr.2009.070

Summons, R.E., Amend, J.P., Bish, D., Buick, R., Cody, G.D., Des Marais, D.J., Dromart, G., Eigenbrode, J.L., Knoll, A.H. and Sumner, D.Y. (2011). Preservation of martian organic and environmental records: Final report of the Mars biosignature working group. *Astrobiology 11*, 157–181, https://doi.org/10.1089/ast.2010.0506

Sun, V. Z., Hand, K. P., Stack, K. M., Farley, K. A., Simon, J. I., Newman, C., et al. (2023). Overview and results from the Mars 2020 Perseverance rover's first science campaign on the Jezero crater floor. *Journal of Geophysical Research: Planets, 128*, e2022JE007613. https://doi.org/10.1029/2022JE007613

Tate, C. D. et al. (2023). Stratigraphic reconstruction and analysis of the delta remnant Kodiak in Jezero crater, Mars. In *Paper presented at the 54th Lunar and Planetary Science Conference, 2023*. Retrieved from: https://www.hou.usra.edu/meetings/lpsc2023/pdf/1473.pdf

Tate, C. D., Hayes, A. G., Kanine, O., Gupta, S., Caravaca, G., Paar, G., ... & Rice, J. (2024). Stratigraphic reconstruction and analysis of the delta remnant Kodiak in Jezero crater, Mars. *Authorea Preprints*.

Teller, J. T. (2004). Controls, history, outbursts, and impact of large late-Quaternary proglacial lakes in North America. In *The Quaternary Period in the United States, INQUA Anniversary Volume*, eds. A. Gilespie, S. Porter and B. Atwater. *Elsevier*, pp. 45–6, https://doi.org/10.1016/S1571-0866(03)01003-0

Vakarelov, B. K and Ainsworth, B. R. (2013). A hierarchical approach to architectural classification in marginal-marine systems: Bridging the gap between sedimentology and sequence stratigraphy. *AAPG Bulletin*, *97* (7): 1121–1161. https://doi.org/10.1306/11011212024

van Yperen, A.E., Poyatos-Moré, M., Holbrook, J.M., Midtkandal, I. (2020). Internal mouth-bar variability and preservation of subordinate coastal processes in low-accommodation proximal deltaic settings (Cretaceous Dakota Group, New Mexico, USA). *Depositional Record 6*: 431–458. https://doi.org/10.1002/dep2.100

Viparelli, E., Blom, A. & Parker, G. (2012). Modeling stratigraphy formed by prograding Gilbert deltas. In *River Flow*, Murillo Munoz, R. (Ed.). *Taylor & Francis Group*, London, 827-836.

Winsemann, J., Lang, J., Polom, U., Loewer, M., Igel, J., Pollok, L. & Brandes, C. (2018). Ice-marginal forced regressive deltas in glacial lake basins: geomorphology, facies variability and large-scale depositional architecture. *Boreas*. https://doi.org/10.1111/bor.12317

Winsemann, J., Lang, J., Fedele, J.J., Zavala, C., Hoyal, D.C.J.D. (2021). Re-examining models of shallow-water deltas: Insights from tank experiments and field examples. *Sedimentary Geology 421*. https://doi.org/10.1016/j.sedgeo.2021.105962

Wolman, M.G. (1954). A method of sampling coarse river-bed material. *Transactions of the American Geophysical Union, 35*(6):951-956.

Wright, L. D. (1977). Sediment transport and deposition at river mouths: A synthesis. *Geological Society of America Bulletin, 88*(6), 857–868. https://doi.org/10.1130/0016-7606(1977)88<857:STADAR>2.0.CO;2

Zhang, X., Lin, C., Zhang, T., Huang, D., Huang, D., Liu, S. (2021). New understanding of bar top hollows in dryland sandy braided rivers from outcrops with unmanned aerial vehicle and ground penetrating radar surveys. *Remote Sensing, 13,* 560. https://doi.org/10.3390/rs13040560

Figures

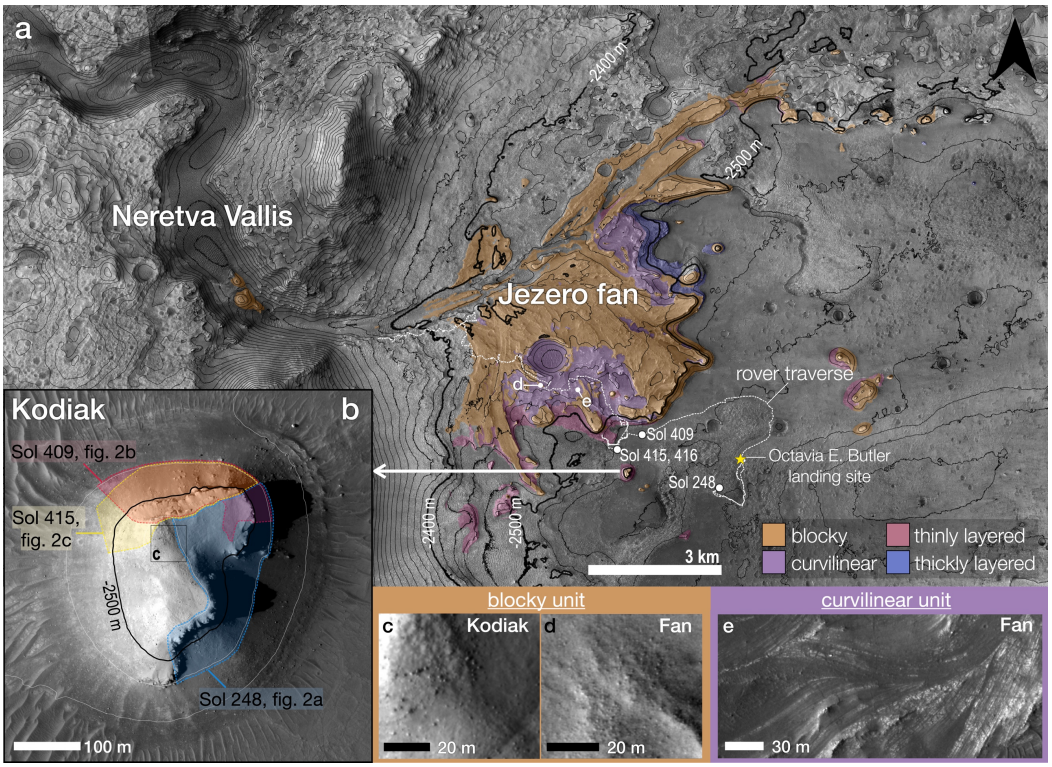

Figure 1. Geologic context of Kodiak Butte in Jezero Crater. Part **a** shows rover traverse up to sol 1144 and orbital unit mapping from Stack et al., 2020 over HiRISE (most of panel) and CTX (upper left) orthomosaics. 20 m elevation contours in **a** and **b** are from HiRISE DEM where available (most of figure) and CTX DEM otherwise (upper left of **a**), with -2400 m and -2500 m elevation contours in bolder black. Rover locations for Mastcam-Z Sol 248, 409, and 415 and 416 images are noted, with 68 m separating Sols 415 and 416 imaging locations. Locations of parts **d** and **e** are also annotated. Inset of Kodiak in part **b** uses HiRISE image PSP_002387_1985. The faces visible in Sol 248, 409, and 415/416 cropped Mastcam-Z mosaics shown in **Figure 2a**, **2b**, and **2c** are highlighted in blue, red, and yellow, respectively. Location of boulders atop Kodiak shown in part **c** is outlined in black solid line within part **b**. Example of blocky unit boulders from the fan top is shown in **d**, while **e** shows an example fan top exposure of the curvilinear unit.

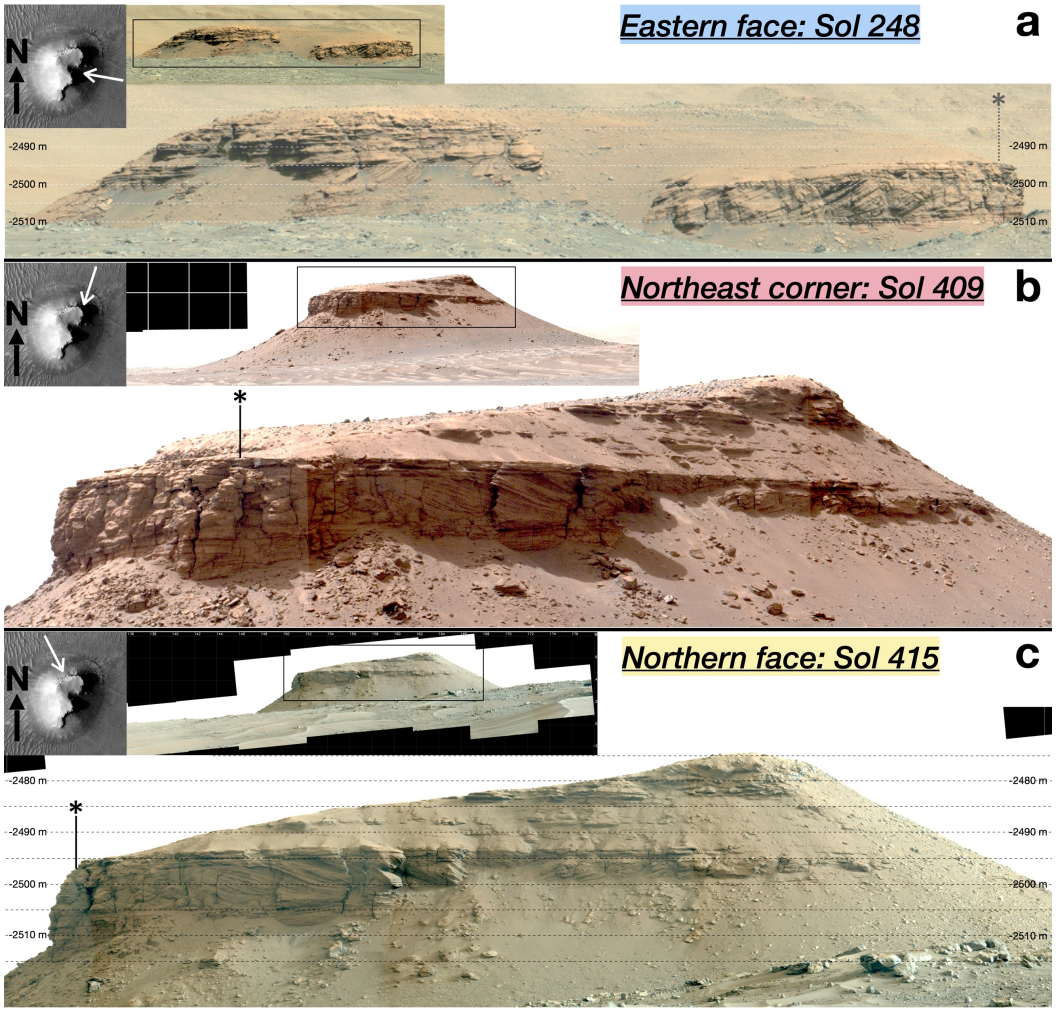

Figure 2. Three key Mastcam-Z views of Kodiak. All mosaics are taken with focal length 110 mm and are cropped and color-enhanced for ease of viewing. White arrows on HiRISE context images in the upper left of each panel approximate look directions from imaging locations shown in **Figure 1a**. Asterisk indicates the location of the central axis of one of the antiformal structures for purposes of orientation reference and is shown in black where this axis is visible in the mosaic (parts **b** and **c**) and gray when the axis is behind the face shown (part **a**). Panel title highlights correspond to the colors overlaid on Kodiak faces shown in planview in **Figure 1b**. Part **a**: Sol 248, sequence I.D. 08270. **b**: Sol 409, seq. I.D. 08425. **c**: Sol 415, seq. I.D. 08430. This mosaic was taken at a very similar angle to that of the slightly higher-resolution Sol 416 mosaic (key in 3D model construction) but has marginally better lighting for viewing with human eyes.

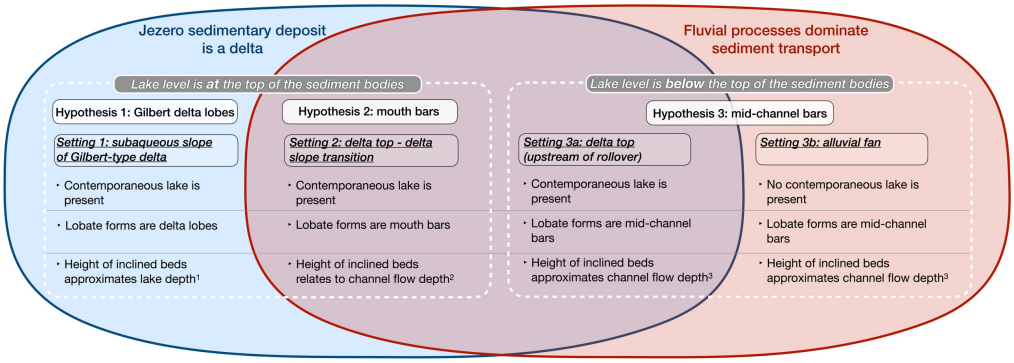

Figure 3. Depositional hypotheses for Kodiak butte. Presented are three possible landform types and 4 possible depositional environments for the antiformal structures with large-scale steeply-inclined beds, along with their implications for a contemporaneous lake level. Venn diagram highlights key similarities and differences in these hypotheses. Important references: [1]Patruno et al., 2015; [2]Edmonds and Slingerland, 2007 and Wright, 1977; [3]Mohrig et al., 2000.

Figure 4. Example of various fluvio-deltaic environments in the Goose River Delta in Goose Bay of Lake Melville in Labrador, Canada. The Goose River Delta is predominantly composed of noncohesive median sand (Caldwell and Edmonds, 2014; Nijhuis et al., 2015), has a semicircular planform geometry, and its top is dominated by braided channels (Caldwell and Edmonds, 2014). The Goose River is 100-200 m wide and 2-3 m deep in its lower reaches (Nijhuis et al., 2015) and conducts up to 500 m^3/s water in spring and summer flows (Coachman, 1953). Goose Bay is ~10 m deep near the shore and 20-40 m deep otherwise (Blake, 1956). **a**: Overview of the Goose River delta system, showing both active and abandoned lobes, demonstrating the process of avulsion. Examples of alternate bank-attached bars, mid-channel bars, and meander cutoffs are labelled. (Continued next page.)

Figure 4 caption, continued… **b**: The largest active lobe of the delta. Flow is roughly southeast (to the lower right). Downstream-migrating unit bars (shaded in pink and outlined in white dotted line) with arcuate fronts (solid white line) are frequently amalgamated in compound bars (two examples outlined in pink dotted line) on the delta top. The largest channel is outlined in blue dashed line. We approximate the transition from subaerial to subaqueous deposits as the shoreline, represented with white dotted line. Basinward from the shoreline, approximate delta front/slope is shaded in teal. Note this mapping is not intended to exactly represent the location of the transitions from delta top to delta front or delta front to lakebed, but rather to indicate the general location and spatial relationships of the depositional environments. **c**: Context image demonstrating the overlap in spatial scales for lobate landforms, even within a consistent climate: here we see an entire lobe of the Goose River delta is comparable in width to compound mid-channel bars in the braided Churchill River <10 km away.

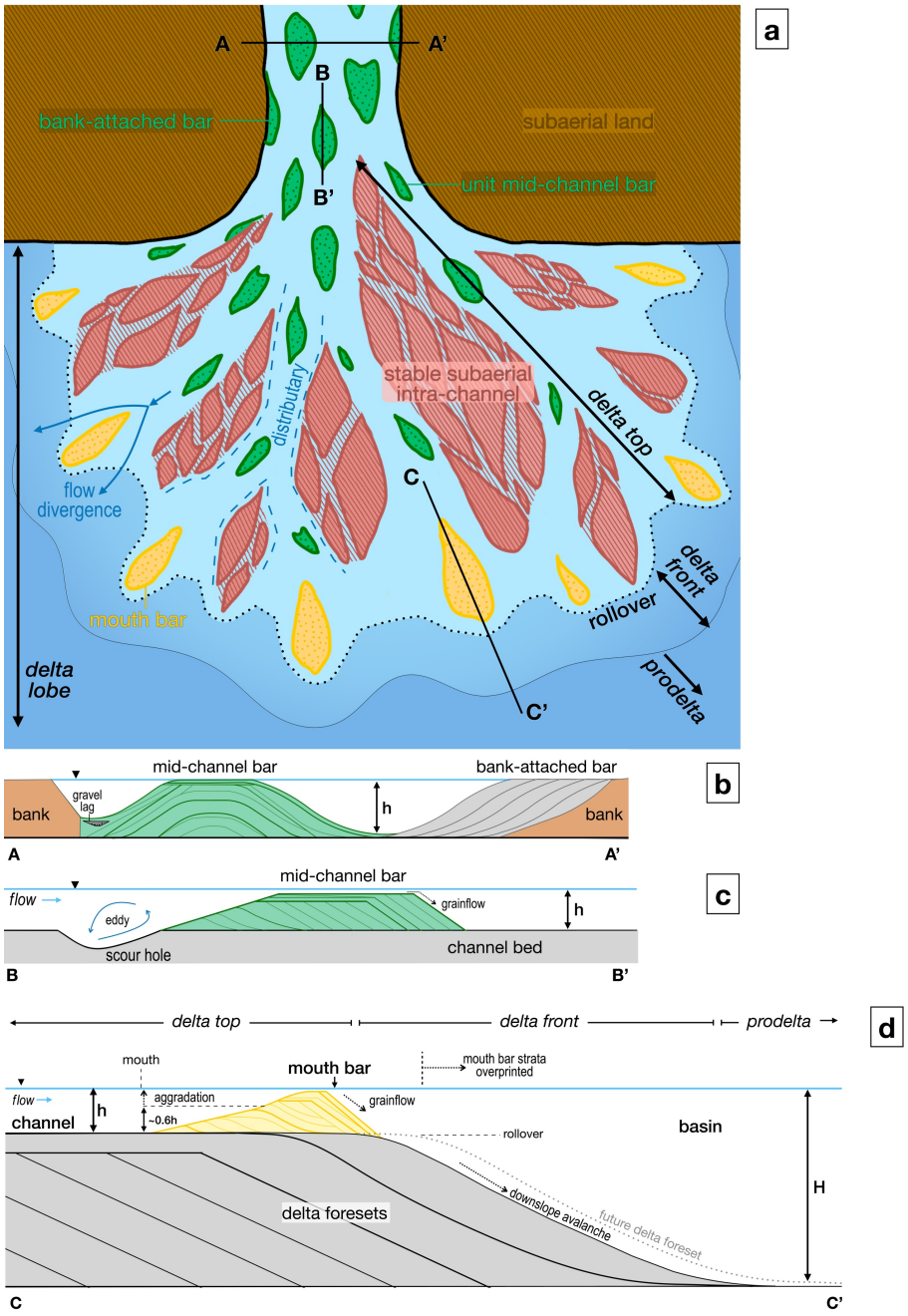

Figure 5. Schematic of delta and river channel anatomy. **a**: Schematic of a delta lobe, with topset dominated by braided channels, a roughly semicircular planform geometry, and low-to-moderate shoreline rugosity. In order to portray both well-developed and protruding mouth bars (atypical of Gilbert deltas) and steep delta foresets (typical of Gilbert deltas) we imagine a hypothetical intermediate scenario where the bedload is coarse sediment, but sufficient cohesion (e.g. Caldwell and Edmonds, 2014) or jet instability (Canestrelli et al., 2014) exists such to promote levee growth and thus encourage … (continued next page).

Figure 5 caption, continued. … mouth bar development while preserving the steep front. This schematic is not intended to reflect a particular real-world system or convey scale. **b**: A-A' shows transverse (flow perpendicular) cross section of a vertically and downsteam-accreting mid-channel braid bar and a bank-attached bar. Flow is out of page. *h* represents bankfull flow depth in the channel; note variation in channel topography such that flow depth varies across the transect and is recorded as such in the height of beds in the mid-channel bar. A comparable cross-section of a mouth bar would show similar concave-down geometry. **c**: B-B' shows longitudinal (flow parallel) cross section of a vertically and downsteam-accreting mid-channel braid bar, with fronts dipping at roughly angle of repose, and a scour hole trailing the bar. **d**: C-C' gives a longitudinal cross-section of the delta top and mouthbar, delta front, and prodelta. *h* represents channel bankfull depth while *H* represents the (greater) basin depth. At heights < 0.6h the mouth bar is dominated by progradation and aggradation, where after reaching that height vertical aggradation dominates. We diagram the mouth bar beginning to prograde over the delta rollover, whereupon mass transport of sediment down the delta slope will eventually build another delta foreset.

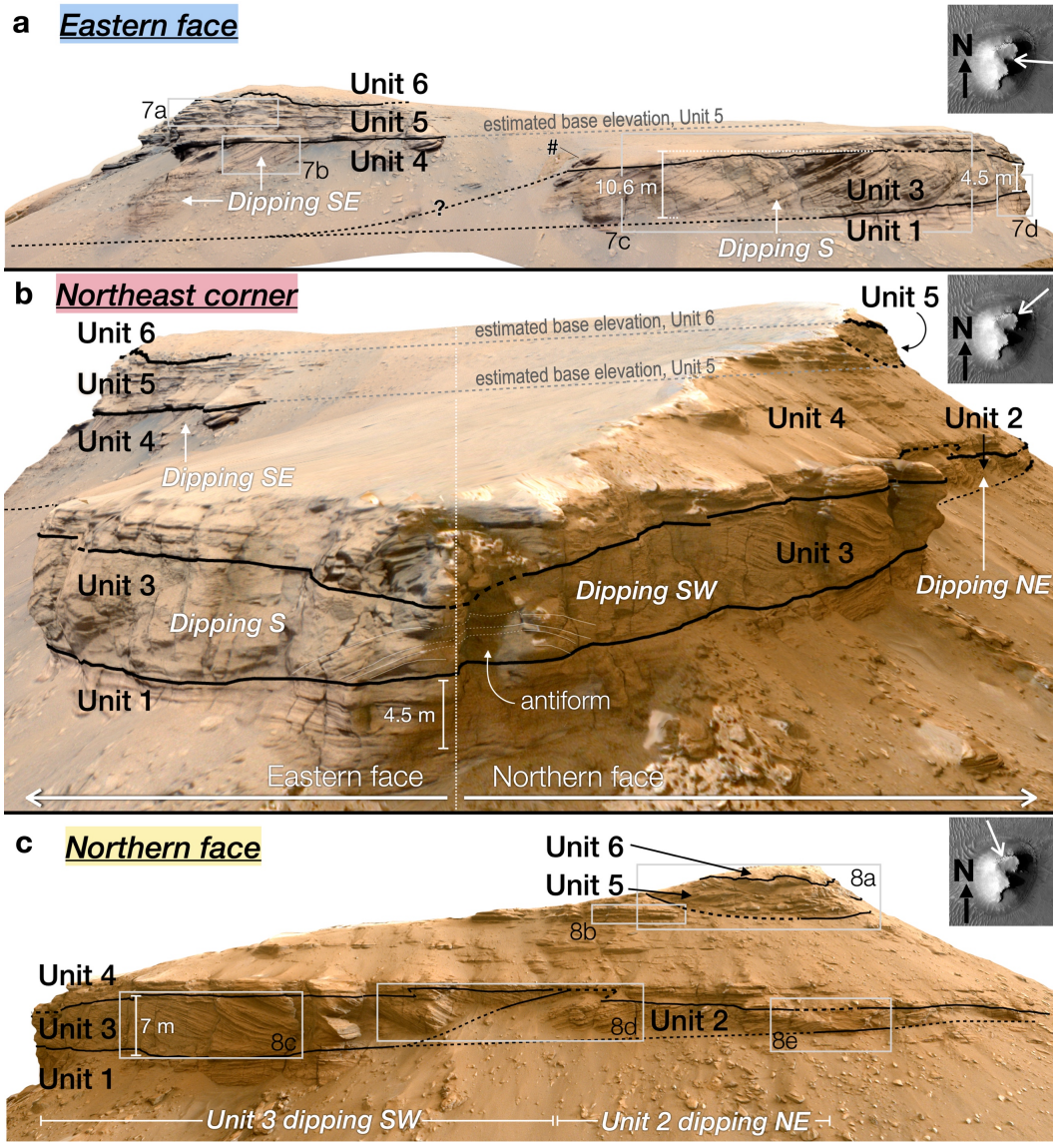

Figure 6. Three perspectives of Kodiak using the 3D model. White arrows on HiRISE orbital views (upper right in each panel) show look directions. Black lines mark the divisions between units; solid where certain, dashed where inferred. Part **a** shows the eastern face of Kodiak, with the viewer looking toward 276˚(west, north is 0˚). "#" notes the location of a small-scale set of steeply-inclined beds. **b** shows the northeast corner looking to the southwest at 220˚. **c** shows the northern face, with the viewer looking southeast at 176˚. Gray boxes in parts **a** and **c** indicate locations of zoomed-in images in **Figures 7** and **8**. Primary dip directions of sets of inclined beds are noted in each part.

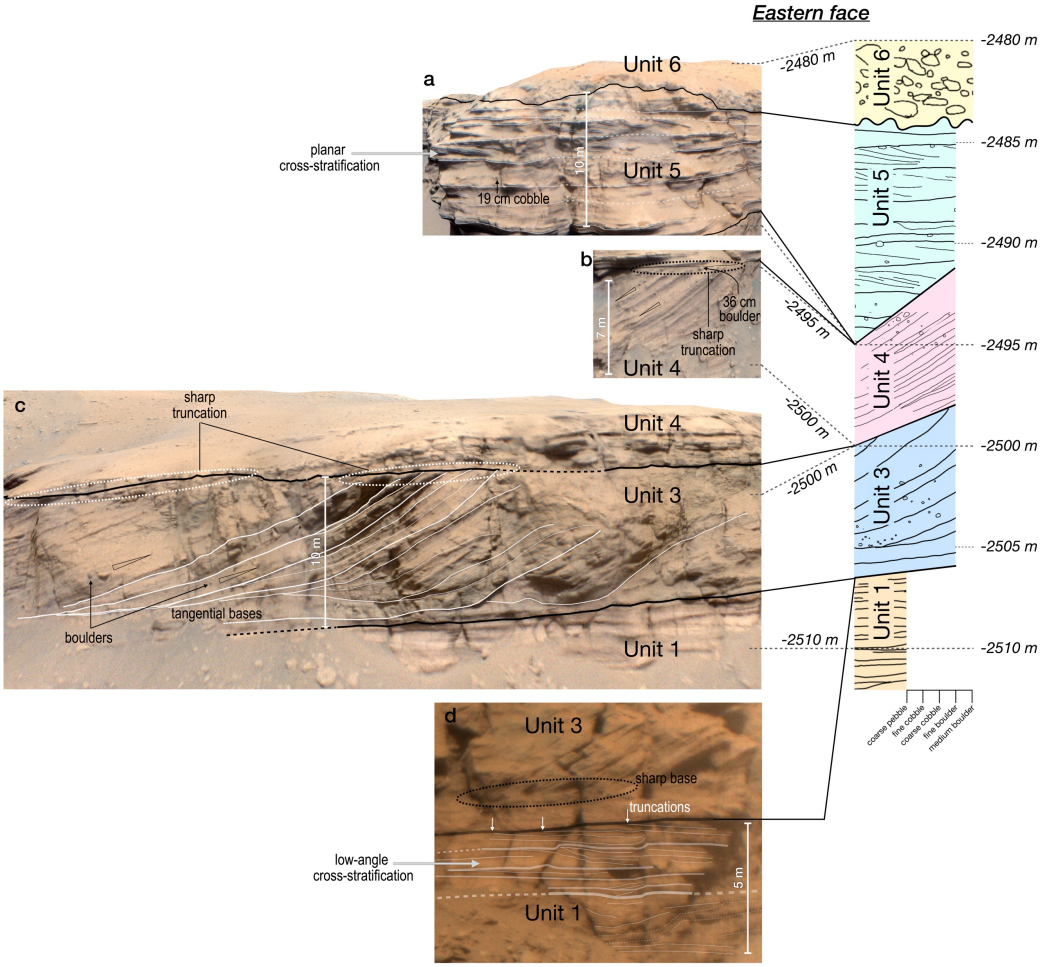

Figure 7. Representative stratigraphic section of the eastern face of Kodiak, highlighting key lithofacies in each unit. Approximate locations of parts **a-d** are shown in **Figure 6a**; note that the viewing perspectives shown here may be different from **6a** to best highlight the features of interest. Foreshortening in the images due to the three-dimensional nature of the model means scale bars may not be valid throughout the entire image and are intended to only be representative in the location they are placed. The column to the right shows typical elevation ranges of unit contacts (black lines) and records the largest grain size (bins following modified Udden-Wentworth scale, Blair and McPherson, 1999) found in each unit. Dotted gray lines mark the approximate locations of elevation contours. Parts **a-c** utilize the 3D model; part **d** shows a SuperCam Sol 77 natural color image.

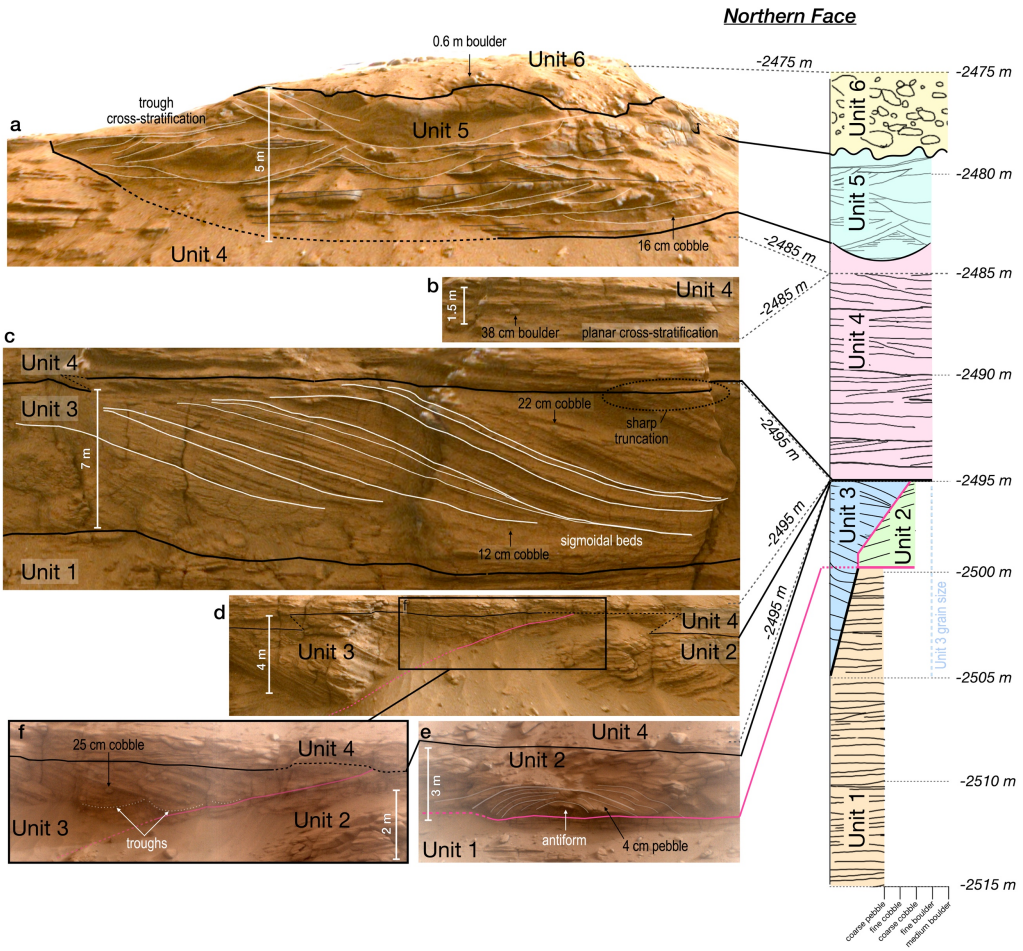

Figure 8. Representative stratigraphic section, as in **Figure 7**, but of the northern face of Kodiak. Approximate locations of parts **a-e** are shown in **Figure 6c**. Unit contacts are again in black line, except for the Unit 1-2 and 2-3 boundaries, which are shown in pink to aid in in differentiation from other contacts. Note simplifications for readability: the Unit 1-3 contact on the northern face occurs typically at ~ -2505 m, while the Unit 1-2 contact occurs just above -2500 m where visible. The Unit 2-3 contact is visible between ~ -2497 m and -2495 m but is inferred to continue under cover of regolith. In summary, Unit 3 overlies Unit 2; the two are exposed at overlapping elevations but are laterally offset; and Unit 3 occurs at a wider range of elevations than Unit 2. Parts **a-d** use the 3D model; part **e** uses SuperCam Sol 580 image LRF_0580_0718440221_487RAD_N0290000SCAM01580_0040I9J01; part **f** uses manually aligned and flat-field corrected SuperCam Sol 580 images LRF_0580_0718440726_489RAD_N0290000SCAM01580_0080I9J01 and LRF_0580_0718440823_515RAD_N0290000SCAM01580_0090I9J01.

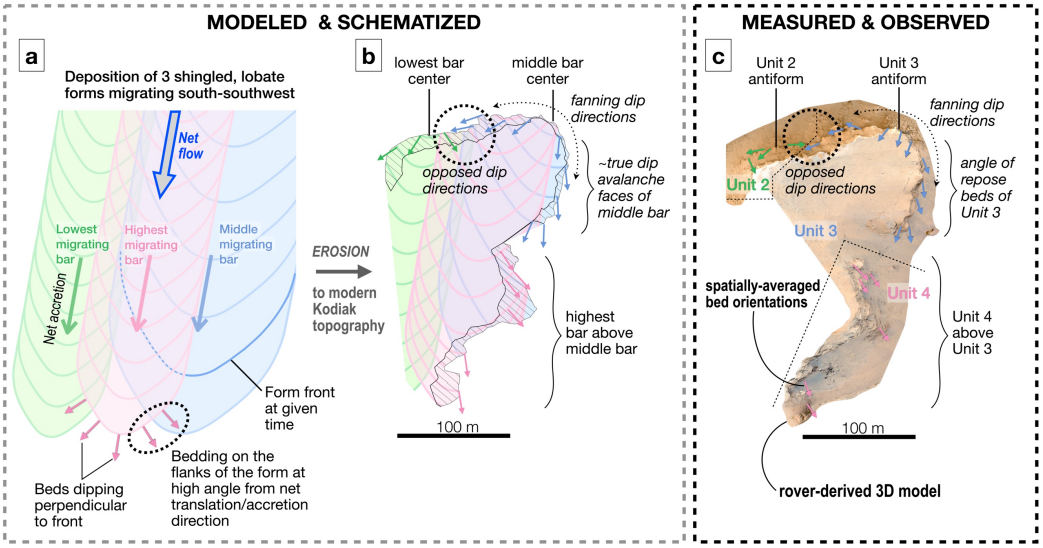

Figure 9. Schematic comparing depositional model and bed orientation observations for Units 2, 3, and 4. **a** three idealized, overlapping lobate barforms migrating south-southwest; stratigraphic position (lowest, middle, highest) is noted. Bar behavior is approximated as unidirectional downstream migration (i.e., no rotations or lateral migration). Solid lines represent arcuate bar fronts at a given time during their downstream migration, with strata dipping perpendicular to the front. **b**: Predicted features and bed directions exposed in outcrop when the bar deposits are eroded to Kodiak's modern topography. **c**: Mean bed azimuths for 21 groups (non-averaged data available as Supplemental Data Set ds01.xlsx) as measured on DOM. Dotted black lines divide locations of unit exposures and are not intended to convey information about subsurface stratigraphic relationships.

Chapter 4

COMPARISON OF REMOTELY-SENSED ORBITAL AND ROVER-BASED *IN-SITU* SURFACE ORIENTATION ANALYSES IN JEZERO CRATER, MARS

O. A. Kanine[1], B. L. Ehlmann[1], & & P. D. Asimow[1]

[1]Division of Geological and Planetary Sciences, California Institute of Technology, Pasadena, CA

Corresponding author: Oak Kanine (oak.kanine@caltech.edu)

In preparation for submission to JGR: Planets.

Key Points:

- Ground-truthing with rover images shows surface orientations calculated with orbital datasets are accurate
- Outcrop lithology and micro- to meso-scale internal deposit stratigraphic architecture cannot be reliably determined from orbit
- Specificity at the level required to test sediment transport hypotheses typically requires rover investigations

Abstract

Orbital data has been used to estimate the three-dimensional orientation of rock exposures or topographic features on Mars interpreted as bedding planes. The results have supported interpretations of internal deposit characteristics and depositional environments. However, opportunities to ground-truth these estimates and to understand the geologic information recorded by the measured surfaces are limited to sites visited by rovers or landers. We performed a quantitative comparison of five orbitally-derived plane fits of scarps, light-toned bands, and other layer-like features exposed in outcrops in the Jezero crater Western fan with both orientations and up-close geologic interpretations of the same features constrained by images of the landscape taken by the Perseverance rover. Both orbitally-derived orientation solutions and those calculated numerically from two or more *in-situ* apparent dip measurements almost always fall within broad orientation constraints set by apparent dip angles and dip directions seen in rover images. Additionally, the rover- and orbital-based solutions often overlap within mutual uncertainty. However, only one of five features traced from orbit was confirmed in rover images to constitute a single bed, indicating that our ability to distinguish hierarchical stratigraphic elements, lithologies, and stratal structures from orbit is limited and poses a challenge better addressed by *in-situ* investigation with landed spacecraft. Nevertheless, certain outcrop characteristics such as light tone and moderate-to-steep inclination may aid in identifying beds or self-similar packages of strata from orbit.

Plain Language Summary

Data from orbiting satellites has been used to describe the structure of rock deposits on Mars by measuring the orientation (angle and direction of inclination) of features inferred to be sedimentary beds. These measurements have been used to make interpretations of depositional environment. We ground-truth satellite measurements of layer-like features exposed in the Jezero crater Western fan with on-the-ground images taken by the Perseverance rover. We establish broad constraints on feature orientations using apparent dip angles and directions in rover images and find numerical solutions for these orientations using observations taken from multiple perspectives. Rover observations indicate that feature orientations derived from orbital data are accurate. However, we find that layer-like features seen from orbit are not always beds, but rather represent a variety of rock types, packages, and erosional surfaces.

1 Introduction

The orientation of bedding planes and the stratigraphic architecture of sedimentary rocks is used to describe facies, identify sediment transport direction and processes, and, on a larger scale, differentiate between depositional environments and understand the succession over time of said environments. On Earth, such work frequently relies on field studies in which geologists are on the ground and can examine by eye outcrops at meter-scale range and make measurements (strike-dip, grain size, etc.) directly on the rock exposure. Recent decades have witnessed the introduction of three-dimensional outcrop models sourced from drone (unmanned

aerial vehicle, UAV) imagery and structure-from-motion (SfM) pipelines (e.g., Korus et al., 2020; Quinn and Ehlmann, 2019a; Hayden and Lamb, 2020), which bridge *in-situ* and remote sensing approaches. Just as on Earth, characterization of ancient environments on Mars and how they changed over time is required to understand how climates evolve and how habitable environments develop and decline.

Studies have utilized 3D datasets from rover stereo images (e.g. Stein et al., 2020, Banham et al., 2018) or SfM photogrammetry (e.g. Caravaca et al., 2024; Barnes et al., 2018) and plane-fitting algorithms in an attempt to describe the attitude of surfaces such as bedding planes and thus identify depositional environments or differentiate between formation hypotheses on Mars. As the percentage of the martian surface explored by rovers or landers is extremely small, other studies have leveraged orbital datasets such as HiRISE visible wavelength images and DEMs (digital elevation models), which have much more complete spatial coverage. These studies have analyzed unit contacts (Stein et al., 2020; Quinn & Ehlmann, 2019a) and bedding planes (e.g., Okubu, 2010), including in Jezero Crater (Goudge et al., 2017), the landing site of the NASA Mars 2020 mission's Perseverance rover. Such analyses rely on both the accurate calculation of the surface's orientation and accurate determination of the surface type (i.e., the ability to distinguish between in-place bedrock and surficial cover, and, if in place, to determine if the feature is a bed, a unit contact, a vein, etc.) However, investigations of the relationship between the measurements, maps, and interpretations built from rover-based and orbitally-based measurements are limited; quantitative comparison of orbitally-based plane-fits with

those measured on a rover 3D dataset has been performed at only a single site (Stein et al., 2020).

Stack et. al (2016) found that regions expressed as light-toned or bright and fractured or striated/banded terrain in orbital views at three sites along the Curiosity rover's traverse in Gale Crater were reliably confirmed to be bedrock in rover views. These bedrock exposures may also form scarps which shed boulders (Stack et al., 2016). Terrains that were dark-toned and smooth or featureless in orbital expression were linked to surficial aeolian-transported sand cover (Stack et al., 2016). Stack et al. (2016) found that, between these two end-member cases, orbital mapping is limited in its ability to reliably differentiate bedrock from surficial or mantling deposits such as float and aeolian sand. Stack et al. (2016) also suggested that orbital facies mapping alone is likely insufficient to identify depositional processes and associated paleoenvironments. In the case of Jezero crater, Goudge et al. (2017) leveraged the additional tool of topographic measurements on a HiRISE DEM and a plane-fitting algorithm to make interpretations of the Western fan's architecture and thus paleoenvironment. Subhorizontal layers were classified as prodelta bottomsets and inclined layers were categorized as delta front foresets (Goudge et al., 2017). Based on the interpreted internal geometry of the deposit, the authors also made inferences about the grain size of the deposit (silt to sand), sediment transport processes (primarily settling out of suspension), and the depth of the receiving basin with relation to the inlet channel (a lake that is deep compared to the inflow). While the specific region measured by Goudge et al. (2017) from orbit was not visited by rover, explorations conducted by Perseverance on portions of the fan stratigraphy

inferred to be analogous were not consistent with the inferences of Goudge et al. (2017). They revealed coarse-grained (cobble and boulder conglomerate) beds steeper than the orbital measurements predicted (Mangold et al., 2021; Tate et al., 2023; Kanine et al., 2024), arranged in small (relative to the Western fan) discrete lobate forms (Mangold et al., 2024) instead of broad foresets spanning the scale of the fan, consistent with deposition via gravity-driven mass movements into a shallow basin (Mangold et al., 2021; Caravaca et al., 2024). These differences motivated us to interrogate the accuracy and completeness of geological information that may gained from orbital studies of stratal geometries. As initial ground-truthing of the HiRISE-derived plane fits show them to be accurate (Stein et al., 2020), we here expand the orbital-rover comparison and investigate whether further refinement of the selection and/or subsequent interpretation of orbitally-based measurements might allow for more reliable paleoenvironmental interpretations.

Additionally, while apparent dip in rover images has been used to make inferences about depositional processes (e.g., Mangold et al., 2021) and bed orientations may be constrained by eye (e.g., Grotzinger et al., 2015), a standardized workflow to calculate numerically true dips from apparent dips – particularly for targets of interest that have not been sufficiently imaged to construct a SfM digital outcrop model yet are too distant for image stereo pairs with small baselines to provide accurate digital models – has yet to be popularized in the planetary geology community.

Our objectives in this study are thus threefold: 1) Quantitatively compare orientations of nominally planar surfaces in Jezero crater obtained via orbitally-based

plane-fitting and via orientation constraints derived from Perseverance rover images, 2) determine if the nature of a surface (i.e., a bedding plane, a stratigraphic bounding surface, an erosional surface, etc.) can be accurately and reliably determined from orbit (via visible wavelength orthomosaics and DEMs) by ground-truthing with rover images, and 3) develop a simple and reproducible workflow for calculating plausible true surface orientations from measured apparent dip angles and look directions that may be applied to photographs of martian or terrestrial settings.

In this paper, we first describe the datasets used and the workflow in *Section 2*; we then apply the process of constraining true surface orientation to four localities in Jezero crater and describe the surface types in *Section 3*. *Section 4* discusses our findings on the accuracy and utility of orbitally-based plane fitting and methodological recommendations for the field of planetary geology.

2 Methods

2.1 Feature tracing and orientation calculation using HiRISE (orbital) datasets

The orbital datasets were viewed and the tracing performed in the open-source software QGIS. Traces of features of interest were digitized using the "Profile Tool" plug-in on a ~25 cm/pixel mosaic of HiRISE (High Resolution Imaging Science Experiment) visible-wavelength images (Fergason et al., 2020) with grayscale ranges stretched to enhance visual contrast. Cartesian *x*-*y*-*z* coordinates were then extracted from a co-registered digital elevation model mosaic with ~ 1

m/pixel vertical resolution derived from HiRISE stereopair images (Fergason et al., 2020).

We traced features (the smallest being ~9 m or 36 pixels) that could plausibly satisfy the criteria implicit in the Goudge et al. (2017) mapping of sedimentary layers, i.e., by characteristics that distinguish the feature from the surrounding terrain such as tone, texture, scarps/slope breaks, differential erosion, curvilinear planview geometry, and selected features with lateral extents of at least tens of HiRISE pixels to ensure adequate data for plane fitting. Each trace was grouped into one of three categories: 1) high quality (green), where the feature has lateral variation in both the *x* and *y* spatial dimensions (i.e., is not a straight line, which is conducive to a well-constrained plane fit) *and* can also be traced with high confidence (e.g., is different in tone from surrounding rock, is not interrupted by regolith, and appears to have a low degree of fracturing); 2) intermediate quality (orange), in which the feature either exhibits lateral variability in both *x* and *y or* can be traced with high confidence, but not both; or 3) low quality (red), where the feature is identifiable from orbit but is relatively straight in planview *and* is challenging to distinguish from surrounding terrain, highly fractured or "crumbly," partially covered by regolith, etc.

We selected for further investigation four localities that contain high-quality HiRISE traces that were also imaged by the Perseverance rover from multiple angles (Figure 1). The *x*-*y*-*z* coordinates of the traces in these localities were then fed into the *Attitude* module in Python (Quinn and Ehlmann, 2019b), which uses principal component analysis (PCA) to find the equation of the plane which minimizes variance in the third principal component (orthogonal to the nominal plane). This

calculation returns the best-fit dip angle, dip azimuth, and strike, as well as reporting angular errors (accounting for 3s of the variance in the coordinates), rake (the angle separating the strike of the nominal plane and the direction of greatest angular error), eigenvalues, and percent of variance contained within each principal component. The solution spaces for the fitted planes were then plotted as ellipses in dip angle - dip azimuth space.

2.3 Feature tracing and orientation calculation using rover (in-situ) datasets

For "green" HiRISE traces that are also the subject of at least two rover images with a difference in viewing direction >10˚, the surface traced from orbit was identified in rover images by referencing to visible features (boulders, tonal differences, scarp promontories, dunes) and topographic/elevation trends. Rover-based orientation analysis used Mast Camera Zoom (Mastcam-Z) (Bell et al., 2021) lossless enhanced color images. The Mastcam-Z camera has a 110 mm focal length at maximum zoom and an instantaneous field of view (IFOV) of 67.4 μrad/pixel (Bell et al., 2021). These images were generated with gridlines aligned to the Octavia E. Butler landing site frame. Higher-resolution SuperCam remote micro-imager (RMI) (Maurice et al., 2021) images (20 μrad/pixel IFOV) were used where available in concert with Mastcam-Z coverage to study fine-scale outcrop sedimentology. SuperCam images were manually adjusted to balance contrast, lighting, and feature visibility.

Absent the ability to make field measurements directly on the outcrop itself, we note the look azimuth (az_{look}) to the feature of interest on the Mastcam-Z

image and record the inclination or apparent dip angle, q_{app}, of a line fit to the surface of interest by eye (Figure 2). This method of fitting is meant to replicate the field method of measuring dip by sighting from afar via the clinometer on a Brunton compass. We assign an uncertainty s_{app} between ±0.5˚ and ±6˚ to the dip angle value depending on our ability to confidently fit a line to the surface of interest by eye. The error introduced by uncertainty in the look azimuth is assumed to be negligible. We also record the apparent dip direction, az_{app}, which, for a given image, will be to the viewer's left or right, or the semicircle from az_{look} to 180˚ counterclockwise or clockwise, respectively (Figure 2). We therefore generate three independent measurements (az_{look}, q_{app}, and az_{app}) of the surface per image.

These measurement triads, collected from at least two images with different viewing angles, are used to place semi-quantitative constraints on the true dip angle q_t and true azimuth az_t. The true dip cannot be less than an apparent dip, so we set the maximum observed q_{app} for a given site as a lower bound for q_t. Then, az_t must fall within the overlap of az_{app} hemispheres. These constraints are presented as a shaded field on each of the azimuth-dip diagrams.

Next, conceptualizing the true bed orientation as a vector with magnitude of the dip angle and direction of the dip azimuth, the observed apparent dip may be approximated as:

$$\theta_{app} = \theta_t \sin\phi \qquad \text{Eq. 1}$$

where q_t is the true dip angle, and f is the difference between the true dip azimuth, az_t, and az_{look}. Given two measurements of q_{app} and az_{look} (e.g., q_{app_a} and az_{look_a} derived from an image taken on *sol a,* and q_{app_b} and az_{look_b} from an image taken on *sol b*) one may find solutions for *true* dip angle and azimuth. We first re-write Eq. 1 for each sol's measurements, substituting (az_{look} - az_t) for f, and rearrange to yield Eqs. 2 and 3:

$$\theta_t = \frac{\theta_{app_a}}{sin(az_{look_a} - az_t)} \quad \text{Eq. 2}$$

$$\theta_t = \frac{\theta_{app_b}}{sin\left(az_{look_b} - az_t\right)} \quad \text{Eq. 3}$$

We here also account for az_{app}. Sign convention requires that az_{look} be reported such that az_{app} is to the viewer's left. Equivalently, we might state that the difference between az_{look} and az_t must be measured in the counterclockwise direction. In cases where az_{app} is to the right, we substitute the case where one is looking in the opposite direction and observing the same surface dipping to the left. For example, for a surface with an az_{app} to the right when looking due North (az_{look} = 0˚), the observed az_{app} when looking due South (az_{look} = 180˚) will be to the left. This latter look direction is used.

Next, For a physically real, planar surface with $\theta_t \in \mathbb{R}$,

$$\frac{\theta_{app_a}}{sin(az_{look_a} - az_t)} \stackrel{!}{=} \frac{\theta_{app_b}}{sin\left(az_{look_b} - az_t\right)} \quad \text{Eq. 4}$$

or, equivalently,

$$\frac{\theta_{app_a}}{sin(az_{look_a} - az_t)} - \frac{\theta_{app_b}}{sin(az_{look_b} - az_t)} = \Delta_{ab} \stackrel{!}{=} 0 \quad \text{Eq. 5}$$

In other words, for a planar surface, the correct q_t will be equivalent for Eq. 2 or Eq. 3, such that Eq. 4 and Eq. 5 are true. We numerically solve for the value of az_t that yields Δ_{ab} closest to our desired solution of 0 in Eq. 5 using the "Goal Seek" algorithm in Excel to perform an iterative search for az_t. The calculated value of az_t may then be plugged into Eq. 2 or Eq. 3 to find q_t.

To explore possible values of q_t and az_t given uncertainty s_{app} in the apparent dip measurements, we conduct a Monte Carlo simulation by generating a Gaussian distribution of 1,000 new q_{app} values for each initial q_{app} measurement q_{app_0}, such that the mean of each distribution is equal to q_{app_0} and the standard deviation equals the uncertainty assigned to the dip angle measurement (s_{app}). We solve for az_t as described above for each of the 1,000 pairs of trial q_{app_a} and q_{app_b} values. The Goal Seek algorithm occasionally locates local minima rather than the global minimum and cannot cross asymptotes, where $\Delta_{ab} \rightarrow \infty$. For such cases, one may plot the error with respect to azimuth, find locations (if any) where the error reaches zero, and seed the algorithm with a starting point azimuth from one side of the asymptote(s) and then the other. In persistently non-convergent trials (after manual aid to cross asymptotes), the "problematic" trial is replaced with values from a new Gaussian distribution, and the process is repeated. The unique solutions for q_t and az_t for each trace are then plotted in dip angle - dip azimuth space. We record the mean, standard

deviation, minimum, and maximum values from these solutions of true orientation for each image pairing (e.g., *sol a - sol b*) available for a given locality. These calculations are modified for cardinal directions: the "mean" azimuth for a given locality is perhaps better conceptualized as the "center of mass" of the multiple image pair solution point clouds, in which the mean azimuth value is obtained by averaging the *x* and *y* components for every orientation solution in the locality. Similarly, finding the standard deviation for azimuth requires finding the angular difference between each nominal solution and the mean azimuth, keeping in mind that cardinal directions "start over" at 0˚ N; for example, a solution with an azimuth of 355˚ is 10˚ away from a mean azimuth of 5˚, not 355˚ - 5˚ = 350˚.

3 Results

In all, we identify four localities containing a total of five traced surfaces across the Jezero Western fan for remote sensing vs. *in-situ* analysis. In the text, a shorthand is used to refer to the "green" HiRISE-rover paired traces, consisting of an abbreviation of the locality name (Cape Nukshak = cn, Whale Mountain = wm, Franklin Cliffs = fc, Pinestand Mountain = pm), the letter *r* for rover and *H* for HiRISE, and the trace label in subscript. E.g., the Cape Nukshak rover a – HiRISE 4 trace pair is shortened to $cn\_r_a\text{-}H_4$. Our findings are summarized in Table 1.

3.1 Cape Nukshak

Cape Nukshak is a plateau that rises above the surrounding crater floor just basinward of the cliffs of the Western fan scarp (Figure 1, Figure 3). The plateau has an arcuate front defined by an abrupt scarp. Some subtly arcuate light-toned deposits that terminate abruptly at the plateau edge are visible atop Cape Nukshak from orbit. These features are reminiscent of the previously-mapped curvilinear unit (Stack et al., 2020) and are possibly the erosional remnants of said unit. Light-toned deformed layered deposits also appear below and above the plateau, mapped as "delta thinly-layered" (Stack et al., 2020). The "green" HiRISE-rover paired trace for this site *cn_r$_a$-H$_4$* is located at the margin of the plateau (Figure 3), where there is a prominent break in slope that the approach of previous works (e.g., Goudge et al., 2017) may have attributed to a bedding plane. The traced portion of the plateau edge roughly follows HiRISE DEM-derived contour lines, so we infer from orbit the surface is approximately horizontal.

Rover views of Cape Nukshak look at the scarp of the plateau edge-on (Figure 3c-f). The *in-situ* view of *cn_r$_a$-H$_4$* shows the top of the scarp appears subhorizontal, with $\theta_{app,\ max}$ of 2.5˚. $\theta_{app} \approx 0$˚ for sols 686 and 415 indicate the surface is dipping toward or away from the viewer along the line of sight, or likely WNW or ESE. Assuming the imaged portions are representative of the entire plateau, the top of the plateau dips between 327˚ (NW) clockwise to 140˚ (SE) (Figure 4). Most of the HiRISE solution ellipse falls within these constraints on dip angle and azimuth, with the best fit plane for the HiRISE trace having a dip angle of 2.65˚ toward 101˚ (ESE),

indeed in between sol 686 and sol 415 lines of sight. Monte Carlo solutions are similarly clustered close to these lines of sight, with the average of the Monte Carlo solutions (calculated by averaging the *x* components and the *y* components of all of the Monte Carlo solutions) located at 116˚ azimuth and 4.40˚ dip.

Though the break in slope at the margin of Cape Nukshak is continuous, rock outcroppings themselves are frequently interrupted by meters of regolith. Outcroppings of subhorizontal to low-angled and parallel to subparallel beds (Figure 5a) inferred to be sandstone (given resolution constraints) are interspersed with, or perhaps interrupted and scoured by, lenses of massive pebble conglomerate (Figure 5a). These lenses appear to correlate to subtle scallop-shaped recessions of the plateau scarp in planview. Also on the plateau edge, just outside of the trace, are pebbly sandstones arranged in tangentially-inclined or "swoop"-shaped beds interpreted as potential scour-and-fill structures, as well as planar crossbedding (Figure 5b). This lithology is also possibly sampled by the trace. In summary, while the trace tracks a quasi-planar topographic feature within the landscape, the break in slope at the top of Cape Nukshak cannot be tied to a single bed, a consistent lithology, or a stratigraphic package with fully internally-consistent bed behavior.

3.2 Whale Mountain

Overlying Cape Nukshak at the terminus of a lobate-shaped promontory of the fan (Figure 1, Figure 6), is the portion of the Western fan scarp known as Whale Mountain. The top of this promontory is covered in ridges of boulders visible on HiRISE, with many boulders appearing to have rolled downslope onto the top of

Cape Nukshak Plateau and the surrounding crater floor. The margins of the top of Whale Mountain are characterized by abrupt breaks in slope that overlie steep sides. In places rocky outcrops jut out from the face of this scarp. Both the margins and the rocky outcrops have a "rubbly" or "blocky" expression, creating edges that are highly rugose in planview, more so than is the case for Cape Nukshak. Trace *wm_r$_b$-H$_5$* is located at the break in slope at the top of Whale Mountain, and appears to roughly follow contour lines, indicating a horizontal to low-angle surface (Figure 6). Trace *wm_r$_a$-H$_4$* samples an outcrop that appears inclined, crossing contour lines (Figure 6).

Rover images of the Western Fan scarp at Whale Mountain (Figure 6c-e) reveal a package of concave-down strata in cross-section, along with isolated exposures of inclined beds amidst regolith cover, one of which is the Mars 2020 mission target "Mount Juhle," traced as *wm_r$_a$-H$_4$*. Examination of this trace from multiple perspectives constrains the surface as dipping between 91˚ (E) and (clockwise to) 255˚ (SW), with a dip of at least 17˚ inclination (Figure 7). The HiRISE solution ellipse falls almost entirely within these constraints with best fit azimuth 142˚ and best fit dip angle is 20.0˚. The average of the Monte Carlo distribution is at 25.7˚ dip and 116˚ azimuth.

The break in slope at the top of the promontory traced as *wm_r$_b$-H$_5$* exposes packages of primarily subhorizontal beds and boulder-bearing deposits, with target name "American Creek." Apparent dips of the planar break in slope at the top of the promontory constrain the azimuth to between 338˚ (NNW) and 87˚ (E) (i.e., roughly the NE quadrant) and at least 2.5˚ (Figure 8). The surface is close to

horizontal in the sol 459 view, indicating a dip direction closely aligned with this line of sight (87˚). Nearly the entire HiRISE solution ellipse falls within the *in-situ* constraints, with best fit azimuth 81.5˚ (close to the sol 459 line of sight) and dip angle 3.75˚. The average of the Monte Carlo simulations is 4.03˚ dip at 76.3˚ azimuth, falling within the HiRISE solution ellipse.

Mastcam-Z and SuperCam images obtained at close range to the outcrops allow for description of the sedimentology and stratigraphy of these outcrops at fine scale. The top of the inclined package traced as wm_r_a-H_4 consists of thinly-bedded, roughly parallel planar strata that protrude from the hillslope (Figure 9). Pebbles are present, and we infer the matrix is sandstone (with grains below the imaging resolution). Below the pebbly sandstone are pebble conglomerates expressed as poorly-bedded to massive deposits as well as arranged in thicker, deformed beds dipping at higher angles. These lithologies do not appear to have been sampled in the trace. Therefore, although wm_r_a-H_4 does not record a single bed, it does appear to record a single lithology: the topographic expression of the exposure, recorded in the *x*-*y*-*z* coordinates of the trace, seem to reflect the relatively consistent bedding orientations within the stratigraphic package of pebbly sandstone.

The trace wm_r_b-H_5 follows the margin of positive-relief outcroppings of rock as viewed from above. This translates to the elevation of the most erosion-resistant strata (those with the greatest projection from the hillslope) being extracted, or, in cases of no notable differential erosion in a vertical section, the uppermost package of rock being sampled. The effect is a slightly stepwise form of the trace when viewed in vertical cross-section. In addition, the stratigraphic

bounding surfaces dividing lithologies occur at higher angle than the topographic surface comprising the top of Whale Mountain, meaning the lithology of the uppermost erosion-resistant package of rock varies laterally. These two points lead to *wm_r$_b$-H$_5$* sampling multiple lithologies. To the south (left in Figure 6c-e), the trace is over thickly-bedded pebble-to-cobble conglomerate (Figure 9b), which appears to comprise a capping unit, and possibly samples the underlying more thinly-bedded (apparently) subhorizontal pebble conglomerate as well (Figure 9b). To the north (right in Figure 6c-e), the trace may sample low-to-moderate angle thickly-bedded, poorly-sorted pebble-to-boulder conglomerate interbedded with a more erosion-resistant thinner and finer pebble conglomerate (Figure 9b) in addition to the capping conglomerate. A lensoid deposit of clast-supported boulder conglomerate and deformed pebble conglomerate (Figure 9b) pinches out laterally and is not sampled.

It is unclear if the topographic break in slope is controlled by an exhumation process that planed off strata, the deposition of a capping unit, or the highest-elevation instance of relatively competent strata (such as the pebble conglomerate that appears in positive relief in the thinly-bedded package and the fine interbeds) – elevations which too may be locally limited by the erosive base of an overlying deposit. Additionally, while the strata sampled by the trace may be grouped as gravel conglomerates, at finer level of detail the facies vary across the break in slope, and we do not identify a single bed that is continuous across the outcrop. It is also important to note that neither trace captures the complex stratal structure that comprises much of the Whale Mountain locality: the meters-high steeply-inclined

beds arranged in a concave-down form (best viewed in Figure 6e) that is not visible from orbit due to exposure geometry.

3.3 Franklin Cliffs

Also on the Western fan scarp, Franklin Cliffs rise even higher than Whale Mountain (Figure 1). From orbit, this region resembles an isthmus, with well-defined breaks in slope near the top of the "isthmus" surrounding the deposit on three sides (Figure 1). One such break in slope, which roughly follows contour lines, is traced as fc_r_a-H_1. Light-toned curvilinear sets, inferred to be continuous with the curvilinear unit (Stack et al., 2020), cross the top of Franklin Cliffs, and to the south, below the break in slope, are inclined (contour-crossing) rock scarps.

On the ground, we can see that Franklin Cliffs consists of a package of subhorizontal to low-angle strata at its top which sharply truncate underlying steeply-inclined beds (Figure 10). This upper package is the rock sampled by fc_r_a-H_1. From this perspective, we see that the topographic break in slope is irregular: while some of the surface is subhorizontal in all images (left of dotted line, Figure 10d-f), in other places it appears inclined (right of dotted line, Figure 10d-f). This inclined portion has $\theta_{app,\ max}$ and thus a lower bound of true dip of 15˚, though we cannot rule out some degree of foreshortening that makes this angle appear artificially steep. Constraints from apparent dip set the true azimuth as between 69˚ (NE) and 200˚ (SW) (Figure 11). As the surface is not actually planar, we would expect the fit using DEM-extracted coordinates to have comparatively large errors. This turns out to be the case. Much of the HiRISE solution ellipse falls within the

azimuth constraints (Figure 11), with a mean azimuth of 233˚. However, HiRISE plane fits have a dip less than $\theta_{app,\,\max}$, with a best fit dip angle of 0.398˚ and 3 standard deviations of the trace variance accounted for with a plane dipping ~14˚ or less. The average of the Monte Carlo simulations is 14.6˚ dip at 178˚ azimuth.

The strata capping Franklin Cliffs exhibit a relatively mature textural hierarchy, with typically subhorizontal to low-angle stratigraphic boundaries separating sedimentary sequences (Figure 12). Lithologies plausibly sampled by *fc_*r_a*-*H_1 include finely-bedded parallel planar pebbly sandstone, boulder conglomerate with an irregular base, and subparallel planar pebble-to-cobble conglomerates (Figure 12). The behavior of the scarp as a whole may be linked to the orientation of the stratigraphic boundaries or the beds within them; as both are low-angle, we cannot distinguish between these scenarios. However, we can definitively state that along the course of the trace, individual beds are erosionally truncated (Figure 12), and the trace does not exclusively follow any one sequence or lithology contained within the larger capping package.

3.4 Pinestand Mountain

Pinestand Mountain is a butte on top of the Western fan (Figure 1), appearing from orbit as part of the curvilinear unit (Stack et al., 2020). Thin, gently curved, light-toned lineations that cross contours are abundant in this locality, one of which is traced as *pm_*r_a*-*H_1 (Figure 13).

Rover images reveal the butte is composed almost entirely of steeply-inclined strata (Figure 13). These beds are not angular, but rather tangentially decrease in dip

angle toward their bases. The traced bed ranges in apparent dip angle from 38˚ (at its top) to 12˚ (at its base). A more typical dip angle occurs near the middle of the bed's elevation range, between ~20˚ - ~30˚. We use the value of 26.5˚, as observed in sol 729, as a reasonable lower bound for an expected planar fit through this surface (Figure 14), though this value should be considered approximate. The true azimuth is constrained as between 76˚ (ENE) and 239˚ (SW). The HiRISE solution ellipse falls entirely within these constraints with a best fit of 35.6˚ dip angle at 153˚ azimuth (Figure 14), with the caveat that this fit is a planar approximation of a non-planar surface. Monte Carlo solutions have an average dip of 26.2˚ and azimuth of 136˚.

This trace is unique across our studied localities in that it appears that it does track a single, continuous bed. This pebble conglomerate (Figure 13d inset) reaches nearly a meter thick at maximum and thins upward along the outcrop. While dusty or fractured portions are light-toned, it appears the fresher exposed surfaces are dark gray, though still lighter in color than the surrounding regolith.

4 Discussion: quality and significance of orbital-based plane fits

4.1 Plane fit quality is high

Based on in-situ constraints of dip angle and dip azimuth, HiRISE-based plane fitting provides an accurate representation of the reality on the ground, in terms of capturing the orientation of planar (or quasi-planar) features such as beds and scarps. Of the five traces analyzed, four have overlap between the broad *in-situ* constraints (green shaded regions) and the HiRISE plane-fitting solutions for both az_t and θ_t; for the non-overlapping case, (fc_r_a-H_1), the surface being tracked was

uneven, such that the orbital plane fit may be more representative of one portion of the trace (the flatter part) than the other. There was overlap between the Monte Carlo simulations and the broad *in-situ* constraints in all cases, and overlap between the Monte Carlo simulations and HiRISE fits in four of five cases.

Additionally, it is important to note that some of the *in-situ* constraints derived from apparent dip directions in Mastcam-Z images allow a wide range of azimuths as potential solutions; the ability to confine possible solutions via apparent dip directions alone to a meaningfully small portion of the compass will vary case-by-case with the availability of images that provide multiple perspectives with significant separation in look direction angles. Therefore, in cases where the average of rover-based Monte Carlo simulations and HiRISE fits indicate different orientations that both fall within the broad apparent dip angle and azimuth constraints, we cannot say whether one or the other is closer to reality.

4.2 Planes are not beds: Implications for mapping and paleoenvironmental interpretations

First, topographic features such as breaks in slope or scarps are often visible as linear features from orbit. They reliably produce quantitative orientations. But such topographic features are related to deposit properties only in a relative sense, in that more cohesive materials are more likely to outcrop in positive relief. Sometimes, these will be beds. More often in our Jezero data, such traced features are packages or sets of beds. The beds that record the details of the flow conditions are at smaller (meters to decimeters) scale, and this is not discernible from orbit. This is consistent

with the findings of Stack et al. (2016) in Gale crater that the boundary between resistant and scarp-forming orbital facies and the surrounding terrain can correlate either to contact of bedrock and unconsolidated surficial deposits, or the contact between lithologies. In addition, we find that while some distinct packages of strata jut out from the surrounding regolith-covered hillslopes (e.g. at Whale Mountain), tying topographic expression to rock physical properties, continuous breaks in slope are also observed to cross multiple in-place lithologies (e.g., Cape Nukshak), indicating independence of topography and lithology. While most of the strata sampled by the five studied traces are gravel-bearing (pebbly sandstones to cobble conglomerates), this trend may result from the ubiquity of gravels in martian fluvial deposits (Braat et al., 2024), rather than being indicative of a unique ability of gravelly sediment to form erosion-resistant ledges. Hence, this study does not prove that a scarp visible from orbit is more likely to be a gravel-bearing sedimentary rock in greater proportion than the population of deposits on Mars that are gravelly sedimentary rocks.

Secondly, *deposit topography need not clearly follow any particular stratigraphic or structural element* (such as bedding planes or sequence boundaries). Sometimes it follows packages. We encounter some evidence for a relationship between the topography and the within-sequence bed orientation of the dominant lithology (i.e., *cn_r$_a$-H$_4$*, *wm_r$_a$-H$_4$*), and this relationship may be even stronger for inclined surfaces (*wm_r$_a$-H$_4$*, *pm_r$_a$-H$_1$*). Therefore, it might be reasonable (though not foolproof) given the appropriate geologic context to interpret the orientation of a light-toned linear feature as reflective of its internal structure. However, it is difficult

to ascertain what is a single bed (*pm_r_a-H_1*) and what is a sedimentary package or sequence of related beds (e.g., *fc_H_4*). While the layers traced in Goudge et al. (2017) are assumed to each "represent a discrete bedding plane exposure," our investigation of similar features demonstrate *not all layer-like features traced from orbit are beds.* It follows that the geometric disposition of topographic features does not allow for clear extrapolation to internal deposit structure (and subsequently to depositional process or environment). Whether a particular feature is a bed or a package of beds has implications for deposit scale and may be relevant for the evaluation or development of some hypotheses. Therefore, we recommend a move toward language that more accurately conveys the level of certainty about the feature in question by separating description (e.g., linear feature with topographic signature and distinct tone) from interpretation (e.g., the distinct depositional and stratigraphic unit of "bed"). This move also has the benefit of enabling clearer communication across fields of study, such as between Earth-focused sedimentologists and sequence stratigraphers and planetary geologists.

Lastly, even if a bed, *the traced surface may have a starkly different orientation than underlying or overlying strata*. This fact may be obvious to the field geologist accustomed to seeing road cuts and other cross-sectional views of deposits but is perhaps more difficult to grasp intuitively for the remote sensing specialist who typically views terrain in planview. It is not safe to assume that because two outcrops (which may be recorded as topographic surfaces in 3D data), separated only by several meters, have similar stratal characteristics, that the intervening strata between them share the behavior. An example of this phenomenon is the low-angle surface of

Cape Nukshak Plateau and the subhorizontal top of the promontory of Whale Mountain a few meters above. Both contain low-angle to subhorizontal planar beds yet they bracket the steeply-inclined beds of Whale Mountain (Figure 6) in between. A similar architectural succession (low-angle beds, steeply-inclined beds, low-angle beds) is seen at Franklin Cliffs (Figure 8).

In summary, orientations of surfaces calculated from traces performed on HiRISE datasets are generally shown to be true to on-the-ground observations, albeit for a small sample size. The accuracy of orbitally-derived plane fits is relevant for landing site selection and/or hazard mapping for planned rover traverses. Additionally, in-place strata can be identified with reasonable fidelity for light-toned linear bands. Those at moderate-to-steep inclinations were shown to be reflective of original depositional geometries. This confirmation is relevant for identifying in-place deposits as science targets for rover investigation. However, the control(s) of the topography or 3D expression of a given feature, or the "type" of surface (bed, self-similar package of beds, or erosional surface) traced for plane-fitting, will be uncertain. While there may be some dependence of scarp orientation upon internal deposit structure, we find the confident identification of a particular grain size, lithology, or stratigraphic element is not supported by orbital data alone. This conclusion extends the findings of previous mapping studies with additional 3D analyses and generalizes them beyond a specific site (Stack et al., 2016). We suggest that while broad determinations of depositional environment (e.g., a fluvio-lacustrine system) may be made by virtue of identification of meso- to macro-scale landforms (e.g., in the case of Jezero, inlet valleys, a depositional fan, and an outlet channel),

the reconstruction of the particulars of localized depositional processes, such as sediment transport mechanisms, or internal landform structures using (currently available) orbital data alone verges on speculation. Orbital data, even that which is relatively high-resolution, is best suited to construct environmental narratives at coarser levels of description that do not require knowledge of internal deposit structure or texture. These studies may then produce testable hypotheses and important guidance that can drive finer-scale exploration with rovers, landers, helicopters, or other spacecraft that can provide higher-resolution observations from an *in-situ* perspective.

5 Conclusions

Though previous studies have used 3D outcrop geometry to interpret deposit architecture, depositional processes, and paleoenvironment (Goudge et al., 2017), other works have suggested, based on rover-orbital facies mapping comparisons, that making such interpretations from orbit is extremely challenging (Stack et al., 2016). Additionally, ground-truthing of orbitally-derived plane fits of the martian surface has been limited to a single site in Gale crater (Stein et al., 2020). We therefore focused on both extending the evaluation of the accuracy of orbitally-measured surface orientations to Jezero crater and investigating the controls of the topography of the traced layer-like features that, in similar exposures, have been interpreted as beds (Goudge et al., 2017). We developed a method for constraining the true surface orientation of a feature of interest from at least two rover images taken from different perspectives. This study offers the first confirmation of the accuracy of HiRISE-

derived plane fits of Jezero crater deposit exposures. However, while the modern topography of breaks in slope or scarps may be influenced by internal deposit characteristics such as bed orientations, there is no robust and reliable relationship between the layer-like topographic features particular and lithologies, grain sizes, or stratigraphic/architectural elements. Notably, even light-toned or inclined features traced on HiRISE should not be uniformly understood as individual beds. Rather, rover images show that the post-erosional topography cuts across rock lithologies, depositional sequences, and within-sequence beds. It is also the case that some structures may only be visible on the ground in cross-section. Therefore, a geologic narrative based on deposit architecture as measured exclusively from orbital data is likely incomplete. Nevertheless, this study does not contraindicate orbital-based descriptions of diagnostic landforms as paleoenvironmental indicators; such investigations likely still present valuable contributions to the understanding of past martian surface processes and the evolution of the planet's climate, as well as complementary tasks such as rover mission planning.

References

Banham, S. G., Gupta, S., Rubin, D. M., Watkins, J. A., Sumner, D. Y., Edgett, K. S., et al. (2018). Ancient Martian aeolian processes and palaeomorphology reconstructed from the Stimson formation on the lower slope of Aeolis Mons, Gale crater, Mars. *Sedimentology, 65*(4), 993–1042. https://doi.org/10.1111/sed.12469

Barnes, R. et al. (2018). Geological analysis of Martian rover-derived Digital Outcrop Models using the 3-D visualization tool, Planetary Robotics 3-D Viewer—Pro3D. *Earth and Space Science, 5*, 285– 307. doi: 10.1002/2018EA000374

Bell, J. F. et al. (2021). The Mars 2020 Perseverance rover Mast Camera Zoom (Mastcam-Z) multispectral, stereoscopic imaging investigation. *Space Science Reviews 217*(24). https://doi.org/10.1007/s11214-020-00755-x

Braat, L., Brückner, M. Z. M., Sefton-Nash, E., & Lamb, M. P. (2024). Gravity-driven differences in fluvial sediment transport on Mars and Earth. *Journal of Geophysical Research: Planets*, 129, e2023JE007788. https://doi.org/10.1029/2023JE007788

Fergason, R. L., Hare, T. M., Mayer, D. P., Galuszka, D. M., Redding, B. L., Smith, E. D., Shinaman, J. R., Cheng, Y., Otero, R. E., (2020). Mars 2020 terrain relative navigation flight product generation: Digital terrain model and orthorectified image mosaics. 51st Lunar and Planetary Science Conference, URL: https://www.hou.usra.edu/meetings/lpsc2020/pdf/2020.pdf.

Goudge, T.A., Milliken, R. E., Head, J.W., Mustard, J. F., Fassett, C. I. (2017). Sedimentological evidence for a deltaic origin of the western fan deposit in Jezero crater, Mars and implications for future exploration, *Earth and Planetary Science Letters*, *458*, p. 357-365. https://doi.org/10.1016/j.epsl.2016.10.056

Grotzinger, J. P. et al. (2015). Deposition, exhumation, and paleoclimate of an ancient lake deposit, Gale crater, Mars. *Science, 350*, aac7575. DOI:10.1126/science.aac7575

Hayden, A. T., & Lamb, M. P. (2020). Fluvial sinuous ridges of the Morrison Formation, USA: Meandering, scarp retreat, and implications for Mars. *Journal of Geophysical Research: Planets*, *125*, e2020JE006470. https://doi.org/10.1029/2020JE006470

Korus, J. T, Joeckel, R. M., and Tucker, S. T. (2020). Genesis of giant, bouldery bars in a Miocene gravel-bed river: Insights from outcrop sedimentology, UAS-

SfM photogrammetry, and GPR. *Journal of Sedimentary Research 90* (1): 27–47. https://doi.org/10.2110/jsr.2020.3

Mangold, N., Caravaca, G., Gupta, S., Williams, R. M. E., Dromart, G., Gasnault, O., et al. (2024). Architecture of fluvial and deltaic deposits exposed along the eastern edge of the western fan of Jezero crater, Mars. *Journal of Geophysical Research: Planets, 129*, e2023JE008204. https://doi.org/10.1029/2023JE008204

Maurice, S., Wiens, R.C., Bernardi, P. et al. (2021). The SuperCam instrument suite on the Mars 2020 rover: Science objectives and mast-unit description. *Space Science Reviews 217*, 47. https://doi.org/10.1007/s11214-021-00807-w

Okubo, C. H. (2010). Structural geology of Amazonian-aged layered sedimentary deposits in southwest Candor Chasma, Mars. *Icarus, 207*(1). https://doi.org/10.1016/j.icarus.2009.11.012

Quinn, D. P., & Ehlmann, B. L. (2019a). The deposition and alteration history of the northeast Syrtis Major layered sulfates. *Journal of Geophysical Research, Planets, 124*, 1743–1782. https://doi.org/10.1029/2018JE005706

Quinn, D. P., & Ehlmann, B. L. (2019b). A PCA-based framework for determining remotely sensed geological surface orientations and their statistical quality. *Earth and Space Science, 6*, 1378–1408. https://doi.org/10.1029/2018EA000416

Stack, K. M. et al. (2016). Comparing orbiter and rover image-based mapping of an ancient sedimentary environment, Aeolis Palus, Gale crater, Mars. *Icarus 280*, 3-21. https://doi.org/10.1016/j.icarus.2016.02.024

Stack, K.M., Williams, N.R., Calef, F. et al. (2020). Photogeologic map of the Perseverance rover field site in Jezero crater constructed by the Mars 2020 Science Team. *Space Science Reviews 216*, 127. https://doi.org/10.1007/s11214-020-00739-x

Stein, N. T., Quinn, D. P., Grotzinger, J. P., Fedo, C., Ehlmann, B. L., Stack, K. M., et al. (2020). Regional structural orientation of the Mount Sharp group revealed by in situ dip measurements and stratigraphic correlations on the Vera Rubin ridge. *Journal of Geophysical Research: Planets, 125*, e2019JE006298. https://doi.org/10.1029/2019JE006298

Figures

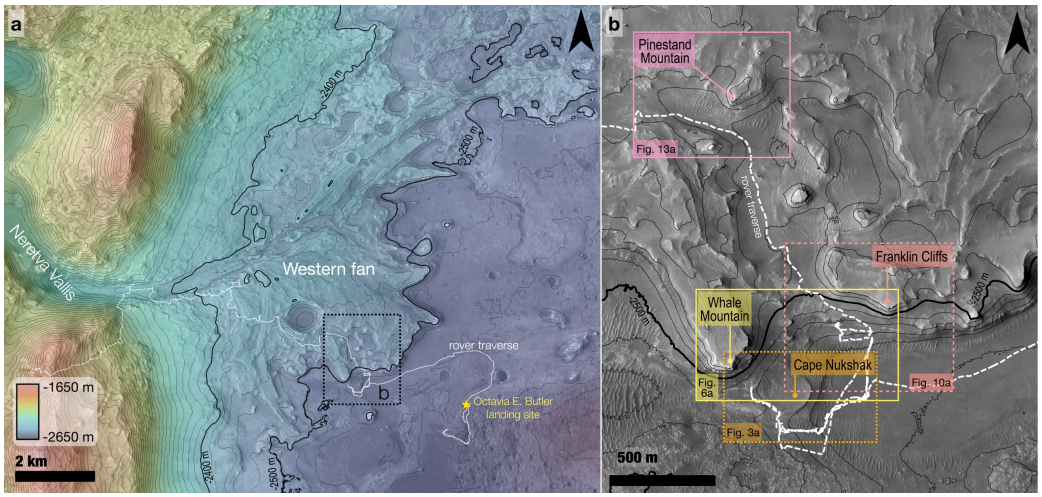

Figure 1: Context and study locations. Part **a**: regional overview of the Jezero crater Western fan. CTX DEM is partially transparent over a CTX mosaic. Contours are 20 m and derived from the CTX DEM. Included is the Perseverance rover Octavia E. Butler landing site and traverse from landing to sol 1431. Part **b** shows the HiRISE image PSP_002387_1985 with 10 m contours derived from the HiRISE DEM. Key localities of study and fields of view of subsequent figures are annotated.

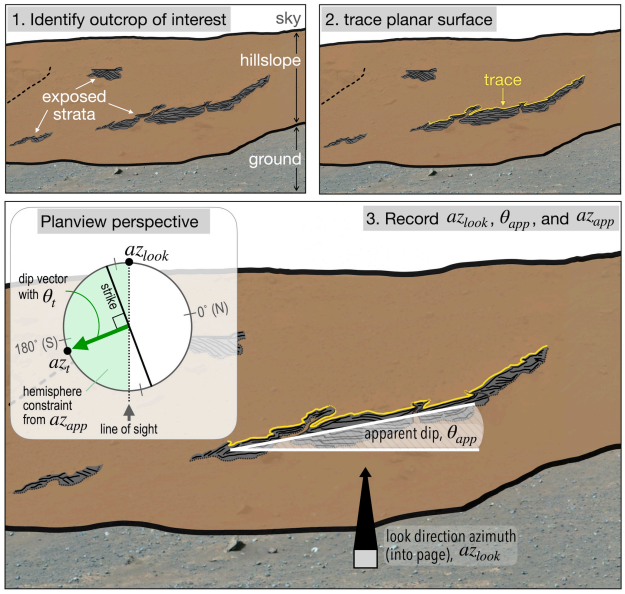

Figure 2: Methods demonstrated with annotations over a sol 411 on-the-ground view of the Whale Mountain locality. The surface traced from orbit is tracked in rover views via feature matching. Then, the image look direction, apparent dip angle, and apparent dip direction are recorded. Inset planview perspective diagram with cardinal directions is rotated to align with the view direction, with up being az_{look}. In this example, a single observation of az_{app} (to the left in this image) constrains the possible true dip azimuth as within the hemisphere from az_{look} to 180° counterclockwise from az_{look}. Diagram is intended to be illustrative, not to convey numerical values.

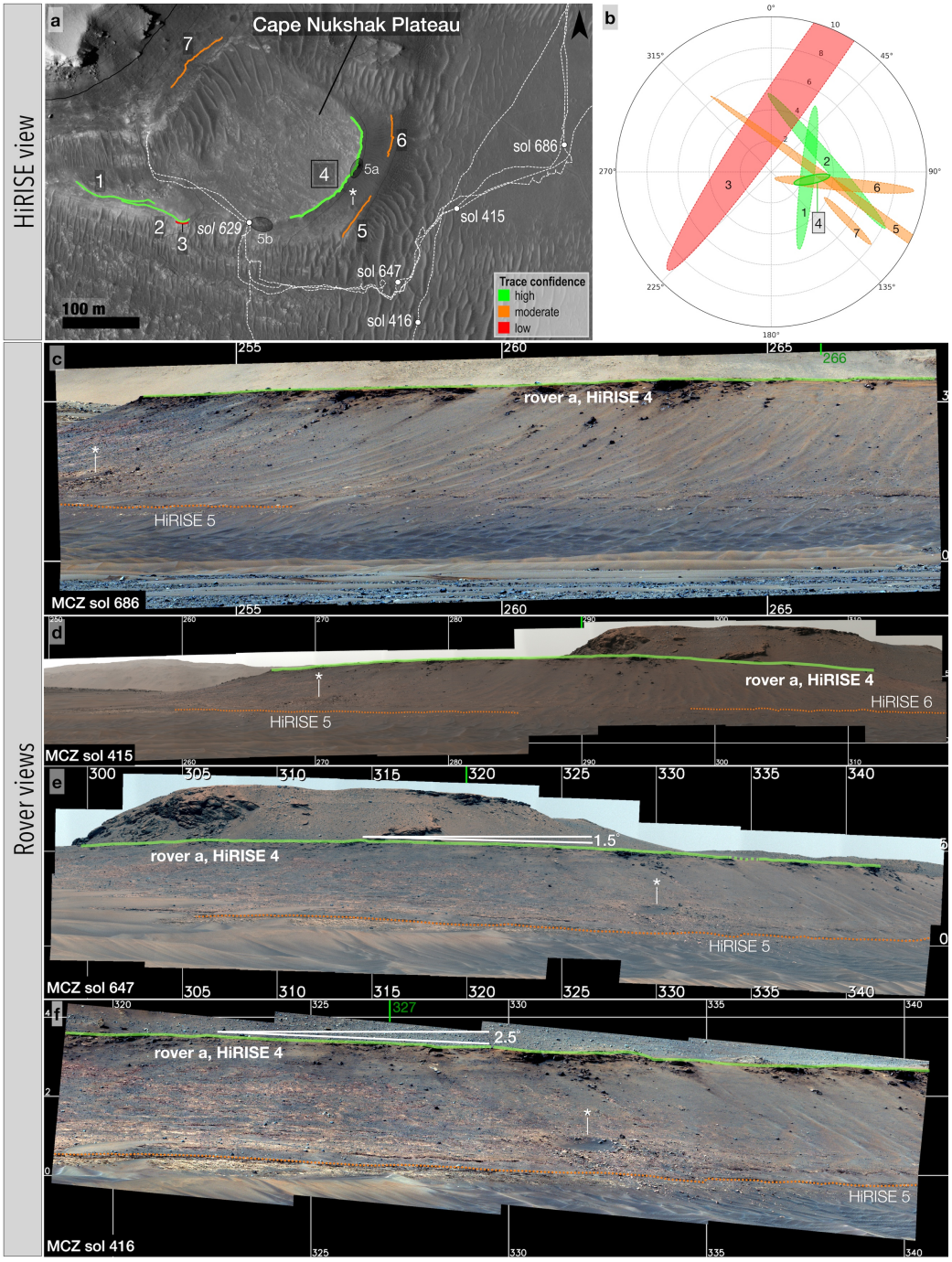

Figure 3: Orbital and rover views of Cape Nukshak Plateau. **a**: HiRISE traces and Mastcam-Z imaging locations. Locations of the outcrops shown in Figures 5a and 5b are shown in shaded ellipses. (Cont. next page.)

Figure 3 caption, continued: Sol 629 image of outcrop "Alagnak" was used for sedimentology analysis (Figure 5) but not surface orientation determination. Trace 4 (label boxed in part **a** and **b**) at the edge of the plateau is analyzed in rover images (parts **c-f**). A crater used for perspective orientation is labeled with an asterisk in parts **a** and **c-f**. Green tick marks note azimuths used in orientation estimates. Part **b** shows the solution ellipses in dip angle – dip azimuth space for the plane fits from HiRISE traces.

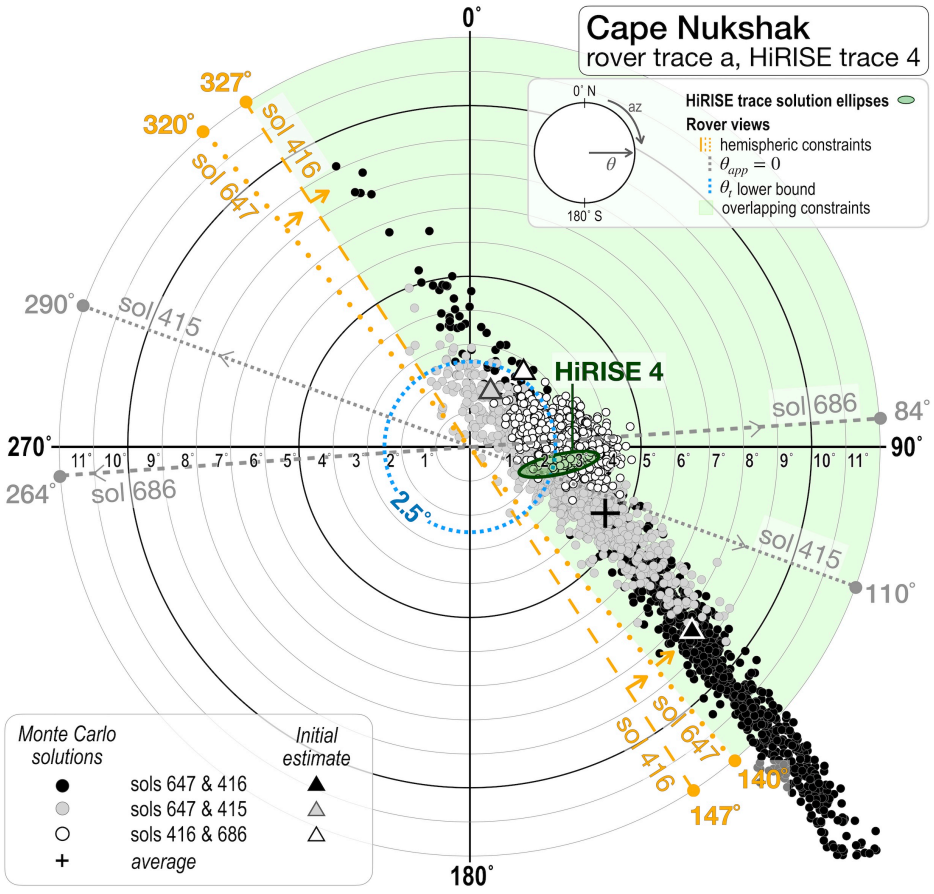

Figure 4: Rover-based orientation constraints (shaded light green) from az_{app} and $\theta_{app,\,max}$ (dotted blue line), rover-based Monte Carlo simulations (cloud of dots), and orbital-based HiRISE plane fits (shaded green ellipse) for Cape Nukshak. Triangles show the az_t and θ_t calculated from the initial estimates (θ_{app_0}) for each image pair. "+" marks the average of the Monte Carlo solutions. Orange lines (dashed or dotted) demarcate lines of sight for Mastcam-Z images in which the trace appears inclined, with orange arrows indicating the direction of az_{app}. Gray lines (dashed or dotted) show the line of sight for images in which the traced surface appears horizontal.

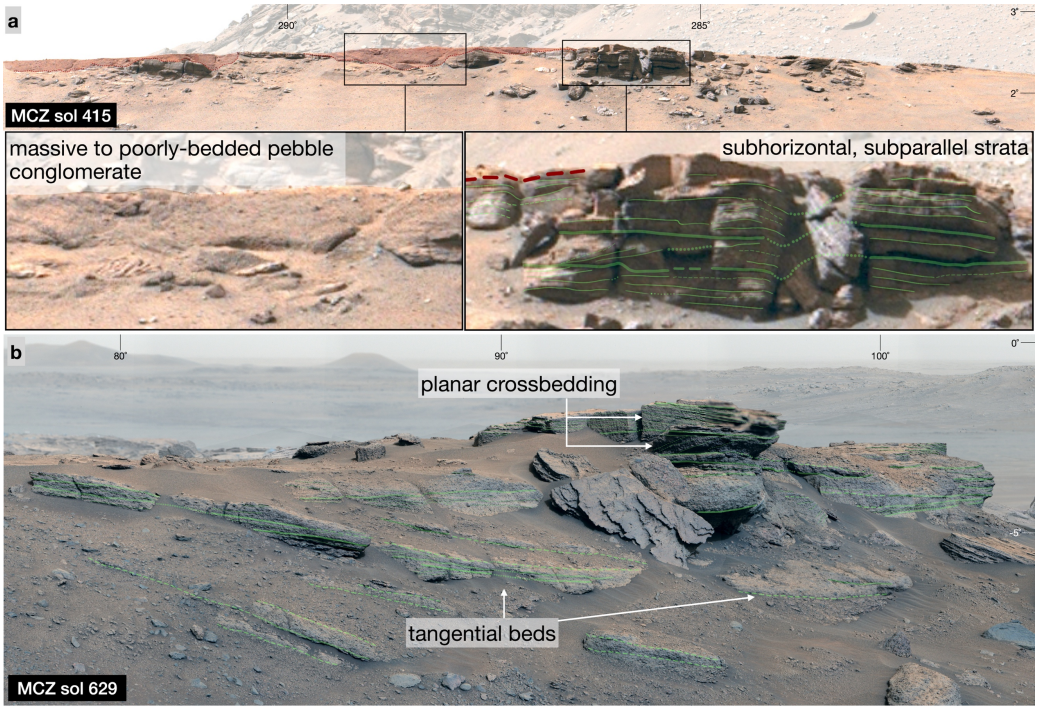

Figure 5: Cape Nukshak lithologies. Backgrounds of all images are lightened to enhance visibility of the foreground. Locations of these outcrops on the plateau margin are shown in Figure 3a. **a**: Varied lithologies along the scarp. Massive to poorly-bedded pebble conglomerate (shaded in red with the base outlined in dashed red line) appears to scour subhorizontal, subparallel beds. **b**: Alagnak outcrop. Also on the plateau margin, and plausibly sampled by HiRISE trace 4, is pebbly sandstone arranged in planar crossbedding as well as larger-scale tangentially inclined beds.

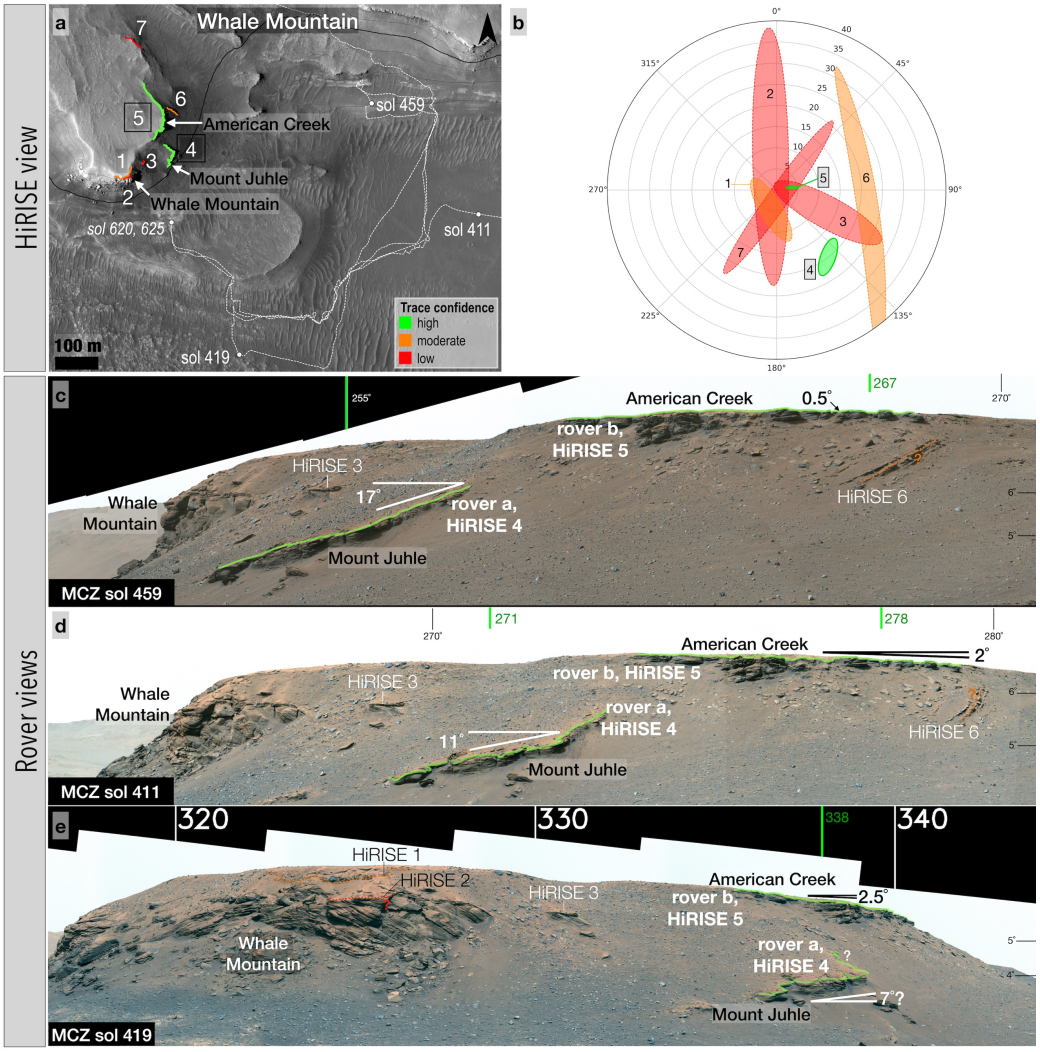

Figure 6: Orbital (**a**) and rover views (**c-e**) of the Whale Mountain locality, which include imaging targets Whale Mountain, American Creek, and Mount Juhle. **a**: HiRISE traces and Mastcam-Z imaging locations. Sols 620 and 625 images were used for sedimentology analysis (Figure 9) but not surface orientation determination. The labels of traces used for orbital-rover comparison are boxed. **b**: Solution ellipses for HiRISE-based plane fits. "?" next to HiRISE 6 in parts **c-e** indicates uncertainty regarding the exact part of the outcropping package that was traced from orbit. Green tick marks note azimuths used in orientation estimates. The apparent dip of *rover a – HiRISE 4* is difficult to distinguish from outcrop geometry in part **e**.

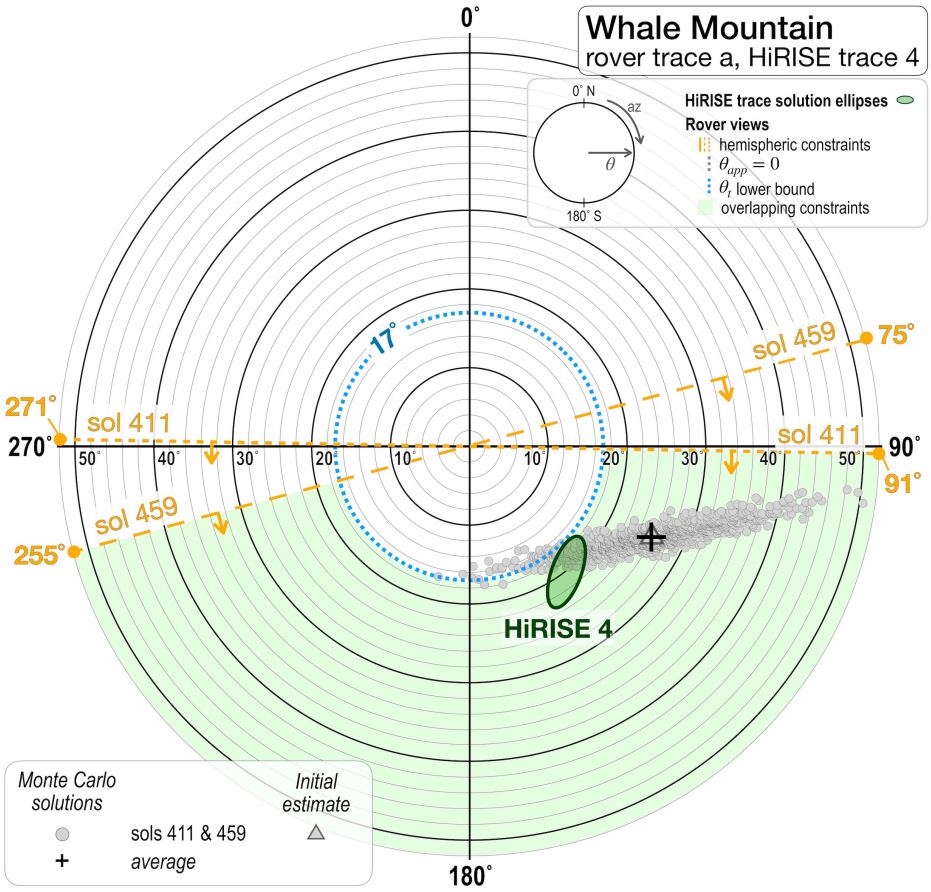

Figure 7: Rover-based orientation constraints (shaded light green) from az_{app} and $\theta_{app,\,max}$ (dotted blue line), rover-based Monte Carlo simulations (cloud of dots), and orbital-based HiRISE plane fits (shaded green ellipse) for Whale Mountain rover trace *a*. Triangle shows the az_t and θ_t calculated from the initial estimates (θ_{app_0}) for the image pair. "+" marks the average of the Monte Carlo solutions. Orange lines (dashed or dotted) demarcate lines of sight for Mastcam-Z images in which the trace appears inclined, with orange arrows indicating the direction of az_{app}.

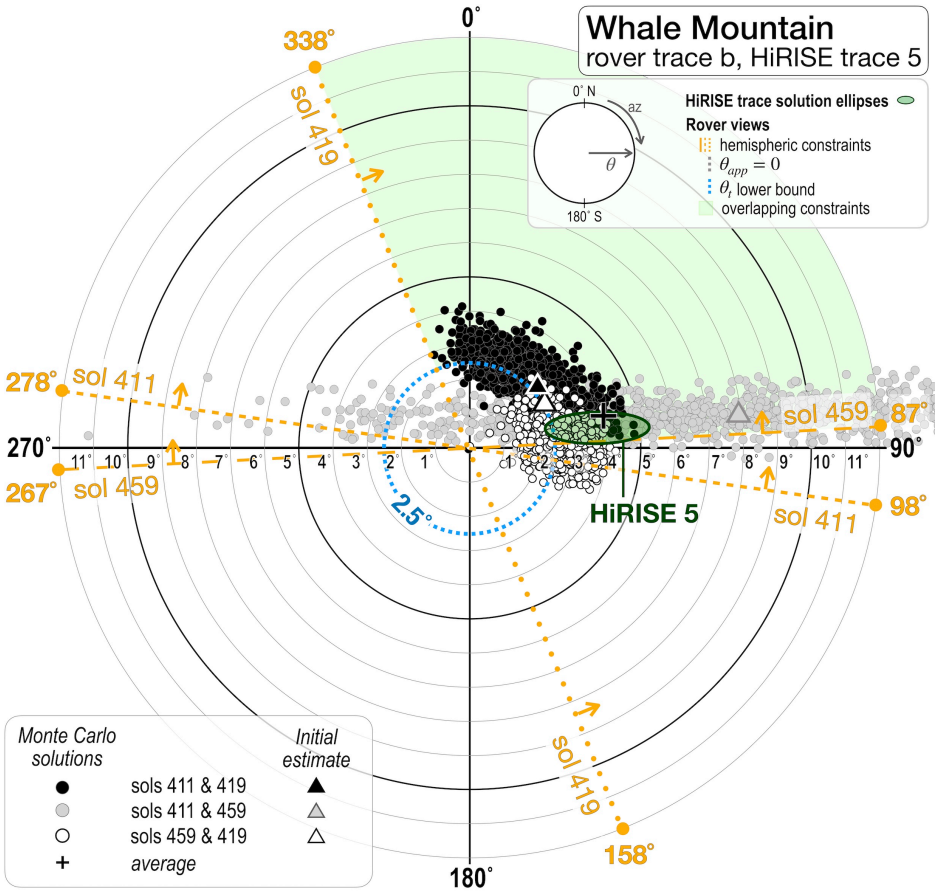

Figure 8: Rover-based orientation constraints (shaded light green) from az_{app} and $\theta_{app,\,max}$ (dotted blue line), rover-based Monte Carlo simulations (cloud of dots), and orbital-based HiRISE plane fits (shaded green ellipse) for Whale Mountain rover trace *b*. Triangles show the az_t and θ_t calculated from the initial estimates (θ_{app_0}) for the image pairs. "+" marks the average of the Monte Carlo solutions. Orange lines (dashed or dotted) demarcate lines of sight for Mastcam-Z images in which the trace appears inclined, with orange arrows indicating the direction of az_{app}.

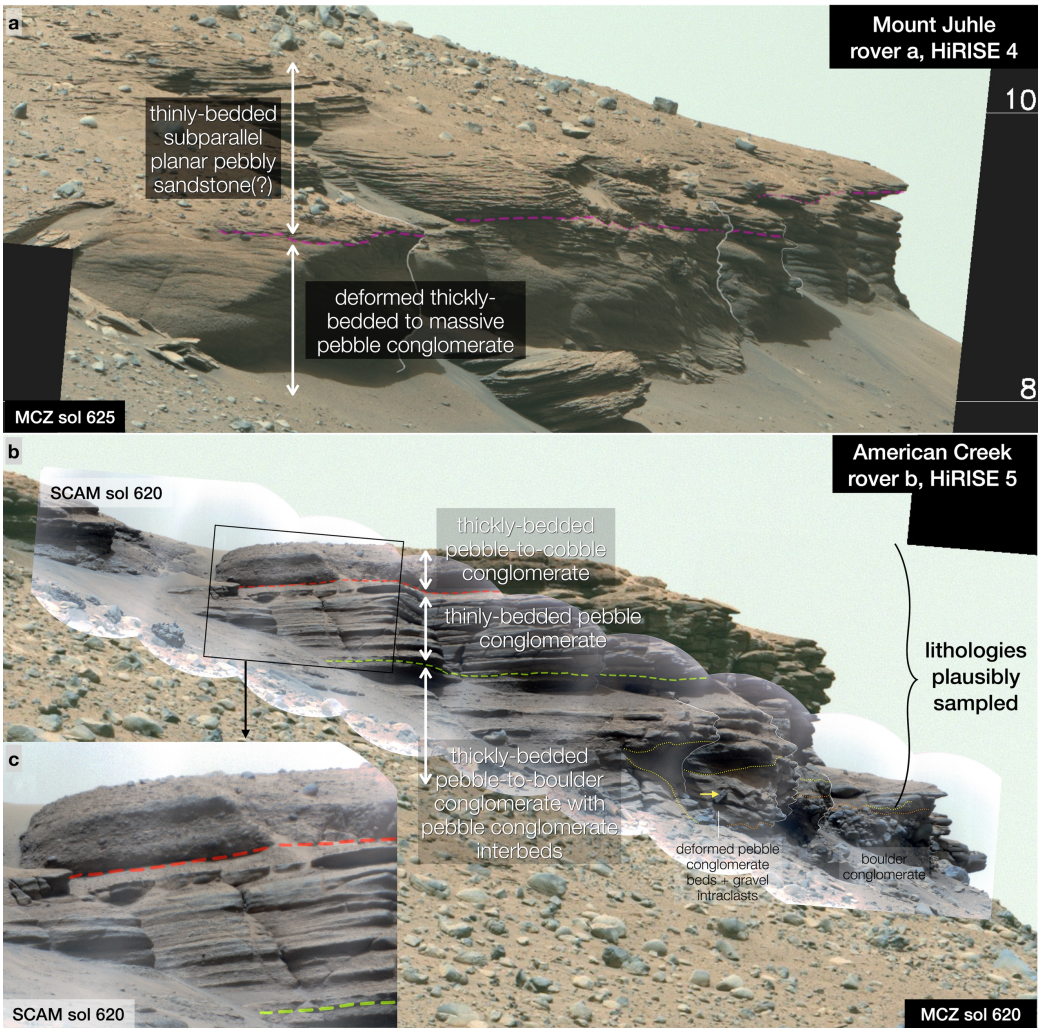

Figure 9: Whale Mountain locality lithologies. Part **a** shows the inclined beds at Mount Juhle. Only the upper thinly-bedded strata was sampled by the trace. Part **b** shows American Creek, at the top of the Whale Mountain promontory. This outcrop exhibits conglomerate lithologies, with positive-relief intervals of the uppermost three varieties likely sampled by the trace. The underlying lens of deformed conglomerate beds (including potential lithoclast, yellow arrow) and grain-supported boulder conglomerate was not sampled.

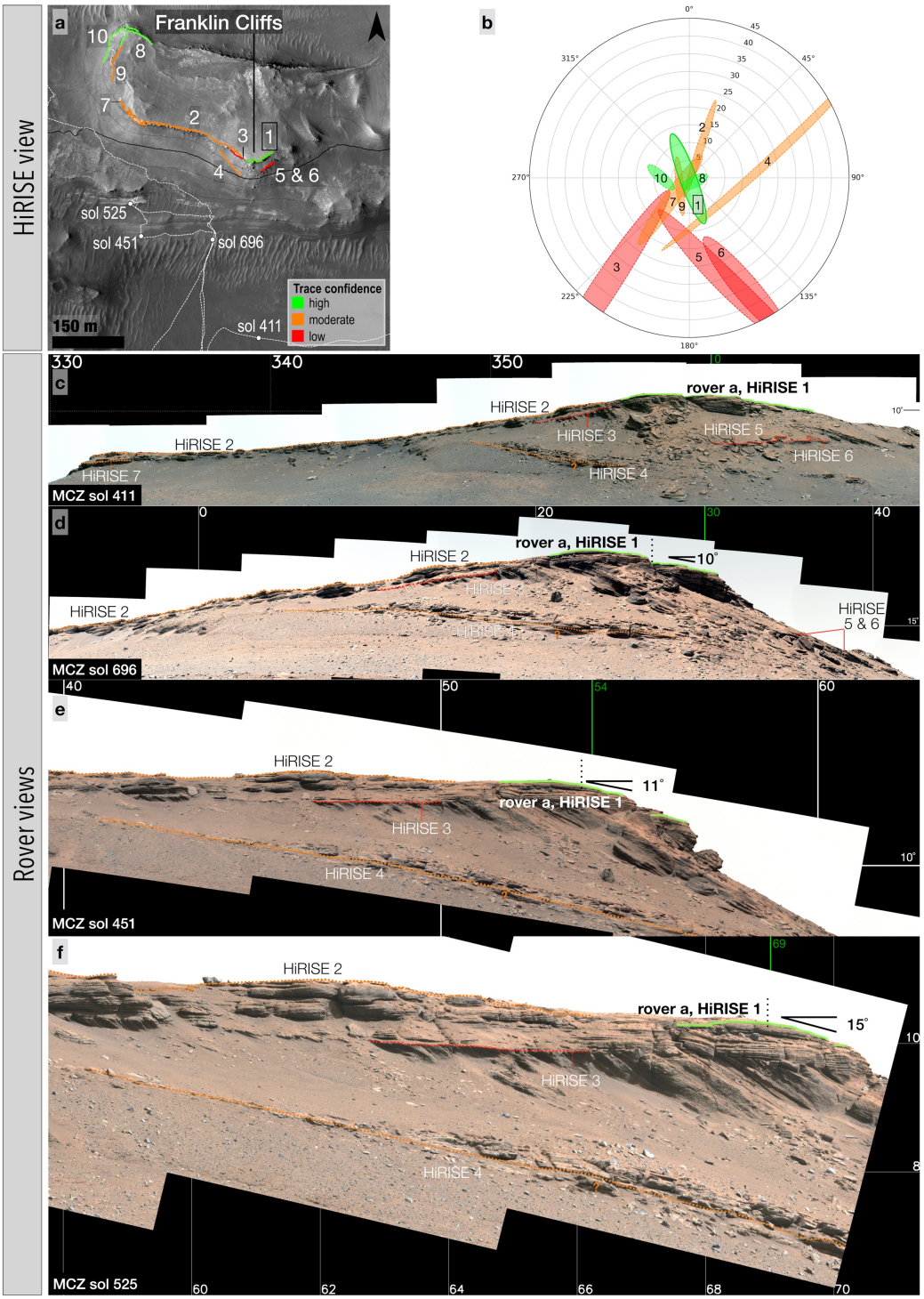

Figure 10: Orbital (**a**) and rover views (**c-f**) of the Franklin Cliffs locality. Part **a** shows HiRISE traces and Mastcam-Z imaging locations. The labels of the trace used for orbital-rover comparison are boxed. (Continued next page.)

Figure 10 caption continued: b: Solution ellipses for HiRISE-based plane fits. Trace *rover a – HiRISE 1* is divided by a dotted line in parts **d-f**, which separates a roughly horizontal portion of the surface (left) from a more steeply-inclined portion (right). Note portions of traces *HiRISE 2* and *HiRISE 4* are cropped out in parts **e** and **f** for purposes of visibility of other traces. "?" next to HiRISE 4 in parts **c-f** indicates uncertainty regarding the exact part of the outcropping package that was traced from orbit. Green tick marks note azimuths used for orientation calculations.

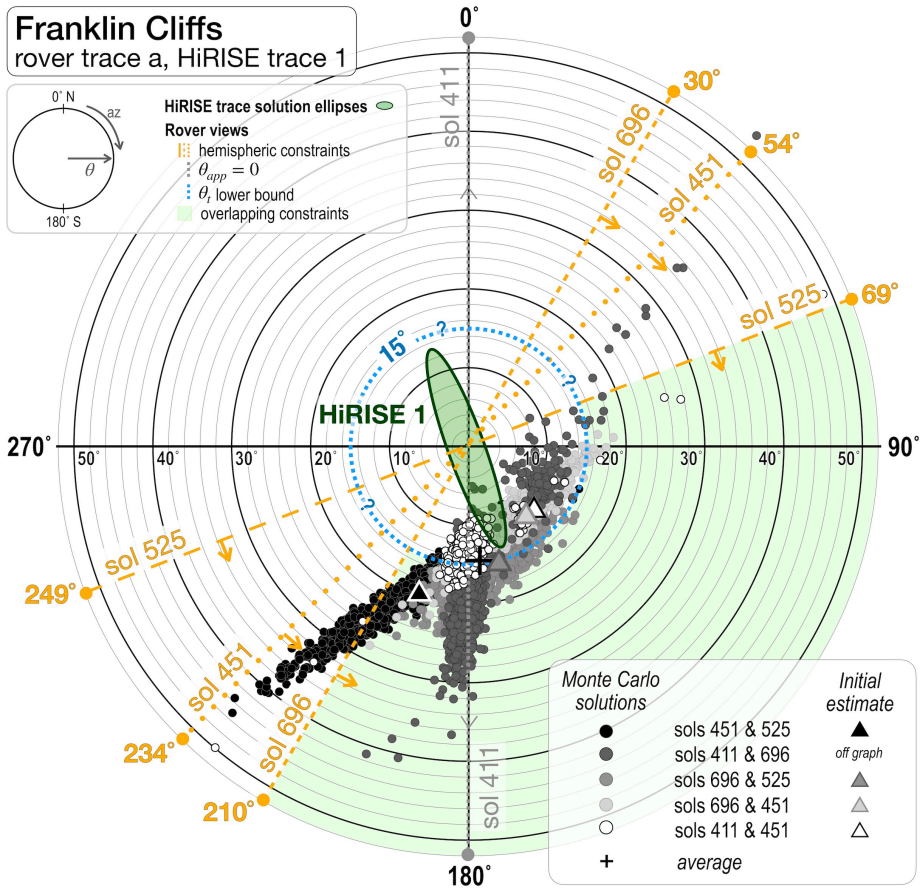

Figure 11: Rover-based orientation constraints (shaded light green) from az_{app} and $\theta_{app,\,max}$ (dotted blue line), rover-based Monte Carlo simulations (clouds of dots), and orbital-based HiRISE plane fits (shaded green ellipse) for Franklin Cliffs rover trace *a*. Triangles show the az_t and θ_t calculated from the initial estimates (θ_{app_0}) for the image pairs. Initial estimate value for sols 411 and 696 occurs at 200˚ az., 57.6˚ dip angle, and is cropped out for visibility of the other data. "+" marks the average of the Monte Carlo solutions. Orange lines (dashed or dotted) demarcate lines of sight for Mastcam-Z images in which the trace appears inclined, with orange arrows indicating the direction of az_{app}. Uncertainty is also noted in the lower bound of θ_t as "?" due to irregularity in the trace, which includes both a ~horizontal and an inclined portion (in which the 15˚ dip is observed).

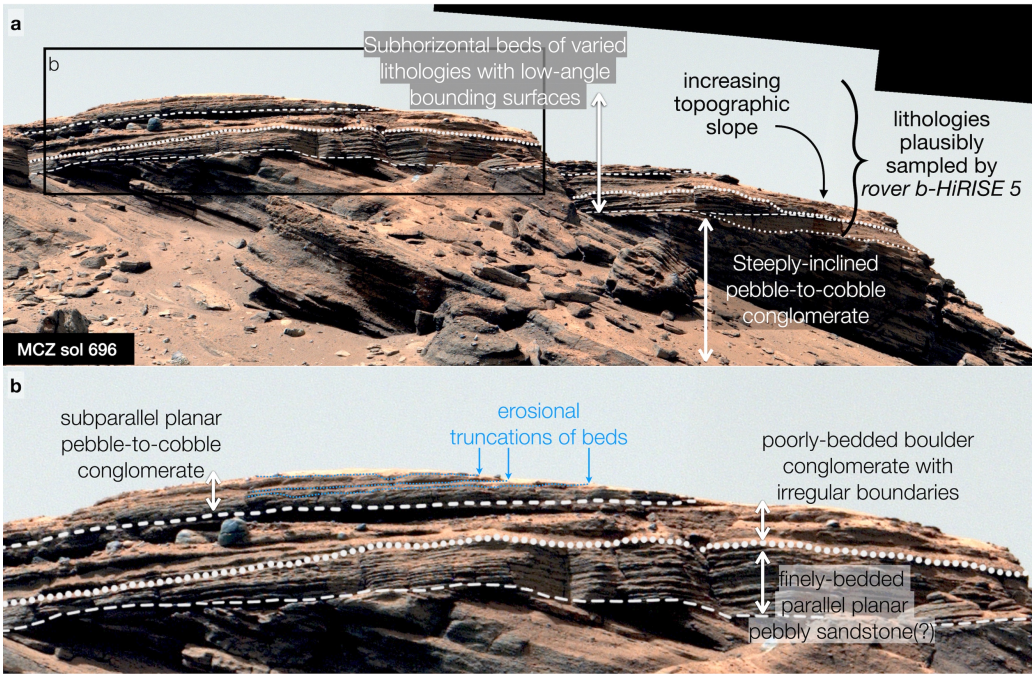

Figure 12: Franklin Cliffs stratigraphy. Steeply-inclined conglomeratic beds are sharply truncated by a sequence, sampled by the trace *rover b – HiRISE 5*, of predominantly subparallel beds with horizontal to low-angle bounding surfaces that divide lithologies. A section of increased topographic slope is noted, possibly reflecting the base of the boulder conglomerate interval, in part **a**. Detail view of capping lithologies is provided in part **b**, along with annotation of erosionally-truncated beds.

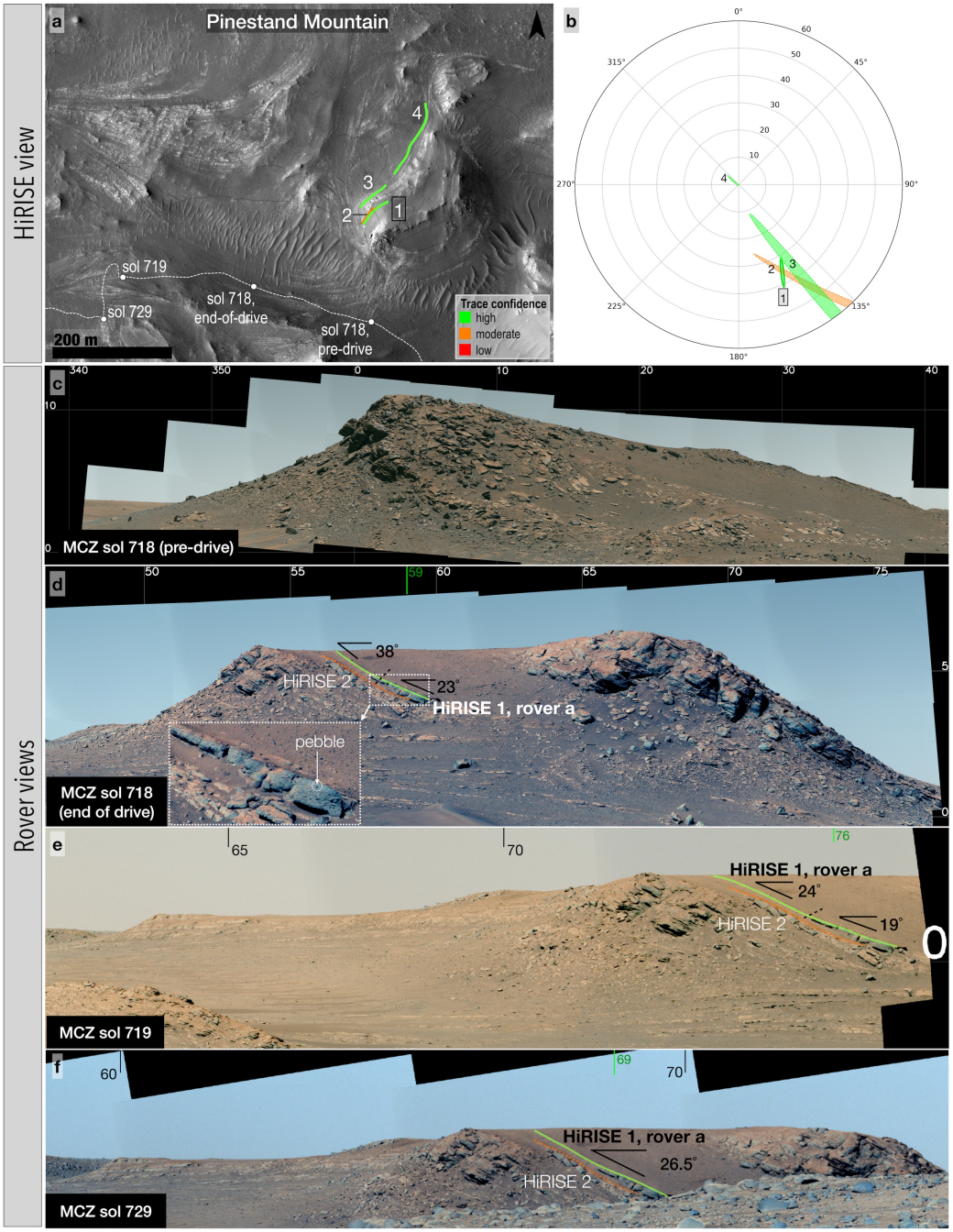

Figure 13: Orbital (**a**) and rover views (**c-f**) of the Pinestand Mountain locality. Part **a** shows HiRISE traces and Mastcam-Z imaging locations; note images from sol 718 were taken in two locations, before and after the rover completed a drive. The labels of the trace used for orbital-rover comparison are boxed. **b**: Solution ellipses for HiRISE-based plane fits. Tangential geometry of the traced bed is visible in part **d**, with inset close-up of pebble conglomerate. Green tick marks note azimuths used for orientation calculations.

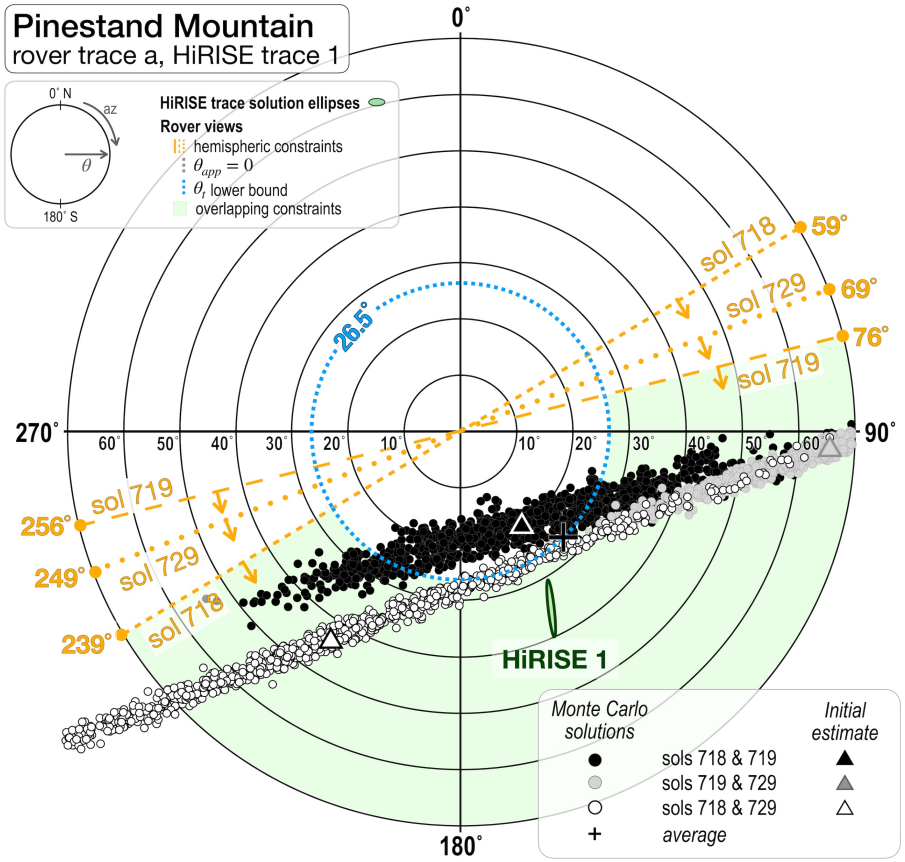

Figure 14: Rover-based orientation constraints (shaded light green) from az_{app} and $\theta_{app,\,max}$ (dotted blue line), rover-based Monte Carlo simulations (clouds of dots), and orbital-based HiRISE plane fits (shaded green ellipse) for Pinestand Mountain rover trace *a*. Triangles show the az_t and θ_t calculated from the initial estimates (θ_{app_0}) for the image pairs. "+" marks the average of the Monte Carlo solutions. Orange lines (dashed or dotted) demarcate lines of sight for Mastcam-Z images in which the trace appears inclined, with orange arrows indicating the direction of az_{app}.

Chapter 5

CONCLUSIONS

In our study of two craters of similar sizes, potentially similar ages, and both in a circumequatorial latitude band, we have nonetheless observed a considerable difference in the geologic processes that shaped them. Much of the morphological work that occurred to shape Endeavour crater's rim may have occurred in the absence of water; rather, the tumbling of boulders, shed from steep portions of its rim, may have created alcoves and incisions. If flowing surface water was present, its footprint is limited to a shallow anastomosing gully, with no depositional fan that can be observed today. On the other hand, Jezero crater hosted high-energy environments: a deep, rushing river that transported clasts as large as boulders in repeated flow events, which arranged sediment in large advancing bedforms, either mid-channel bars or mouthbars in a shoal-water delta. Where a lake in Jezero was previously implied to be a relatively quiescent environment, with inlet flows shallow in comparison to the lake depth, allowing for a low-energy lakebed and the accumulation of clay-rich suspended sediment, our analysis of the 3-D architecture of the fan remnant Kodiak butte and comparison to analogous terrestrial deposits suggests that this lake was shallow compared to the inlet channel depth, would have had sustained currents, and may have been more likely to be ephemeral. Such an environment may have continued for a geologically significant amount of time as the crater infilled, as similar

deposits are found throughout the fan succession. The environmental conditions implied by the morphology and stratigraphy of the fan deposits provide important context for samples cached by the Perseverance rover and the potential biosignature detected upsection near the inlet mouth (e.g., Hurowitz et al., 2025). Significant as well, in the absence of biological activity, would be providing the geologic context in which pre-biotic reactions were occurring. Finding, for instance, that habitable conditions (at least, in terms of water abundance and duration) alone are not sufficient to initiate the development of microbial life, is itself an exciting discovery that inspires further investigation into the requirements for life to both emerge and persist long enough to shape its surroundings. In short, to understand the controls on whether life emerges from an abiotic landscape first requires understanding the landscape.

On the topic of lifeforms, this study (and those that follow from it) may hopefully contribute more generally to comparative planetology studies. Studies of climate evolution at the current moment may be both esoteric and self-interested: just as we investigate the boundaries of habitability for simple organisms, so we too explore the limitations of our own survival on a planet undergoing a rapid human-imposed climate transition. Investigations of the process by which Mars changed from a habitable planet to a cold desert may now be gaining additional urgency in an age of climate disaster preparation and mitigation.

On a more optimistic note, we continue developing ever more advanced technologies and methodologies to scour the rock record of Mars (and Earth). I am

therefore also concerned with the implementation of these tools, lending an epistemological bent to a portion of this work, as I seek to identify and describe the margins of the usefulness of the datasets and workflows upon which planetary scientists frequently rely (namely, orbital data). This is less of a concrete outcome as a mindset or a practice of describing certainty (or lack thereof) and intentionality in designing research questions suitable for the data one seeks to use. Similarly, I have found it is important to relate deposits and phenomena occurring on Mars to terrestrial deposits and processes; to be grounded, as it were, in studies of landforms most accessible to us Earthlings. Such exercises foster a deeper understanding of the potential ancient environments. I have also experienced the necessity of holding curiosity of not just what is "right," but what is *possible*. This too, is not a result, but a process of questioning: What scenarios can be disproven? What alternatives exist? Asking and answering these questions, as I have learned, is fundamental to the scientific integrity I seek to cultivate.

References

Hurowitz, J. A. et al. (2025). The detection of a potential biosignature by the Perseverance rover on Mars. 56th Lunar and Planetary Science Conference, Lunar and Planetary Institute, Mar 2025, The Woodlands (Texas), United States. Abstract # 2581. Retrieved from: https://www.hou.usra.edu/meetings/lpsc2025/pdf/2581.pdf

JGR: Planets

Supporting Information for

3D architecture of Kodiak butte as evidence of fluvial or shoal-water environments in Jezero crater, Mars

O. A. Kanine[1], M. P. Lamb[1], B. L. Ehlmann[1], J. P. Grotzinger[1], C. D. Tate[2]

[1]Division of Geological and Planetary Sciences, California Institute of Technology, Pasadena, CA, [2]Department of Astronomy, Cornell University

Contents of this file

Additional Supporting Information (Files uploaded separately)

Introduction

Within this document there are additional details on the process of plane-fitting (Text S1), including the location of beds analyzed (Figures S1-S5). The best fit solutions of each bed orientation are in Data Set S1 (ds01.xlsx). Then follows a description of the process of grain counting (Text S2), details on the image resolutions (Table S1), locations of counts (Figures S6-S8) and detailed results of the grain counts (Figure S9, Table S2) used to determine the median grain size used in paleohydraulic calculations. Raw grain size measurements are in Data Set S2 (file ds02.xlsx). Bar front heights are in Figure S10 and Tables S3 and S4, and the discharge estimates are presented in Figure S11 and Table S5. Terrestrial analogs for large-scale braid bar deposits, mouth bar deposits, and Gilbert deltas are given in Tables S6-S8, respectively.

S1 Bed orientations

288 traces were taken across the Kodiak model along segments of beds that can be locally approximated as planar. These were placed into 21 groups (named Group A through U) which sample Units 2, 3, and 4 (Figure S1). Detail views of trace locations and the plane fits for each group are presented in Figures S2-S4, while Figure S5 shows the orientations of beds organized by both group and unit. Individual plane fits corresponding to the labeled traces in Figures S2-S4 may be found tabulated in the file *ds01.xlsx*.

Data Set S1. A spreadsheet of best-fit solutions for bed orientations is found as *ds01.xlsx*. Beds are organized by "Group" (see Figures S1-S5), and the dip angle, dip azimuth, strike, minimum angular error (Min_e), maximum angular error (Max_e), and rake of each fitted plane is given.

Data Set S2. File *ds02.xlsx* is a spreadsheet of grain lengths, ordered largest to smallest, and the calculated fraction finer using Equation S1.

S2 Grain counts

Grain size counts on the eastern face of Kodiak were performed in two boxes, measuring ~19 m x ~7 m (box 1) and ~8.2 m x ~10 m (box 2) (Figure S6) that sample representative Unit 3 strata along the beds used for paleochannel depth estimates (Figure S5a). To facilitate interval-based sampling analogous to a Wolman pebble count performed in the field (Wolman, 1954), Box 1 contains a grid with 7,367 intersections overlaid on SuperCam image scam01063 and Box 2 contains 4,588 intersections overlaid on SuperCam image scam01077. Both images were color stretched to the minimum and maximum values of the current view extent while counting and were manually co-registered to corresponding sol Mastcam-Z images using a linear fit to facilitate direct comparison between the instrument datasets. Various criteria were used to identify grains, including: color; shape (rounded); relief (as indicated by shadowing) from the surrounding rock; visibility in different images (i.e., observable in both the aforementioned sol 63 and sol 77 SuperCam images) where available to represent different lighting conditions, view angles, and image stretches; not talus; not cut by visible layers aligned with the surrounding bedding fabric; and not associated with other confounding features such as a fracture or a weathering-resistant bed with knobby texture. We recognize that these criteria bias the count toward larger, darker grains that contrast against the surrounding rock, and may have eliminated some real grains from the count. Nevertheless, in absence of physical access to the outcrop, we favor greater certainty over over-interpretation of long-distance images in service of producing order-of-magnitude estimates of the hydrology of the depositing flow, and favor consistent, rule-based counts in service of scientific reproducibility. While not counted, one may note a "mottled" texture in the SuperCam images, especially in rubbly-textured beds, which may indicate the presence of clasts with diameters around or just below the imaging resolution (Morgan et al., 2014) (i.e., ~2.5 cm for the sol 63 SuperCam image (Table S1)); this is consistent with our estimates of a D_{50} between ~1 and ~3.6 cm. We also note this range is aligned with the proposed grain size of Catuneanu et al. (2023). We choose the value of 2.6 cm for hydrology calculations as it is derived from the most heavily sampled bin and close to the mean calculated D_{50} of 2.3 cm for all bins.

The longest axis exposed on the identified grains was recorded (Figures S7, S8). Physical lengths were calculated by multiplying the length of the traced axis in pixels by the image resolution (Table S1). The summary of the count is presented in Figure S9. Grains were counted if their boundaries appeared to be within 1 pixel width of the grid intersection, and if a grain crossed more than one intersection on the grid, each overlapped intersection was counted. We infer that the visible grains comprise the coarsest fraction of the sedimentary deposit, and that every intersection where a grain was not visible, the grain present must be too small to be resolved (i.e., < 7.4 cm for the sol 63 SuperCam image). Following this logic, we can estimate the percentage of the outcrop finer than a given grain, starting with 100% of the grains in the box being smaller than the largest counted grain. The D_{50} may then be estimated from this coarse fraction using the cumulative distribution function in Equation S1, which assumes a log-normal distribution for the sediment sizes (Parker, 2004). We assume that $D_{84}/D_{50} = 2$. The results of the D_{50} calculation are presented in Table S2.

$$f_{finer} = \frac{1}{2}\left[1 + erf\left(\frac{lnD_{bin} - lnD_{50}}{\sqrt{2}ln\frac{D_{84}}{D_{50}}}\right)\right] \quad \textbf{Equation S1}$$

S3 Paleo-discharge

We utilize our estimates of channel geometry, bedload grain size, and empirical relationships for terrestrial rivers to constrain the magnitude of the flow that deposited Kodiak. First, we may use the relationship between bankfull stress (τ_*) for steady uniform flow (Equation S2) and the critical Shield's number (τ_{*c}) for incipient particle motion in coarse, braided rivers (Equation S3, Paola and Mohrig, 1996) to solve for channel slope (S) (Equation S4, Lamb et al., 2008). R, the submerged specific gravity of sediment, is assumed to be 2.0 for a basaltic bedload. For a sand-bedded river, we infer most of the flow resistance is due to large-scale bedforms (e.g. Paola and Mohrig, 1996; Parker and Peterson, 1980) and thus the equations below remain valid.

$$\tau_* = \frac{dS}{RD_{50}} \quad \textbf{Equation S2}$$

$$\tau_* \approx 1.4\tau_{*c} \quad \textbf{Equation S3}$$

$$\tau_{*c} \approx 0.15\left(S^{0.25}\right) \quad \textbf{Equation S4}$$

Combining equations S2 - S4 gives:

$$S = \left[\frac{100}{21}\left(\frac{d}{RD_{50}}\right)\right]^{-\frac{4}{3}} \quad \textbf{Equation S5}$$

We use the variable-power resistant formula for gravel and boulder-bedded rivers (Equation S6) proposed in Ferguson, 2007 with parameters $a_1 = 6.5$ and $a_2 = 2.5$ (Ferguson, 2007) to calculate a friction factor f, assuming $D_{84} \approx 2D_{50}$ ($D_{84} = 2.2D_{50}$ used in Rickenmann

and Recking, 2011, and $D_{84}= 2D_{50}$ used in Morgan et al., 2014) and thus calculate bankfull flow velocity using the Darcy-Weisbach formula (Equation S7, Silberman et al., 1968). We set the gravitational constant g = 3.72 m/s^2 for Mars. Flow depth *d* is estimated from measurements of bar strata heights in Unit 3 (Figure S10; Table S3, S4).

$$\sqrt{\frac{8}{f}} = 16.3\left(\frac{d}{D_{84}}\right)\left[42.3 + 6.3\left(\frac{d}{D_{84}}\right)^{\frac{5}{3}}\right]^{-\frac{1}{2}} \qquad \textbf{Equation S6}$$

$$u = \sqrt{\frac{8gdS}{f}} \qquad \textbf{Equation S7}$$

We may now calculate discharges for a range of channel geometries, with $Q = udw$. Studies of terrestrial gravel bed rivers indicate braiding initiates at a width-to-depth (w:d) ratio of approximately 50 (Eaton et al., 2010; Kleinhans et al., 2011). The upper bound of w:d values is less well-constrained. The dataset of braided rivers in Li et al. (2023) have w:d between ~20 and ~400, while the compilation of sand to cobble/boulder bedded braided and braided/anastomosing rivers in Church and Rood's 1983 dataset have w:d from 35 to 371. Thirteen braided or moderately braided rivers with recorded bankfull widths and depths in Kleinhans and van den Berg (2011) show a range of width-to-depth values of ~60 to ~2090. While there are braided and low-sinuosity rivers with w:d > 1000 (Parker, 1976; Gibling, 2006), most fall within 50 < w:d < 1000 (Gibling, 2006). We utilize width-to-depth ratios 50 - 400 to represent a broad range of plausible bankfull channel geometries for this system.

Using D_{50} = 2.6 cm, *d* = 4.2 (Table S4), and R = 2.0 for specific gravity of basaltic sediment bedload, we find a slope of 0.00036, a friction factor f = 0.044, and velocity u = 1.01 m/s. For a sand-bedded river with D_{50} = 2 mm, we find a slope S = 9.5 x 10^{-6}, f = 0.0187, and u = 0.25 m/s. We present our estimates of river discharge in Table 5 and Figure S11.

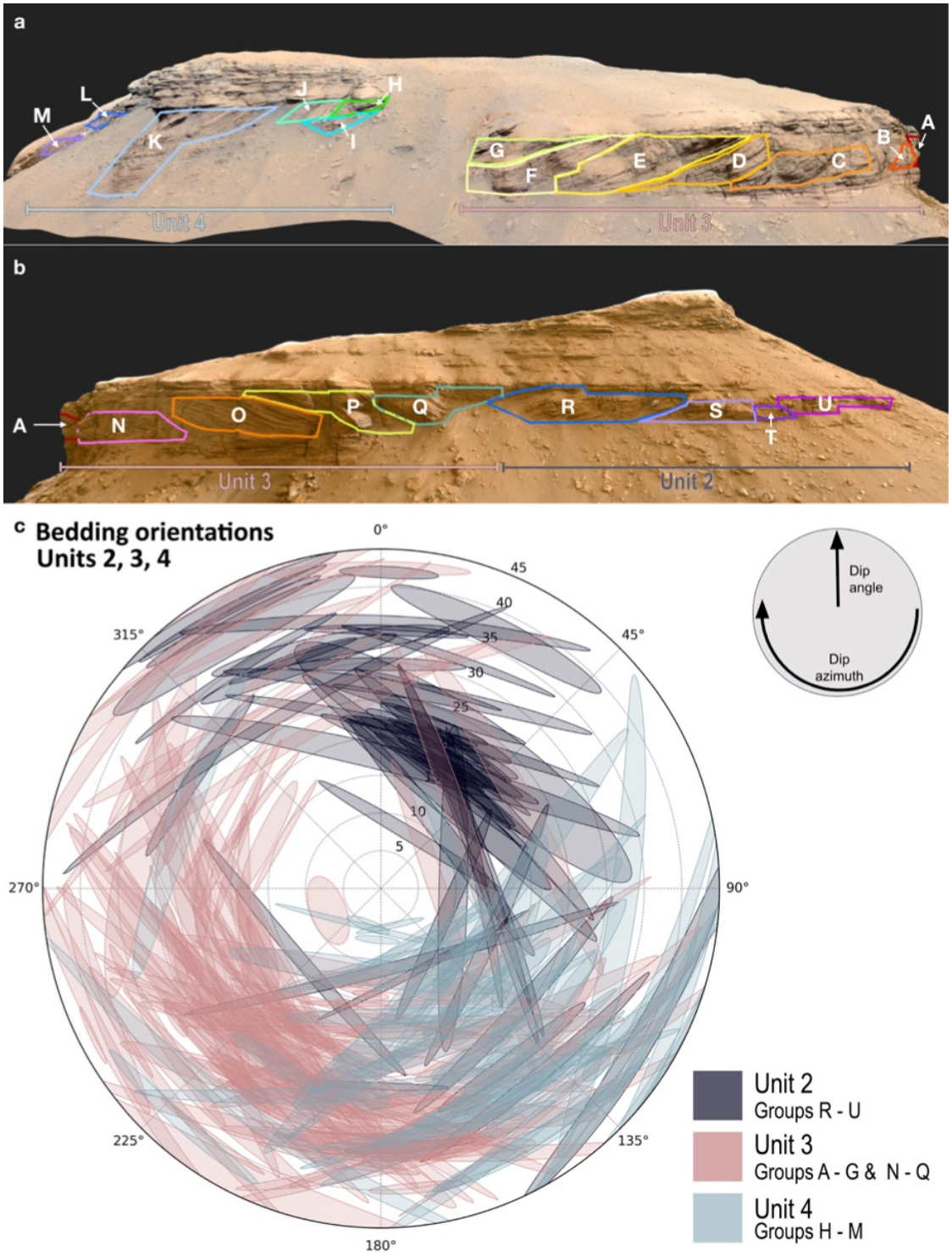

Figure S1. Bedding orientations. Part **a** shows the east face of Kodiak and sample groups A - M, which comprise units 1 and 2. Part **b** shows sample groups A and N - U on the north face of Kodiak, which make up sequences 2 and 3. Plane fits for traces in units 2, 3, and 4 are plotted in part **c** to the 95th percent confidence interval using methodology of Quinn and Ehlmann (2019). Dip azimuth is read on the perimeter of the plot, with north as 0˚, and dip angle increases radially outward from the center of the plot (see key in upper right of part **c**).

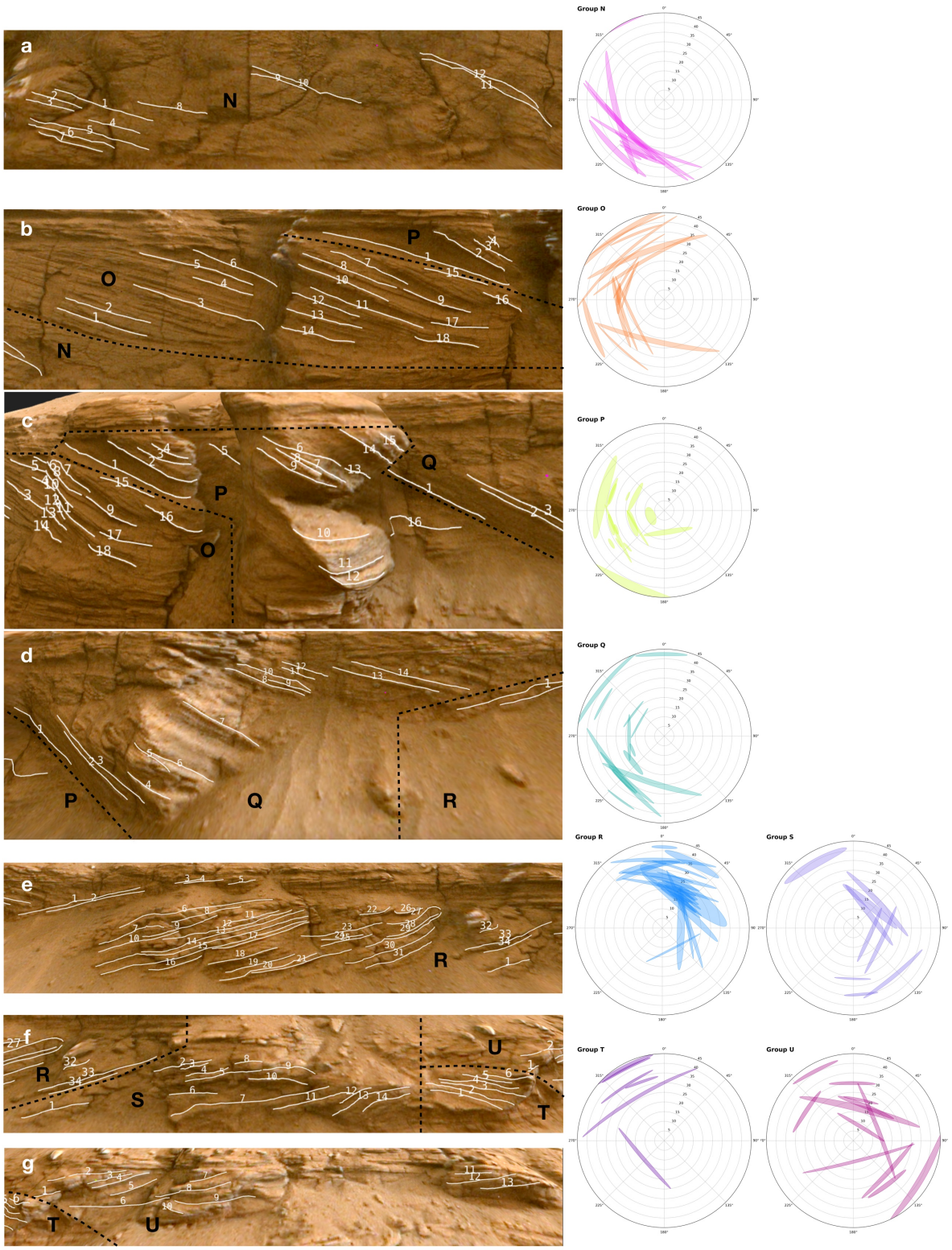

Figure S2. Trace locations (parts **a-g**) and plane fits (right) for sampling groups N-U, associated with Units 2 and 3. Colors of bed orientation plots correspond to group outlines in Figure S1.

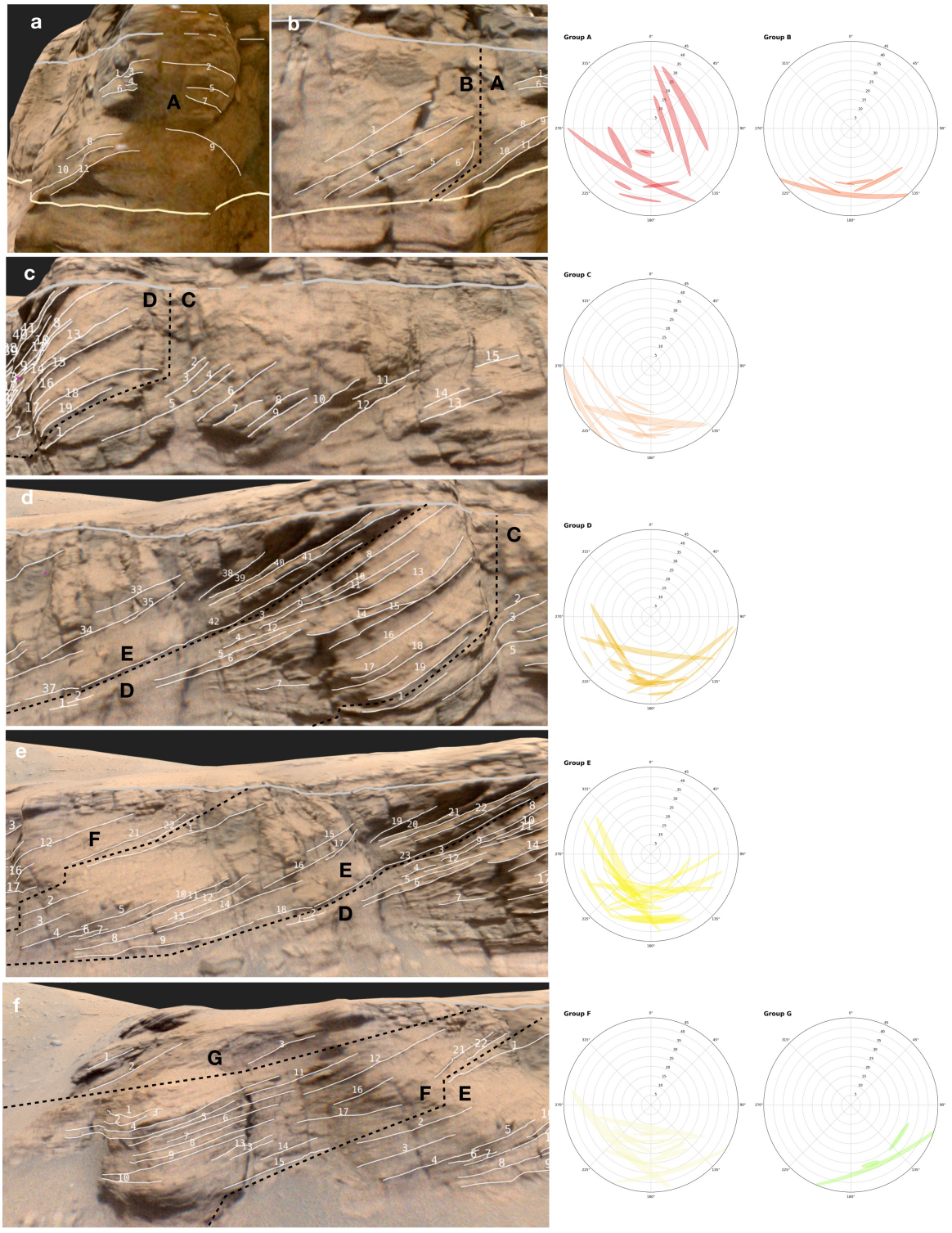

Figure S3. Trace locations (parts **a-f**) and plane fits (right) for sampling groups A-G, associated with Unit 3. Colors of bed orientation plots correspond to group outlines in Figure S1.

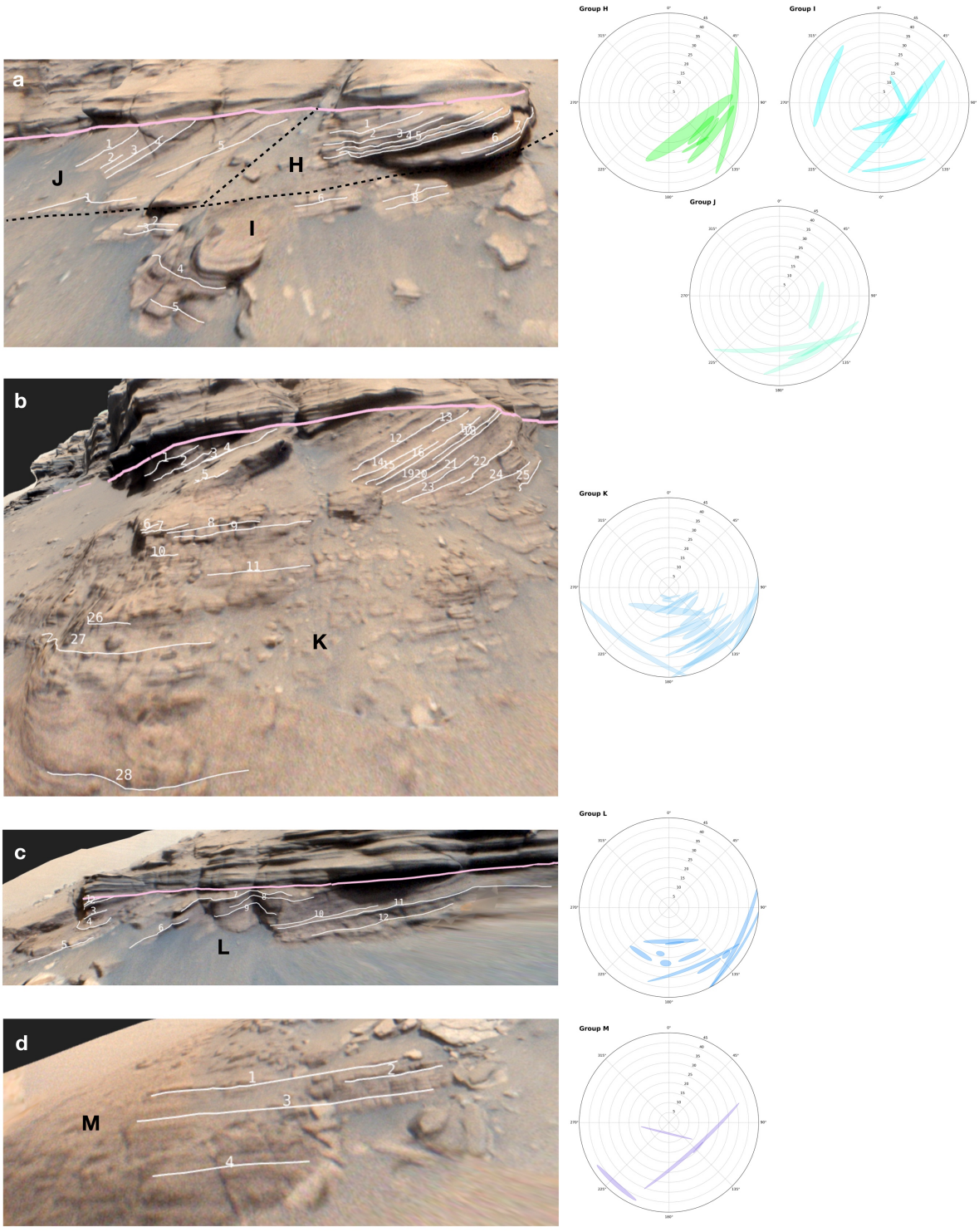

Figure S4. Trace locations (parts **a-d**) and plane fits (right) for sampling groups J-M, associated with Unit 4. Colors of bed orientation plots correspond to group outlines in Figure S1.

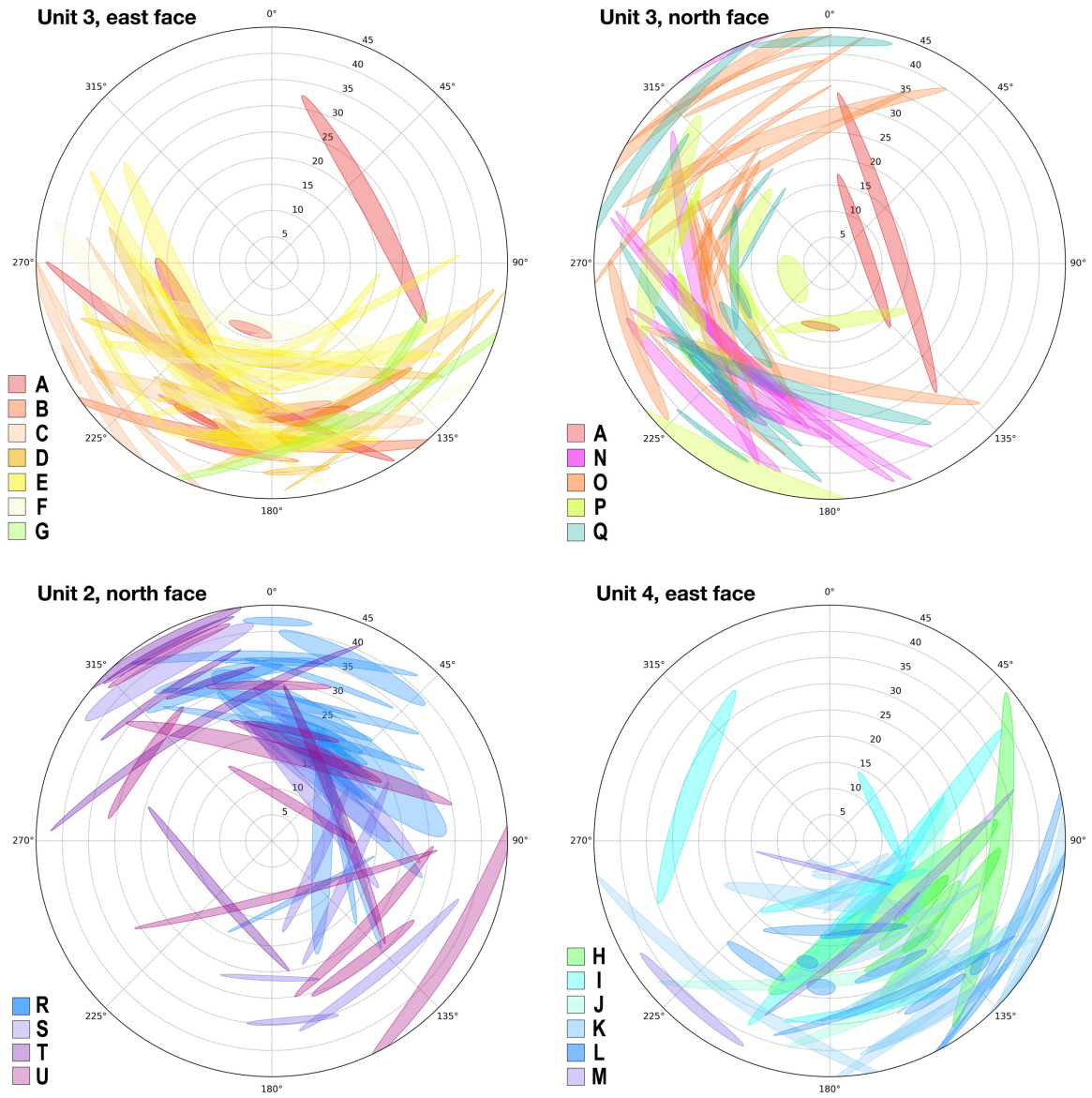

Figure S5. Bed orientations of each group organized by unit. Unit 3 is divided into the exposures on the east and north face of Kodiak.

Instrument	Sol	Sequence ID	Distance (rover to target, m)	Resolution (cm/px)	Smallest resolvable feature (3 pixels wide, cm)
Mastcam-Z	63	zcam08022	2369	17	51
	77	zcam08036*	2390	17	51
	409	zcam08425	784	5.5	17
	415	zcam08430	527	3.7	11
	416	zcam08433	478	3.3	9.9
SuperCam	63	scam01063	2369	2.47	7.4
	77	scam01077	2390	2.50	7.5
	418	scam01418*	478	0.50	1.5
	548	scam04548*	580	0.61	1.83
	580	scam01580	701	0.73	2.19

Table S1: Key images of Kodiak with their resolutions and the size limits of resolvable grains. *Images are usable for some visual analysis but were not incorporated into the 3D model.

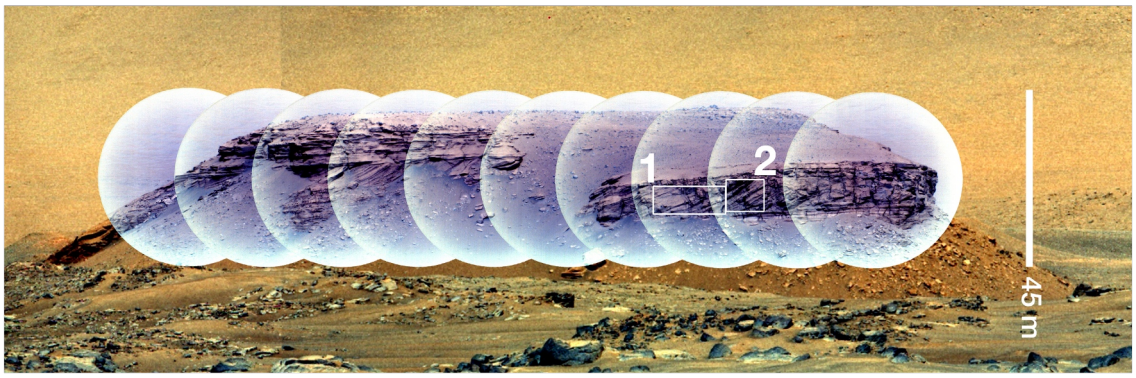

Figure S6. Grain count sample locations over sol 63 Mastcam-Z (zcam08022) and SuperCam (scam01063) color-enhanced mosaics.

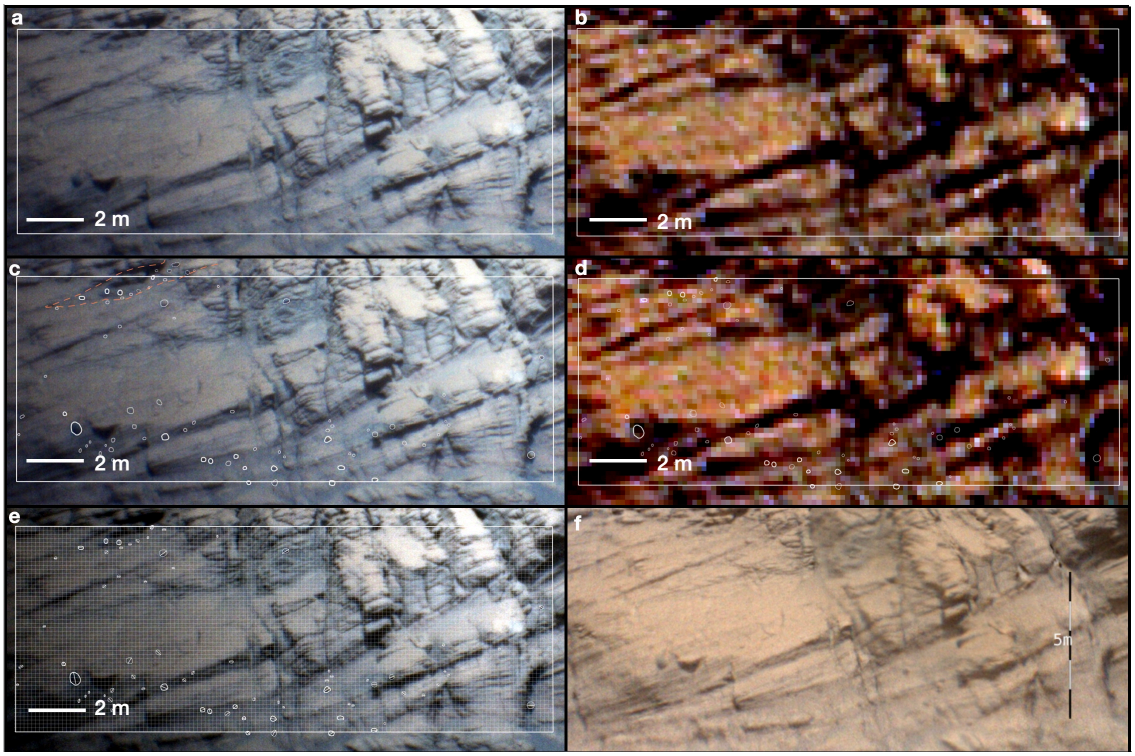

Figure S7. Grain counts and comparison of SuperCam and Mastcam-Z images, box 1. Parts **a**, **c**, and **e** utilize a sol 63 SuperCam frame, while **b** and **d** use a sol 63 Mastcam-Z image. The white box in all parts of this figure shows the extent of the grid used for grain counting in Box 1. Parts **c** and **d** include outlines of identified grains, and **c** shows a coarse lens in dashed red line; **e** shows the grid partially transparent over the base SuperCam image in addition to the grain outlines and long axis measurement locations. Part **f** shows approximately the region sampled in **a**-**e** as viewed on the 3D model looking to the east.

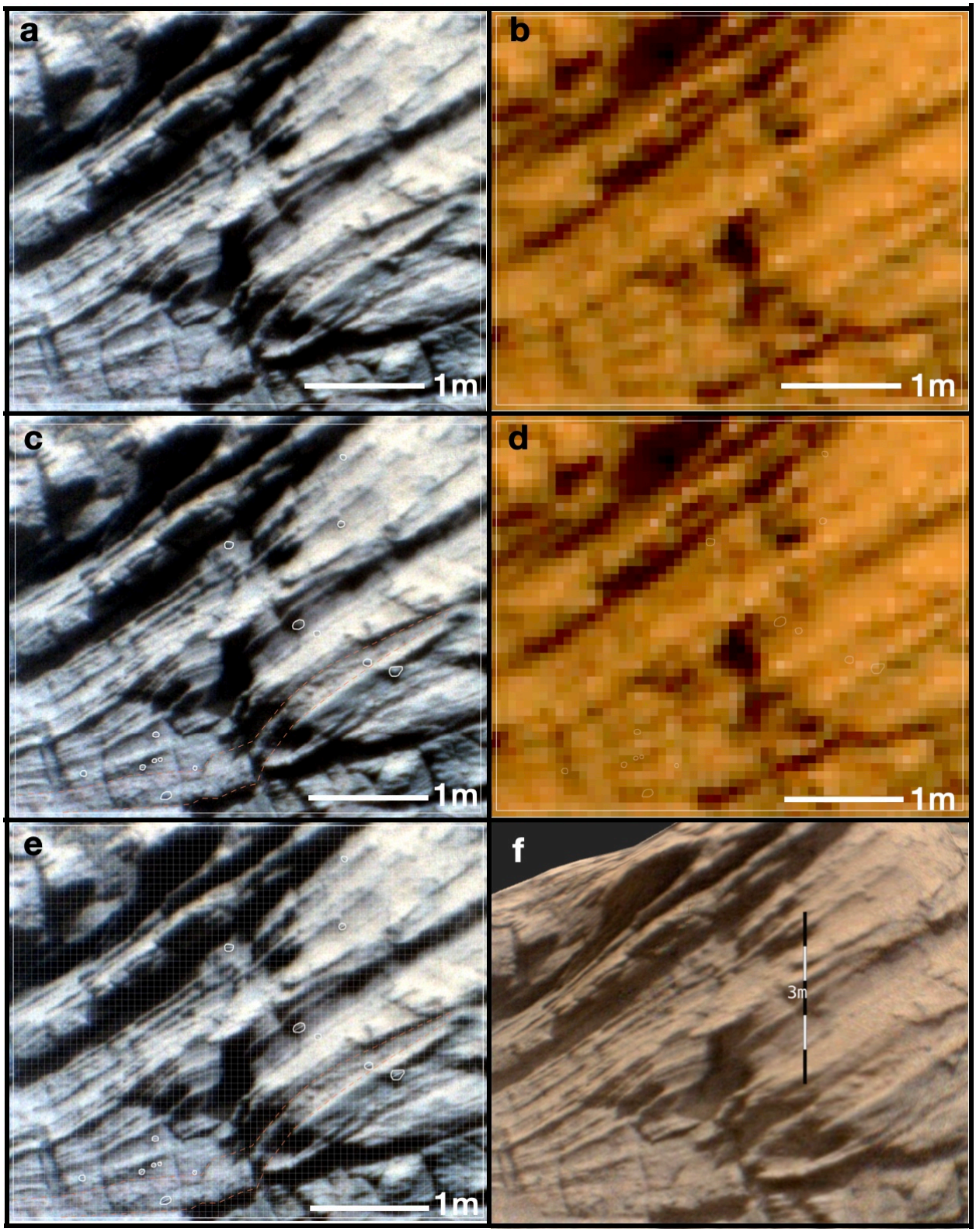

Figure S8. Grain counts and comparison of SuperCam and Mastcam-Z images, box 2. Parts **a**, **c**, and **e** utilize a sol 77 SuperCam frame; **b** and **d** use a sol 77 Mastcam-Z image. The white box in all parts of this figure shows the extent of the box 2 grid used for grain counting. **c** and **d** include outlines of identified grains and a coarse lens (red dashed line); **e** shows the grid partially transparent over the base SuperCam image in addition to the grain outlines and long axis measurement locations. Part **f** shows approximately the region sampled in **a**-**e** as viewed on the 3D model looking to the east.

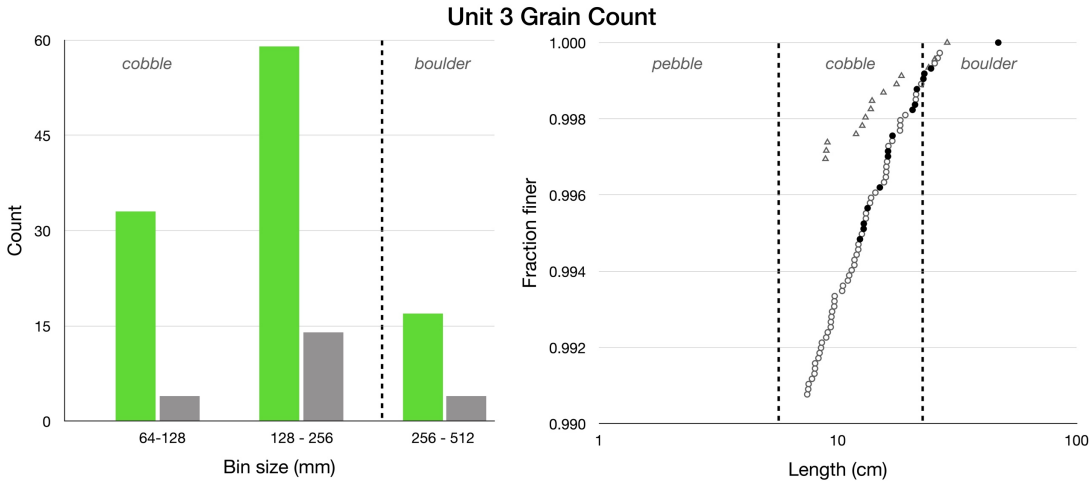

Figure S9. Histogram and fraction finer calculations for Unit 3. The green bars are counts from Box 1, while grey show results from Box 2; filled black circles are high-confidence grains from Box 1, and open circles show the remaining mapped grains. Triangles show grains mapped from Box 2.

Sample	Image	Bin [mm]	Count	f_{finer}	Calculated D_{50} [cm]
Box 1	scam01063	64 -128	33	0.985	1.4
		128 - 256	59	0.990	2.6
		256 - 512	17	0.998	3.6
Box 2	scam01077	64 -128	4	0.995	1.1
		128 - 256	14	0.996	2.0
		256 - 512	4	0.999	2.9

Table S2. Grain count results from Unit 3. D_{50} is extrapolated from the measured grains in each bin (assumed to be the coarse fraction) using equation S1.

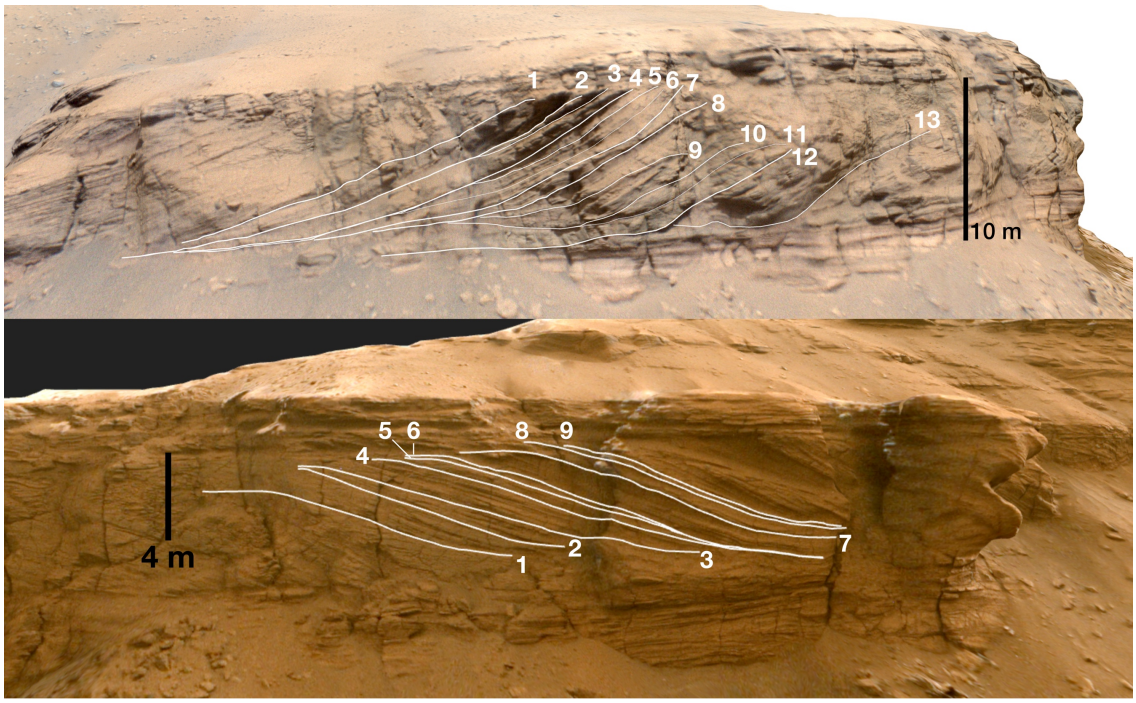

Figure S10. Locations of Unit 3 bed height measurements, east face on top and north face below. Values are reported in Tables S3 and S4.

North face	
Trace	Height [m]
1	3.1
2	3.8
3	4.1
4	4.8
5	4.8
6	4.9
7	4.1
8	4.2
9	3.9

Table S3. Vertical height of inclined beds on north face (Fig. S10, bottom).

East face	
Trace	Height [m]
1	8.9
2	10.1
3	10.6
4	10.1
5	10.2
6	10.0
7	10.1
8	7.9
9	4.1
10	5.2
11	5.1
12	6.4
13	5.6

Table S4. Vertical height of inclined beds on east face (Fig. S10, top).

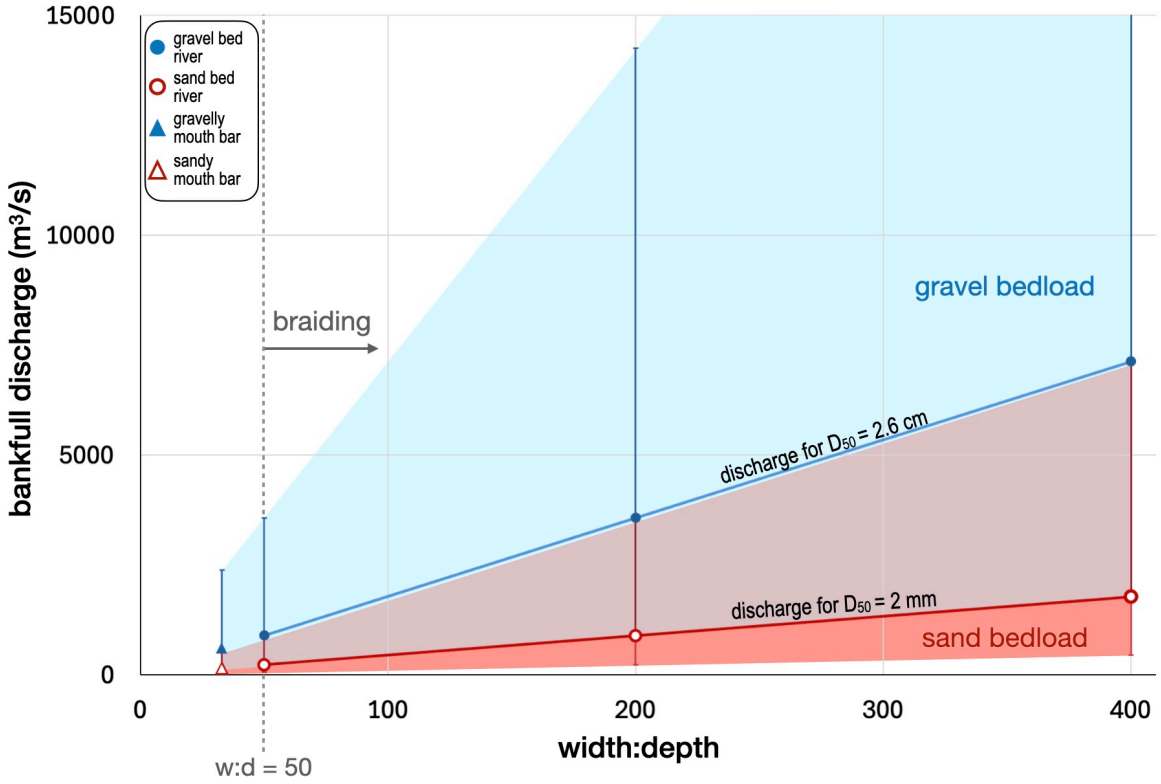

Figure S11. Discharge estimates based on Unit 3 strata height measurements yielding estimated bankfull flow depth of 4.2 m. Blue shaded region uses calculated D_{50} of 2.6 cm, slope = 0.00036, and u = 1.01 m/s. Red shaded region uses D_{50} = 2 mm, slope = 9.5 x 10^{-6}, and u = 0.25 m/s. Purple shaded region shows discharges plausible for either a gravel bed or sand bed of a given width:depth. Circles represent estimates for braided rivers at w:d = 50, 200, and 400; triangles are estimates for mouth bars, using the width of the Unit 3 form as an upper bound for channel width and yielding w:d = 33. Error bars show a factor of 6 error, as both the bankfull flow depth and the flow velocity carry an error of ~ a factor of 2 (Hayden and Lamb, 2020; Mohrig et al., 2000; Ferguson et al., 2007) and depth was used with an assumed w:d to find width.

Environment	Width-to-depth	Discharge [m^3/s]
Gravel-bed braided river	50	890
	200	3,600
	400	7,100
Sand-bed braided river	50	220
	200	880
	400	1800
Gravelly mouth bar	33	590
Sandy mouth bar	33	150

Table S5. Estimated bankfull discharge rates for range of channel geometries and bed types for mouth bars and braided rivers.

Literature examples of terrestrial steep river bar strata	
Source	*Description*
Figures 4 and 6 in Almeida et al., 2016 https://doi.org/10.1111/sed.12230	Unit bar fronts with multiple meters of relief in the Hawkesbury Sandstone in southeast Australia and the Marizal Formation in northeastern Brazil.
Figures 9 and 10 in Steel and Thompson, 1983 https://doi.org/10.1111/j.1365-3091.1983.tb00677.x	Conglomeratic braid bar fronts several meters in height in the Bunter Pebble Beds, England.
Figure 4 in Carling et al., 2013 http://dx.doi.org/10.1016/j.earscirev.2013.06.002	Pebbly sandstone and boulder conglomerate bar front beds with several meters relief deposited via megafloods in the Altai Mountains.
Figures 11 and 14 in Cowan, 1991 https://doi.org/10.2110/csp.91.03.0080	Fill of multi-meter deep scour hole or "hollow" by sandstone avalanche faces at braid channel confluences or upstream of a large bar. Morrison Formation, New Mexico.

Table S6. Compilation of terrestrial field examples of sandy and gravelly steeply-inclined braided river strata.

Literature examples of terrestrial mouth bars in shallow deltas	
Source	*Description*
Figure 9 in Gruszka and Zielinski, 2021 https://doi.org/10.2478/logos-2021-0004	~1 m thick gravelly mouth bar with sigmoidal beds, deposited in a shallow glacial lake, Poland.
Figure 10 in Leszczyński and Nemec, 2015 https://doi.org/10.1111/sed.12155	Gravelly mouth bar (<1 m thick) with sigmoidal beds deposited in shoal-water or mouth bar-type delta, Poland.
Figure 4a and 7d in Winsemann et al., 2021 https://doi.org/10.1016/j.sedgeo.2021.105962	Gravelly sub-meter to >2 m thick shallow-water mouth bar deposits with tangential beds in Germany and Spain.
Figure 6d in Schomacker et al., 2010 https://doi.org/10.1111/j.1365-3091.2009.01136.x	Sandy mouth bar ~5 m thick deposited in shallow lake. Green River Formation, Utah.

Table S7. Compilation of terrestrial field examples of sandy and gravelly shallow-water mouth bars with inclined beds.

Literature examples of terrestrial Gilbert deltas	
Source	*Description*
Figures 2 and 19 in Bell, 2009 http://dx.doi.org/10.5027/andgeoV36n1-a04	Gilbert delta deposits in Lake General Carrera, Chile. Broad, arcuate fronts shown in planview in Figure 2, and conglomeratic delta foresets shown in cross-section in Figure 19.
Figure 1 in Lai et al., 2019 https://doi.org/10.1029/2018WR023824	Gilbert delta in Peyto Lake, Canada with straight shoreline and braided channels on delta top.
Figure 1 in Ke and Capart, 2015 http://dx.doi.org/10.1002/2015GL066455	Gilbert delta with straight shoreline in Wushe reservoir, Taiwan.

Table S8. Compilation of terrestrial field examples of gravelly, homopycnal Gilbert deltas, exhibiting typical smooth, straight-to-arcuate shorelines in planview.